Pull-out of hooked end steel fibres: Experimental and numerical study

by

Christian Mpanga-A-Kangaj

Submitted in partial fulfilment of the requirements for the degree

Masters in Applied Science

in the Faculty of

Engineering, Built Environment and Information Technology

University of Pretoria

December 2013

Pull-out of hooked end steel fibres: Experimental and numerical study

Author: Christian Mpanga-A-Kangaj

Supervisor: Ms Helen Inglis

Co-supervisor: Prof Schalk Kok

Department: Mechanical and Aeronautical Engineering

Degree: Masters of Science

Keyword: fibre pull-out, hooked end fibres, epoxy matrix, finite element analysis, numerical modelling

Abstract

The reinforcement of concrete with steel fibres changes the failure of the composite material from catastrophic brittle failure to pseudo-ductile behaviour as a result of crack-bridging by the fibres, and the additional work which is absorbed by fibre pull-out. A good understanding of the properties of the fibre-reinforced concrete depends on an understanding of the fibre pull-out process. The main aim of the current study is to investigate, both experimentally and numerically, the pull-out behaviour of a single hooked end steel fibre from epoxy matrix, where epoxy was chosen to replace concrete in order to enable visualisation of the pull-out process. The experimental and numerical results both contribute to the development of a physical understanding of the mechanism of pull-out.

Experimental studies included the evaluation of the mechanical properties of hooked end steel fibre and epoxy matrix by means of tensile tests, the manufacturing of pull-out specimens consisting of a single hooked end steel fibre embedded in epoxy matrix, and the experimental characterisation of the fibre pull-out. The significant features (peaks and minima) of the load vs. displacement graph were correlated to stills taken from a video of the pull-out process, in which the plastic deformation of the fibre is evident. Small deformations (spalling) were also observed in the matrix. A model is proposed for the mechanisms which interact during the pull-out process.

Numerical analysis has been performed using a 3D finite element analysis implemented in ANSYS, incorporating nonlinear contact between the fibre and the matrix and plastic deformation of the fibre. Sensitivity studies investigated the effects of material and interface properties on the resultant load vs. displacement curve of the pull-out. Results of these studies demonstrated the importance of accurately modelling the plastic behaviour of the steel fibre in predicting the pull-out response of the system.

The numerical and experimental pull-out behaviours capture the same fundamental behaviour. The fibre displacement at critical intervals is well-correlated, and the numerically-predicted load is within the range of the experimental results at these intervals.

The finite element analysis allows investigation of the stress and strain distributions. The plastic strain accumulated in different regions of the fibre, and the maximum stress experienced in the matrix are studied, and correlated with the global response, and further understanding is gained into the mechanisms of fibre pull-out.

Acknowledgements

A successful life does not depend on self-effort, but it is a result of different contributions coming from good intentioned people that surround us. I thank God that I had wonderful people, around me, and it would not have been possible to pursue the goal of this work without their help.

I would like to express my deepest gratitude to my study leaders, Ms Inglis, Prof Kok, and Mr Pietra, for your unyielding support and enthusiastic encouragement. Thank you for your valuable guidance and constructive suggestions. Your willingness to provide generously the best of your knowledge and your quality time have been much appreciated.

I would also like to express my great appreciation to Prof Kearsley, for the suggestion that she has made regarding the research topic and more importantly for the necessary financial support provided for this research. It would be ungrateful on my side if I do not mention the technical help that I have received in the Civil laboratory at the University of Pretoria, I thank all the technicians in general and particularly to Mr Mostert for his guidance.

My special thanks are also extended to the committee of the University of Pretoria, in general, and to the Department of Mechanical and Aeronautical Engineering, in particular. The laboratory, library and computer facilities have been the indispensable resources for the completion of my research work.

I would not be the man I am today without the support and encouragement of my father Kangaj Floribert-Richard, my mother Mpanga Cécile, and with the love of my entire family, brothers and sisters, nephews and nieces. I am heartily grateful for the assistance given by my brother Tshal Flavien, his advice and consideration are much appreciated.

To my fellow friends, you have helped me tremendously. I am so thankful to God for having you as companions, you are wonderful people. Thank you for all the support you have bestowed.

Table of contents

List of Figures

viii

List of Tables

List of Symbols

A_f	Cross sectional area of the fibre
a_i	empirical constants
E	Elastic modulus (Young's modulus)
E_f	Elastic modulus of the fibre
E_m	Elastic modulus of the matrix
E_T	Tangent modulus
k_c	Contact stiffness
P_{fl}	Maximum failure load
Δ	Fibre's end displacement (slippage distance) or relative displacement between the fibre and its surrounding.
μ	Static isotropic coefficient of friction
ν	Poison's ratio (in general)
ν_f	Poison's ratio of the fibre
ν_m	Poison's ratio of the matrix
Δx_p	Penetration / gap, distance separating two nodes of contacting bodies
ΔF_c	Contact force
Δ_p	Axial punch displacement
ε	Tensile strain
τ_i	Frictional bond strength
τ_s	Elastic bond strength
σ_f	Normal stress of the fibre
σ_{fl}	Normal stress at failure
σ_p	Proportional limit
σ_u	Ultimate tensile strength
σ_{YV}	Virgin yield stress
σ_{YPl}	Work-hardened yield stress (plasticised yield stress)

Abbreviations

3D	Three-Dimensional
CAD	Computer Aided Design
FEA	Finite Element Analysis
CVFE	Cohesive Volumetric Finite Element
LCD	Liquid Crystal Display
LVDT	Linear Variable Differential Transformer
MSC	MacNeal-Schwendler Corporation
NASTRAN	NASA Structural Analysis
SP(1,2)	Sample (1,2)
S1T1, S1T2, S1T3	Series 1-Test (1, 2, 3)
S2T1, S2T2, S2T3	Series 2-Test (1, 2, 3)
SEM	Scanning Electron Microscope
TRF	Test on the right flank
TLF	Test on the left flank
TFF	Test on the front flank
w/c	water-cement ratio

1. INTRODUCTION

1.1. Motivation

Concrete material is used in most civil constructions, its worldwide use justified by the fact that its production is simple and its properties can readily be altered by changing different parameters involved in its manufacturing process, such as constituents' ratio etc. It is important to understand its fundamental behaviour in relation to its nominal functionality.

It is well known that unreinforced concrete materials fail in a brittle manner when subjected to tensile loads. For example consider in the case of an unreinforced concrete beam spanning a window opening and subjected to load as seen in Figure 1-1(A). The beam starts to deflect and cracks appear and propagate at the bottom side of the beam (Figure 1-1(B)). As the cracks grow bigger, they will split and consequently the beam collapses as shown in Figure 1-1(C) (Trevorrow, 1984). From a tensile loading standpoint, unreinforced concrete materials have very bad response, but in general they have good compression response. The poor response of unreinforced concrete materials results in premature failure of the structure, without warning, and at very small deflections. In order to prevent this catastrophic behaviour, concrete is combined with other materials to form a composite that can accommodate tensile loads without damage or destruction.
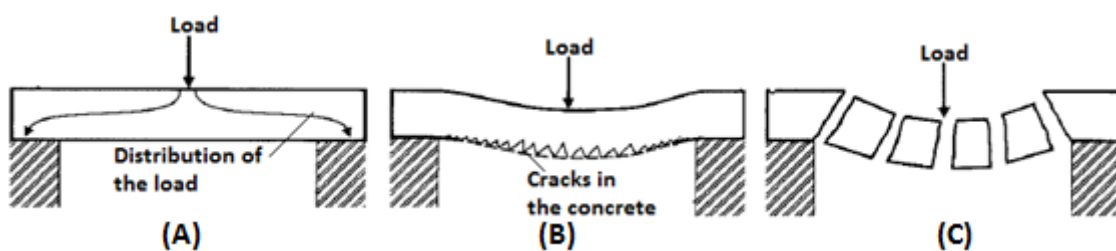
Figure 1-1. Plain concrete beam. (A)-Beam loaded. (B)-Deflection and cracking of the beam. (C)-Collapse of the beam. (Trevorrow, 1984)

1.1.1. Concrete reinforcement

Concrete reinforcement consists in inserting steel or non-ferrous metals into concrete, in the zones of the concrete experiencing tensile loads. This insertion is achieved in order to change the brittle concrete behaviour to pseudo-ductile behaviour (Grosse and Weiler, 1996). Transfer of stresses from the matrix to the reinforcement (and vice-versa) is achieved via the interface zone which is an intermediate region between the matrix and the reinforcing materials (Brandt, 1995). It should be emphasized that steel reinforcing is preferred because its coefficient of expansion is approximately the same as that of concrete at normal conditions of temperature. Additionally, amongst all materials, steel provides the best bond when combined with concrete. Steel concrete reinforcement can be classified in two different categories, firstly reinforcing bar and pre-stress reinforcement, and secondly, fibre reinforcement.

1.1.1.1. Reinforcing bar and pre-stress reinforcement

Steel bar reinforcement consists in placing the steel bar into the concrete before it hardens. The reinforcing bar, otherwise known as rebar, can be rounded or squared, and the surface can be smooth or rough. Another way of reinforcing plain concrete can be achieved by introducing internal compressive stress in the zone of the concrete subjected to tensile loads. Basic principle of concrete pre-stressing can be explained by considering a pile of books which can be lifted by squeezing their ends. An initial stress has been induced so as to compress the books together, and the stack can only be split if the tensile stress induced by the self-weight of the books is greater than the compressive pre-stress that was initially induced (Caprani, 2006). This operation is practically achieved by inducing compressive forces in the concrete by tensioning steel tendons of strands or bars placed in ducts embedded in the concrete. Internal tensile and compressive forces will then form a couple in equilibrium which will be counteracted by application of external loads. The pre-stress principle is illustrated in Figure 1-2.
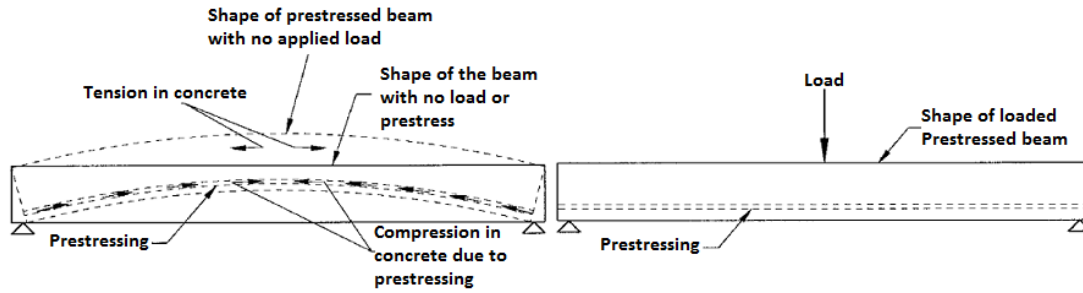
Figure 1-2. Pre-stress principle. (ACI, 2006)

1.1.1.2. Fibre reinforcement

Fibre reinforcement is the case where fibres are dispersed randomly through a concrete matrix. This mixture of fibres will then cause a high degree of random dispersion within the concrete and result in control of crack opening through fibre bridging and then will prevent the cracks from propagating within the concrete medium. Different kinds of fibre can be used for reinforcement depending on the function and importance of the structure. The following fibres can be used for reinforcement: asbestos fibres, glass fibres, steel fibres, metallic glass ribbons, polymeric fibres, natural vegetable fibres, horsehair, straw, textile reinforcement, carbon fibres (Brandt, 1995). The most commonly used in structures where safety is required, are steel fibres. For a better bond between the fibre and the concrete their geometry can be deformed (i.e., twisted, hook-ended, etc.) or their surface can be varied (i.e., smooth, indented, roughened).

1.1.2. Mode of failure observed in fibre reinforced concrete

Different studies conducted on fibre reinforced concrete have shown that concrete matrices reinforced with fibre, do not suddenly break (collapse) when the first crack is being initiated as is the case for unreinforced concrete matrix. Fibre reinforced concrete will rather sustain the loading by transferring it from the matrix to the fibre via the interface between the two thus increasing the toughness of the structure. If the load increases the failure is mainly caused by fibre debonding followed by the pull-out of the fibre from its surrounding.

1.2. Objectives of the thesis

The objective of the current research is to conduct experimental and numerical studies of the pull-out of hooked end steel fibres from a clear matrix. These studies will allow correlation between graphs of pull-out load versus fibre end displacement with images of the fibre's configuration in the matrix during the pull-out process. In particular, this will allow specific pull-out loads of interest (e.g. maximum, minimum) to be related to a physical process. Experimental studies will provide mechanical characterisations of the composite constituents (fibre and epoxy), and the pull-out of fibre from epoxy. Note that during experimental pull-out, plastic deformation of the hook of the fibre is going to be directly visualised through a transparent matrix (epoxy) and will be correlated with the pull-out response presented in the form of a graph (load versus displacement); numerical studies will also provide the pull-out graph. Additional information such as the state of stress / strain distribution for both components, the fibre and the matrix, will also be computed using numerical approaches.

1.3. Outline of the thesis

In order to achieve the main aim of the present research, different studies have been conducted; and thus rearranged into different chapters. In Chapter 2, a summary and results of some previous studies, related to the fibre pull-out, are presented. Chapter 3 provides the experimental characterisation of steel fibre and epoxy matrix; this includes the tensile test experiment setup and results. Mechanical properties of the fibre (Young's modulus, tensile strength and yield point) are determined herein. The same kinds of studies have been conducted in order to characterise the epoxy matrix. Prior to determining mechanical properties of epoxy matrix, selection of raw materials which should be involved in the fabrication of epoxy matrix is being established and the manufacturing techniques with all the processes involved are exposed. Chapter 4 illustrates the manufacturing processes of the composite which is a dog-bone shaped epoxy matrix embedding a single hooked end steel fibre. Based on the theory of Boolean operation, different techniques involved in the embedment of a hooked end steel fibre in the matrix of epoxy are explained. Thereafter, an

experimental setup of the pull-out and the pull-out results are presented and discussed. Chapter 5 illustrates different schemes used to model the pull-out response. The model is based on a 3D finite element model implemented in ANSYS. Numerical results presented in form of graphs, pull-out load versus fibre end displacement and the state of stress/strain of the composite, are provided. Comparison between the numerical pull-out curve (pull-out load versus fibre end displacement) and experiment pull-out curves is presented in Chapter 6. In closing, a summary giving an overview of the study is provided in Chapter 7.

2. REVIEW OF LITERATURE

Concrete is widely used in civil engineering structures, and much research has been focused on methods to improve its long-term serviceability and mitigate its lack of ductility. Being a brittle material, when subjected to tensile loads concrete fails suddenly without early warning of failure. When subjected to tensile loads the unreinforced matrix deforms elastically followed by micro-cracking, localized cracking and then finally fracture of the matrix (ACI, 1996). Thus reinforcement of concrete materials is of paramount importance in order to improve their effectiveness and longevity.

Historically speaking reinforcement of concrete materials is not a new subject, it has been used since ancient times. For example, in the early age, horse hair was used in mortar and straw in mud bricks as reinforcement to strengthen structures (Rajeshkumar *et al.*, 2010).

Using an energetic framework, Alwan *et al.* (1991) have defined brittle materials such as cementitious and ceramic matrices as being low energy absorbers, as a result of their small sustainable amount of deformation and their poor resistance to cracking. In order to increase total energy absorption capability, it has been suggested that either the path of cracks during separation can be increased or the material capability to deform be increased (Alwan *et al.*, 1991). Fibres inserted in a cementitious matrix can bridge cracks and then absorb energy by means of deformation or pulling out depending on their bond characteristics and the fibre's mechanical properties. In the case where the behaviour of the fibre is fairly ductile, the energy absorption mechanism involves the debonding of the fibre from its surrounding followed by sliding, deformation and possibly failure of the fibre (Cook *et al.*, 1989). Studies on engineered steel fibres with optimal properties for reinforcement of cement composite (Naaman, 2003) have revealed the importance of the fibre's surface and geometry for improving the bond between the fibre and the concrete matrix. Thus the fibre's surface can be roughed or mechanical deformation can be induced in its geometry. Fibres can be indented, deformed, crimped, coiled or twisted, with hooked ends, paddles or buttons (see Figure 2-1).
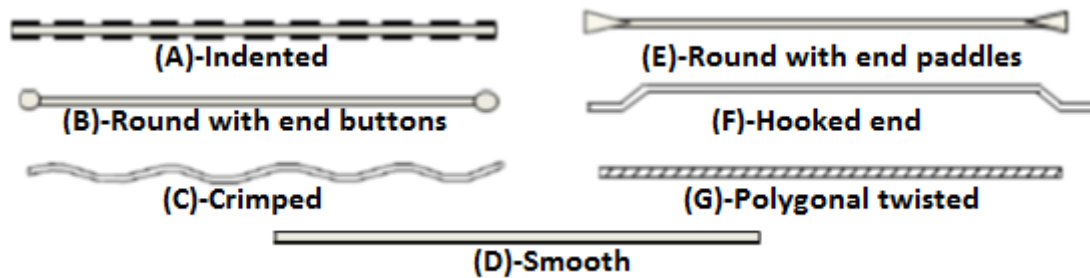
Figure 2-1. Typical profile of steel fibres commonly used in concrete. (Naaman, 2003)

These studies, conducted by Naaman (2003), have illustrated the ingenuity of adding short needle-like fibres to concrete and have proved its effect on mechanical properties improvement of the matrix, more precisely the toughness, ductility and energy absorption capability under impact.

After examination, it has been observed that addition of fibres in concrete does not improve mechanical properties before failure but only governs the post failure behaviour, and this is true for low content fibre reinforced composites (FRC). That is, the enhancement of mechanical properties of the composite is only active after the appearance of micro-cracks, when the behaviour of the composite changes from brittle (plain concrete) to pseudo-ductile (once fibres have been added) (Grosse and Weiler, 1996).

2.1. Investigation of the pull-out mechanism

Markovich *et al.* (2001) conducted studies on the tensile strength improvement of concrete materials with embedded hybrid steel fibres (fibres of different geometries: long and short). Attention was focused on the bridging mechanism of straight short and long hooked end steel fibres in concrete. It was demonstrated that each type of fibre is active in bridging cracks of their appropriate size. Therefore short straight steel fibres are active in bridging micro-cracks in the first stages of the tensile loading whereas long hooked end steel fibres will be active when micro-cracks have propagated and have grown bigger. It was found that the bridging mechanism is utterly dependent on the interface properties which in turn depend on the concrete mixture. The design of such mixtures requires a balance between

good workability and placing properties, and an optimum response under the action of tensile stresses in the hardened state (Markovich *et al.*, 2001).

As seen in Figure 2-2 the pull-out test, conducted by Markovich *et al.* (2001), simulated a hooked end steel fibre bridging an opening crack. The experimental setup of the pull-out test involved a concrete matrix with one hooked end steel fibre embedded, the free end of the fibre was clamped in a grip of a tensile testing machine and the concrete matrix was firmly fixed at the bottom plate of the machine. The slip of the fibre was measured by a displacement transducer LVDT (Linear Variable Differential Transformer).
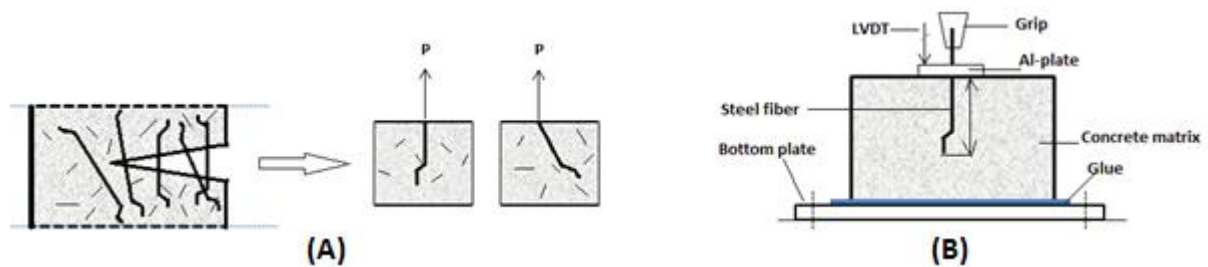
Figure 2-2. (A)-Pull-out test as simulation of the crack bridging by fibres. (B)-Scheme of the applied test setup. (Markovich *et al.*, 2001)

Results of a typical experimental pull-out test are shown in Figure 2-3, with different stages of the pull-out being correlated with the pull-out curve. All the pull-out tests conducted presented the same pattern.
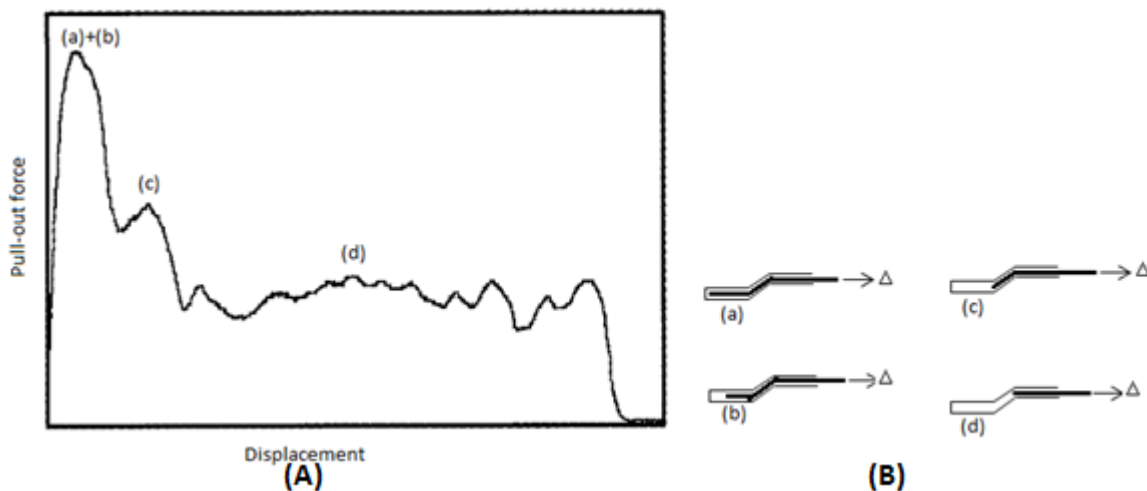
Figure 2-3. (A)-Typical fibre pull-out curve. (B)-Stages in the plastic deformation of hooked end fibre. (Markovich *et al.*, 2001)

The work of Alwan *et al.* (1999) has illustrated the pull-out mechanism of hooked end steel fibres in cementitious matrices. This mechanism consists of five different stages illustrated

in Figure 2-4: fully bonded; onset of complete debonding of straight portion or gradual debonding; bends straighten; frictional slippage; and pull-out failure.
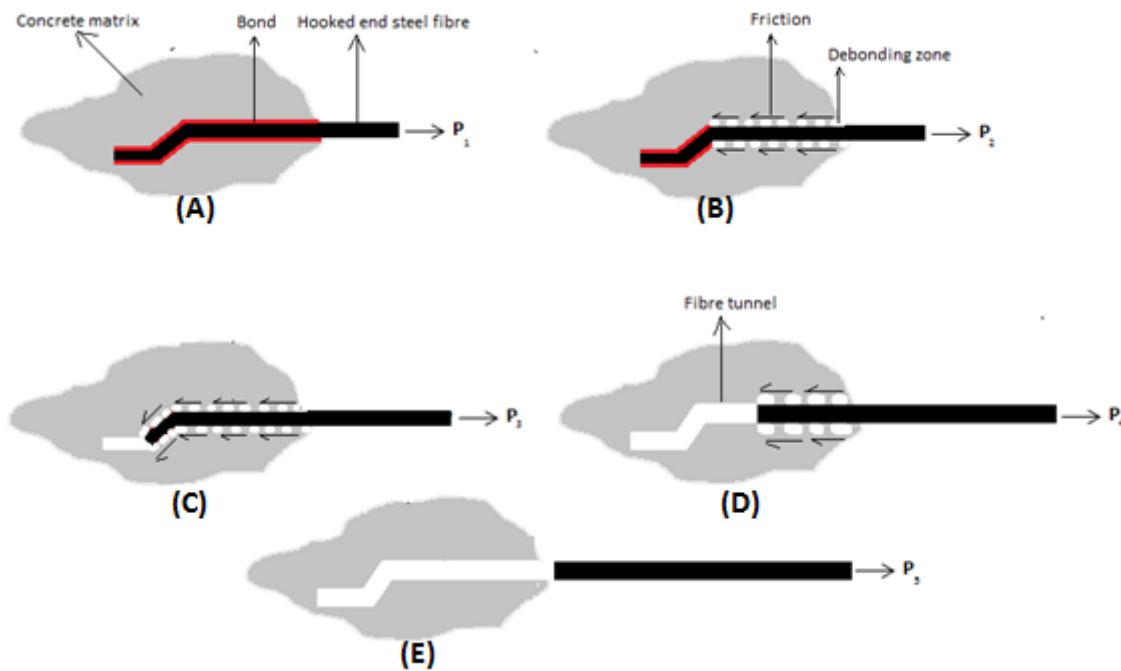
Figure 2-4. Pull-out stages for a hooked-ended steel fibre. (A)-Fully bonded. (B)-Onset of complete debonding of straight portion. (C)-Bends (Straighten). (D)-Frictional slippage. (E)-Pull-out failure.(Alwan et al., 1999).

During loading the fibre is in tensile mode and as the applied load increases the fibre elongates. Subsequently microcracks appear on the interfacial bond between the fibre and the matrix from the top surface to the bottom end. This phase is characterized by transfer of load (stress) from the fibre to the matrix and as the load still increases, the interfacial bond continues to break with a slight contraction of the fibre and slight increase in diameter of the duct (tunnel) of the matrix where the fibre was sticking (Andersen *et al.*, 2011). As this cylindrical delamination crack grows progressively from the interfacial surface of the matrix and the fibre, the maximum axial stress appears to be in the near vicinity of the top surface where the fibre comes forth from the matrix (Krasnikovs *et al.*, 2010).

Experimental results of the pull-out process for three different mixtures can be seen in Figure 2-5. The discrepancies between the different pull-out curves is a characteristic of such failure process, which are dependent on the properties of the mixture (Markovich *et al.*, 2001) as well as the heterogeneities of the concrete.
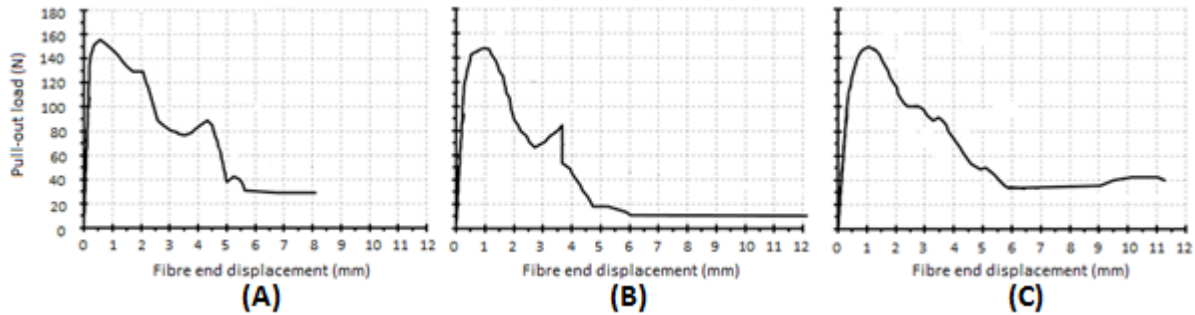
Figure 2-5. Experimental results for different pull-out of hooked end steel fibres 30mm long embedded (12.5mm) in concrete matrix. (A)-Mix 1. (B)- Mix 2. (C)-Mix 3.(Alwan et al., 1999).

Throughout these studies, the importance of ensuring the effectiveness of the fibre-matrix reinforcement has been pointed out. Based on different analyses of experimental tests, it has been shown that the effectiveness in concrete matrices could be guaranteed if the following criteria were met (Naaman, 2003):

- The tensile strength of the fibre should be significantly higher than the tensile strength of the concrete, in the range of 2 to 3 orders of magnitude;

- The bond strength of the fibre should be of the same order or higher than the tensile strength of the matrix;

- The elastic modulus of the fibre, in tension, should be significantly higher than that of the concrete;

- The Poisson's ratio and the coefficient of thermal expansion should be of the same order for both the matrix and the fibre. It has been also noted that if the Poisson's ratio of the fibre is significantly higher than that of the matrix, detrimental debonding will occur under tensile load.

2.2. Factors which affect pull-out

According to investigations of Laranjeira *et al.* (2010) the contribution of the mechanical anchorage of hooked end steel fibres to the peak pull-out load is tremendously dependent on several material properties such as the fibre's geometry and matrix properties. It has been shown that more the larger the fibre diameter, the more energy is required to deform the fibre due to the increase of its bending stiffness (Laranjeira *et al.*, 2010). Moreover if the matrix where the fibre is embedded is stiffer the pull-out response becomes better. Other

interesting effects such as embedment length of hooked end and smooth (straight) steel fibres on the peak pull-out load and total work of pull-out have been examined and results (Hamoush *et al.*, 2010) have shown that increase in embedment length increases also both peak load and total pull-out work, but further it was noticed that smooth and undeformed fibres were the most influenced.

As the pull-out work is a function of the end slip of the fibre, it is of paramount importance to maintain the work at an optimum level. A very stiff matrix can result in insignificant or small pull-out work due to the fact that the fibre will break instead of slipping prior to debonding. A very soft matrix will result in poor bonding and mechanical anchorage mobilization. Therefore precautions should be taken in the concrete mixture design.

The dependence of the pull-out behaviour on specimen geometry has been examined during an experimental studies (Tsai and Kim, 1996) involving two glass fibres, coated with acrylate or gold, embedded in two epoxy matrices of different geometry (Figure 2-6). The experiment test was schematically represented by a system of mass-spring system (Figure 2-7) where the attached spring represents the compliance of the epoxy matrix and the testing machine.
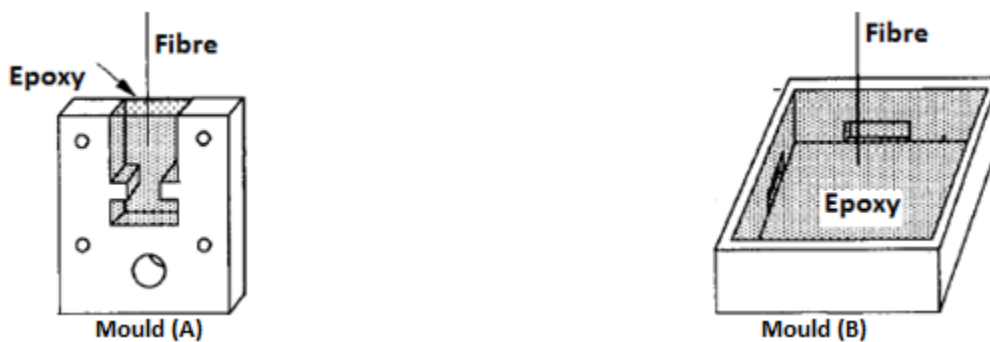
Figure 2-6. Two different moulds resulting in two geometries of epoxy matrices embedding a single fibre for pull-out experiment. (Tsai and Kim, 1996).

Test results revealed the same behaviour for both geometries (epoxy cast in mould (A) and (B), see Figure 2-6); that is, it was concluded that the global geometry of the matrix does not influence the pull-out response. Only the nature of the local deformation near the edge of the interface and the active sliding zone propagation condition account for the pull-out response.
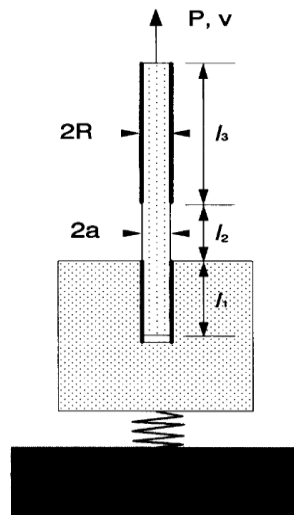
Figure 2-7. Schematic representation of the fibre pull-out test. (Tsai and Kim, 1996).

2.3. Analytical models of pull-out

From a prediction standpoint, many studies have been conducted in order to determine, analytically or numerically the pull-out response of fibres. Most of the analytical studies aimed to determine the pull-out behaviour in form of graphs, pull-out load versus displacement or bond stress versus fibre's slip. Two different analytical approaches based on force equilibrium equations and related to an axisymmetric model are considered: the perfect interface and the cohesive interface models. The former, also known as shear-lag model, is usually utilised for analyses of stress transfer problems dealing with resin matrix composite, whereas the latter is used to analyse cement based composites (Banholzer *et al.*, 2005).

Theoretical analyses and modelling of fibre pull-out from brittle materials has been conducted (Wang *et al.*, 1988). In this approach steel fibre's behaviour was predicted after experimental studies on synthetic fibres such as nylon and polypropylene. The aim was to predict the pull-out force versus the displacement relationship by simply observing the fibre's surfaces abrasion based on the theoretical model. The definitive model which is that of the steel fibre was an adjustment of the theoretical model (the predicted pull-out behaviour) and experimental curves plotted during pull-out of nylon and propylene fibres. In the theoretical model it was assumed that the fibre is strong enough to pull-out completely without being ruptured, linear behaviour of fibres during pull-out was considered and the

matrix deformation was neglected. These assumptions result in the effect of Poisson's ratio and the elastic bond strength (τ_s) being neglected. During debonding the shear stress intensity in the elastically bonded zone decays approximately exponentially with the distance from the debonding point. Only the frictional bond strength (τ_i) was simulated and it was found that it varies with the slippage distance between the fibre and the matrix. It follows that the frictional bond strength in pull-out of steel fibres decreases as the slippage distance increases. This is related to the breakdown of the cement at the fibre-matrix interface due to the stiffness and hardness of the steel fibre. On the other hand in case of pull-out of nylon and propylene fibres, the frictional bond strength was found to increase due to the fibre's surface abrasion and accumulation of wear debris.

Two different configurations have been considered: direct pull-out problem (one sided pull-out problem) whereby the force is directly applied to the free end of the fibre and the two-sided pull-out problem case where a fibre is embedded in a matrix across a crack plane (see Figure 2-8).
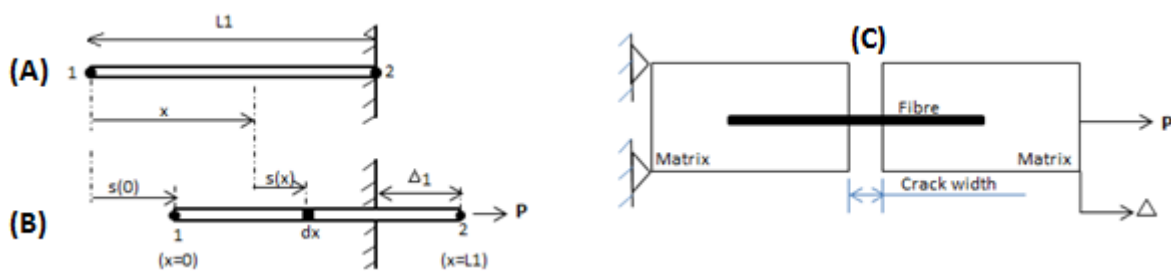
Figure 2-8. Illustration of fibre pull-out problem. (A)- Direct pull-out before loading. (B)- Direct pull-out during pull-out. (C)-Two-sided pull-out. (Wang *et al.*, 1988)

The pull-out load, in case of direct pull-out problem, was modelled by considering two different configurations: before and during pull-out. The x-coordinate system is with respect to the fibre's geometry before loading (undeformed) and is associated with the material particles. The slippage distance, $s(x)$, taken to an infinitesimal segment of the fibre Δx was found to be the sum of the slippage of the fibre's embedded end plus the elastic elongation of the fibre between 0 and Δx.

Furthermore the theoretical prediction representing the load versus slippage distance was achieved based on a quadratic formulation of frictional bond strength (τ_i) as function of the slippage distance $s(x)$:

$$\tau_{(s)} = \sum_{i=0}^{n} a_i s^i \qquad \text{(2-1)}$$

where a_i are empirical constants determined in such a way that theoretical curves are reasonably correlated to experimental results. The predicted pull-out model, presented in form of curve (load versus displacement) is shown in Figure 2-9.
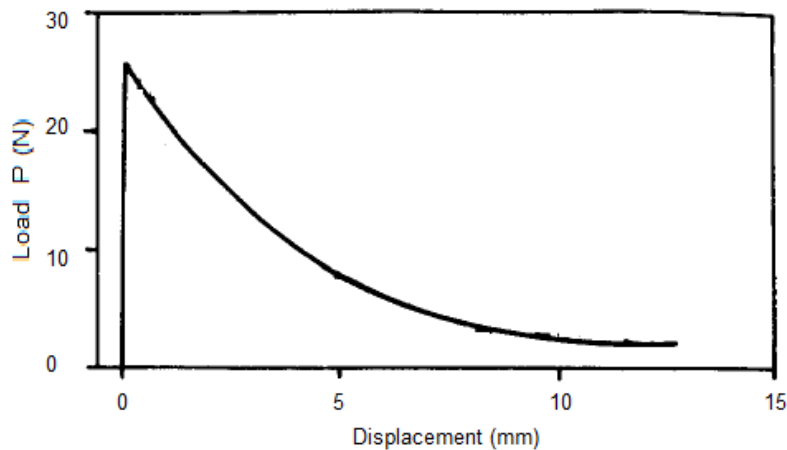
Figure 2-9. Pull-out model prediction. (Wang *et al.*, 1988).

The bond stress versus the fibre displacement can also be calculated analytically from the load displacement distribution obtained from a pull-out test. To derive the bond law from experiment data (pull-out load versus displacement) bond parameters have to be estimated a priori; and then the resulting curve should be compared to the experimental one after which an optimisation process will be conducted in order to determine the best approximation of the bond law. Based on the fact that the interfacial material properties (bond stress versus slip) are directly derived from the experimental pull-out curve, this method is termed to be the direct boundary value problem (Banholzer *et al.*, 2005). The contrary is also feasible; the bond law can be used to simulate the load displacement distribution. In this case the problem is termed to be the inverse boundary value problem (Banholzer *et al.*, 2006).

Models for debonding process of ceramic fibres embedded in ceramic matrix have been analysed (Hutchinson and Jensen, 1990). The fibre-matrix interface debonding was modelled by a cylindrical cell with two sets of boundary conditions representing the model of an isolated fibre-matrix unit and the matrix containing an array of unidirectional fibres. Emphasis was laid on systems with residual compressive stress acting across the fibre-matrix

interface. It turned out that in such conditions friction effects are very important and it was concluded that large amount of friction implies small debonding when the fibre breaks whereas for no consistent friction, large debonding is observed. The model was used under assumptions of transverse elastic isotropy about the fibre's axis, elastic and isotropic material for the matrix. The debonding was treated by fracture mechanic approaches. This model was restricted only to composite materials for which the fibre and the matrix have the same Young's modulus (E) and Poisson's ratio (ν). According to their investigations there is no difference in the model for the two types of boundary conditions when the fibre and the matrix have the same elastic properties. But in contrast important discrepancies appear when there is significant mismatch in elastic properties. Steady crack propagation has been observed in the case of identical fibre and matrix properties with constant friction model. This steady behaviour is reached when the debonding length (l) is equal to the fibre's radius.

Another analytical model for obtaining the local bond stress-slip relationship of hooked end steel fibres embedded in concrete matrix was examined. The pull-out problem was mathematically formulated and all the numerical algorithm of the model was presented as well (Cunha et al., 2008). In the end the analytical model was validated using experimental pull-out results. A cohesive interface model was used to obtain the bond stress-slip relationship. A nonlinear bond stress-slip law was introduced into the model in order to account for the interfacial bond, and a nonlinear spring component was also introduced to account for the reinforcement mechanism resulting from the fibre's mechanical anchorage. Two different approaches were used to formulate the debonding criteria. The first is a stress-based (strength-based) criterion, in which it is assumed that debonding starts when the interfacial shear stress exceeds the shear strength. The second criterion is a fracture-based criterion in which the debonding zone is considered as an interfacial crack. The pull-out behaviour was simulated by means of second order differential equations in terms of slip, with adhesion and friction simulated by a local bond-slip relationship and mechanical anchorage simulated by a spring component. The pull-out of hooked end steel fibre from concrete is being modelled by a matrix embedding a straight fibre; hook of the fibre is replaced by a spring as can be seen in Figure 2-10.
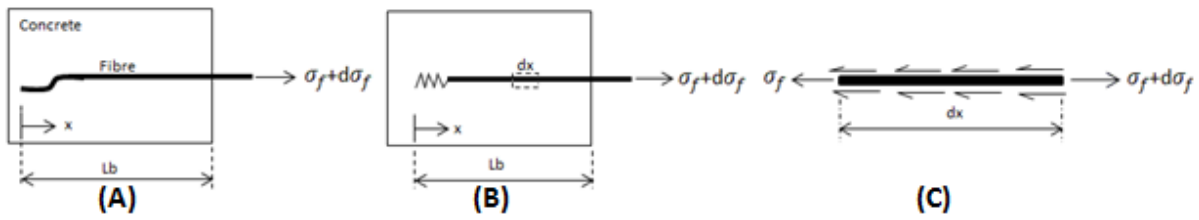
Figure 2-10. Axisymetric pull-out model. (A)-General problem. (B)-Simplified model. (C)-Equilibrium of an infinitesimal fibre free-body.(Cunha et al., 2008).

2.4. Numerical models of pull-out

Studies on interfacial failure in quasi static push-out on a composite material (Lin *et al.*, 2001) have reported four types of failure in the case of crack propagation perpendicular to the reinforced bar. The schematic of the push-out test is shown in Figure 2-11. A finite element scheme with embedded cohesive elements was used to model the physics of the push-out under axisymmetric conditions, where the bilinear rate-independent intrinsic cohesive model was coupled with a frictional contact element. Lin *et al.* (2001) have noticed in their studies that the matrix cracking, fibre-matrix debonding, fibre pull-out and fibre breakage, are the inevitable source of energy dissipation in a push-out mechanism.
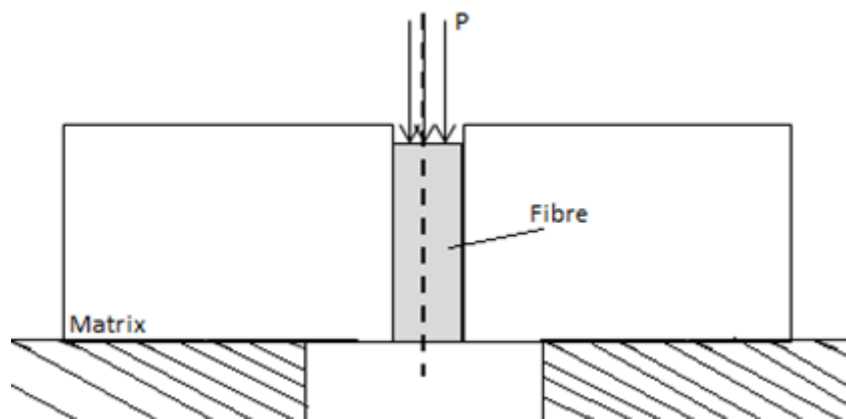
Figure 2-11. Schematic of a push-out test of a model composite system. (Lin *et al.*, 2001).

Different phases of the push-out phenomenon have been identified from a typical load versus displacement curve obtained during experimental testing. As seen in Figure 2-12, Zone I corresponds to a perfectly bonded stage of the composite and the response to the applied load is linear. As the load increases a crack initiates from the top of the specimen and start to propagate along the interface thus leading to a nonlinear force-displacement relation (Zone II). There is a point where the crack reaches critical length leading to an

unstable process which is characterized by the complete debonding of the fibre from the matrix. The instability within the system is accompanied by frictional sliding of the fibre out of the matrix (Zone III). It has been noted that the sliding process (Zone III) could be either continuous or involving a stick-slip process depending on the roughness of fibre's surfaces and the magnitude of the compressive residual stresses acting along the interface.

Experimental results were interpreted based on various analytical investigations including the shear-lag theory which has been approached under the assumption of a uniformly distributed compressive (residual) radial stress (Lin *et al.*, 2001).
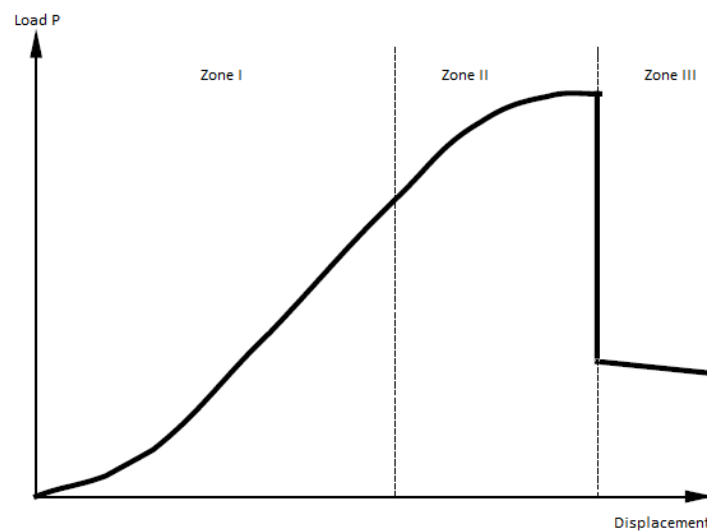
Figure 2-12. Schematic of a push-out test of a model composite system. (Lin *et al.*, 2001)

The axial load acting on the fibre was assumed to be solely transmitted to the matrix through shear stresses acting on the interface. The fibre's end and surface effects were neglected as well. The simulation was conducted in two steps: first residual stresses associated with the chemical shrinkage experienced by the matrix were induced, and second, the axial punch displacement (Δ_p) was applied to the top of the fibre. The contact between the punch and the fibre, the bottom side of the matrix and the support, were assumed to be frictionless at the beginning of the simulation. The corresponding punch force (P) was determined by summation of reaction forces on punch nodes.

In order to account for nonlinearities encountered in the physical model, Georgiadi-Stefanidi *et al.* (2010) have analysed the pull-out of hooked end steel fibres from high strength cementitious matrix by means of three dimensional finite element modelling. The aim was to experimentally characterize the bond strength between the fibre and the matrix

so that the result could be implemented in the numerical model. Thus, a straight steel fibre was pulled-out from the matrix in order to obtain the frictional behaviour of the pull-out.

The physical problem was simulated by two deformable bodies representing the cementitious matrix and the steel fibre. Due to the fact that during the pull-out process the load is firstly transferred by bond shear stresses and secondly by frictional stresses the debonding criterion in the simulation was based on a yield surface defined by the normal and shear strength of the interphase. The bonding mechanism was taken into account by introducing an interfacial zone between the fibre and the matrix as a third phase with lower stiffness and strength than the matrix or fibre. This interfacial zone was modelled as nonlinear springs acting tangentially to the interface (Figure 2-13.). The pull-out response obtained from experimental results was used to determine the stiffness of the spring element. The contact and friction forces were accounted for by introducing unilateral contact and friction conditions between the fibre and the matrix.
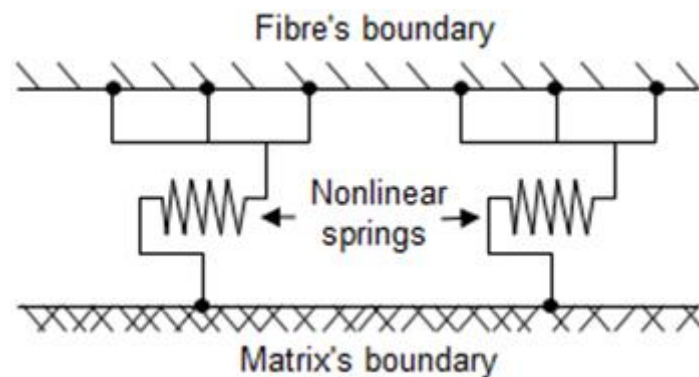
Figure 2-13. Schematical representation of the function of the interfacial elements between the steel fibre and the cementitious matrix. (Georgiadi-Stefanidi *et al.*, 2010).

The numerical model was implemented by using MSC-MARC software. The solution was conducted using Von Mises plasticity criterion with an isotropic hardening rule for the expansion of the yield surface. Investigations on different coefficients of friction as well as the geometry of the hooked end of the fibre were performed. It has been pointed out that the peak pull-out load is noted to be utterly dependent on the friction and mechanical anchorage. Five solutions were conducted with coefficients of friction ranging from 0 to 0.2, and the highest peak pull-out load was correlated with the highest coefficient of friction (0.2) as seen in Figure 2-14.
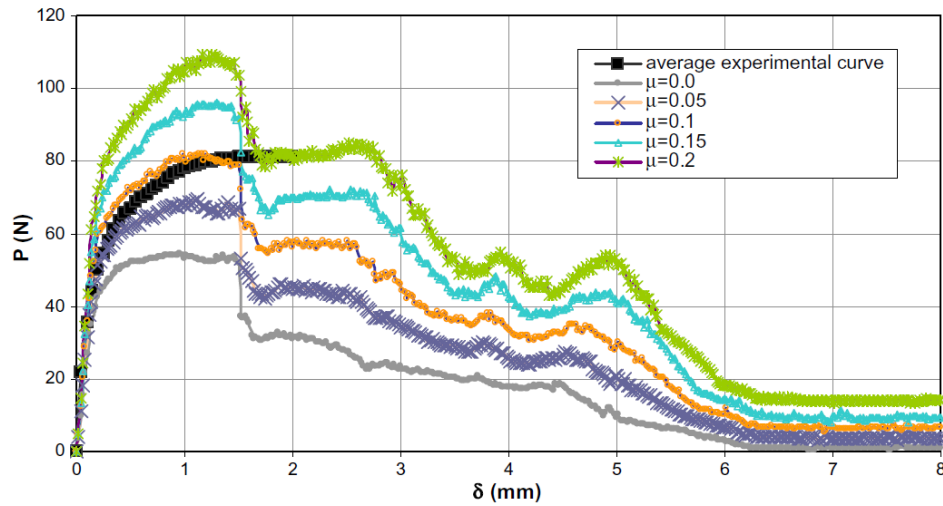
Figure 2-14. Comparison of the load-displacement diagrams obtained by the three-dimensional model for various values of the friction coefficient, with the average experimental curve. (Georgiadi-Stefanidi *et al.*, 2010).

Mobasher and Li (1998) simulated the pull-out of a straight fibre from cylindrical cement based composite by means of two-dimensional finite element analysis using axisymetric formulations. The model used is presented in Figure 2-15. In this model both the fibre and the cement matrix was considered to have linear behavior, the interfacial zone was characterized as a linear elastic third phase which has a thickness of $50\mu m$ and the ratio of Young's modulus of the interface layer to the matrix phase was 0.1. The effect of residual compressive stresses due to matrix shrinkage was simulated by a clamping pressure applied at the outer surface of the matrix.
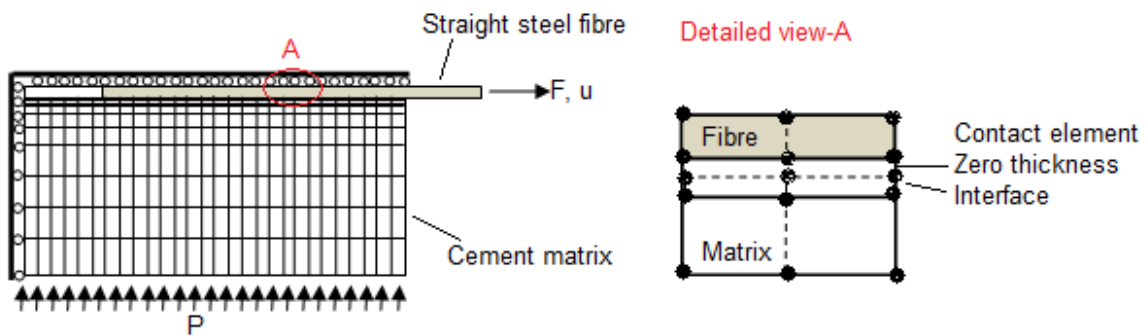
Figure 2-15. 2D axisymetric finite element model of straight fibre pull-out from cement matrix. (Mobasher and Li, 1998).

The pull-out response, see Figure 2-16., was obtained after implementation using the nonlinear finite element code ABAQUS. The debonding was initiated by means of yielding at the interface and progress gradually from the free end of the fibre, where the load is applied, to the embedded end. It has been observed that the maximum load occurs under

partial debonding conditions, thereafter the process is governed by frictional pull-out of fibre with a constant shear distribution at the highest slip level.
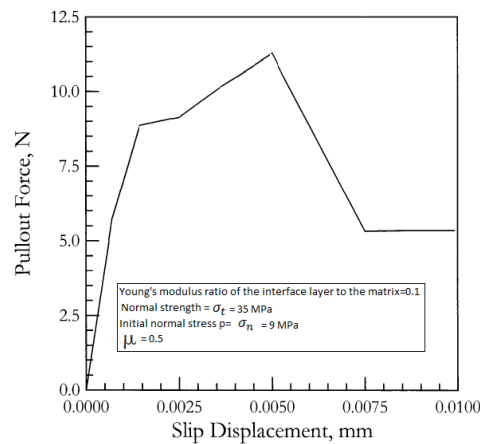
Figure 2-16. Pull-out response of a 2D axisymetric finite element model of straight fibre pull-out from cement matrix-(Mobasher and Li, 1998).

2.5. Proposed study

As can be observed from this literature review, many studies have been carried out concerning the pull-out response of fibres from their corresponding matrix. Different approaches have been taken in pursuing the objective by conducting solely experimental studies, numerical or analytical simulations. In some cases both experimental and numerical or analytical studies have been conducted. In the current research, the pull-out of a single hooked end steel fibre from epoxy matrix will be studied both experimentally and numerically.

Based on the experimental setup presented by Markovich *et al*. (2001), current experimental studies are built under similar conditions except that an LVDT was incorporated into the tensile testing machine and a dog bone-shaped clear epoxy matrix is used. The choice of embedding the fibre in a clear matrix, as studied by Grosse and Weiler (1996), allows a direct observation of the fibre's positions during pull-out. Numerical studies are going to be conducted using a three-dimensional finite element framework implemented in ANSYS Workbench. As was the case in simulations conducted by Markovich *et al*. (2001), in the current study effects of the matrix deformation are neglected and the solution is conducted in two steps which consist of solving contact problems and then

application of a prescribed displacement to the fibre's free end. In contrast to the study of Georgiadi-Stefanidi *et al.* (2010), the current study has simulated the physical problem by a deformable body, the fibre, embedded in an elastic body, the epoxy matrix. Previous finite element studies have provided pull-out curves, but have not given information on the state of stress or strain during deformation. The present research studies the pull-out behaviour of a hooked end steel fibre from epoxy matrix, both through the macroscopic pull-out and an examination of the fibre configuration and matrix tunnel deformation at different stages of loading.

3. EXPERIMENTAL CHARACTERISATION OF STEEL FIBRES AND EPOXY

As per the earlier introduction, the present research aims to determine experimentally and numerically the pull-out response of a single hooked end steel fibre from epoxy matrix. Prior to determining the pull-out behaviour it is of paramount importance to characterise individually each component of the composite, since it is required as input in the numerical model.

3.1. Tensile testing machine

Mechanical properties of steel fibres and epoxy matrix were achieved by performing tensile tests with different setup depending on specimens at which the test is performed. That is, the experimental setup of the fibre differs to the experimental setup of epoxy.

The tensile testing machine that was utilised is a universal material testing machine (Figure 3.1.) of type EZ50 (standard) which can apply loads up to $50\ kN$. This machine comprises a twin column designed with a maximum crosshead travel range of $855\ mm$. The crosshead is driven by twin lead screws actuated by a servo motor and a DC servo system in order to achieve a wide range of speed throughout the full load range. The entire process is microprocessor controlled, and uses *NEXYGENPlus*, data analysis and material testing software (AMETEK, 2009). Data inputs are manually entered by means of a keypad and the outputs and setup information are displayed on an LCD screen. It should be noted that this machine has the additional flexibility of being connected to a personal computer with *NEXYGENPlus* material test and control software incorporated. In this case data inputs can be entered manually by means of the computer's key board and the outputs are directly displayed on the screen of the computer.
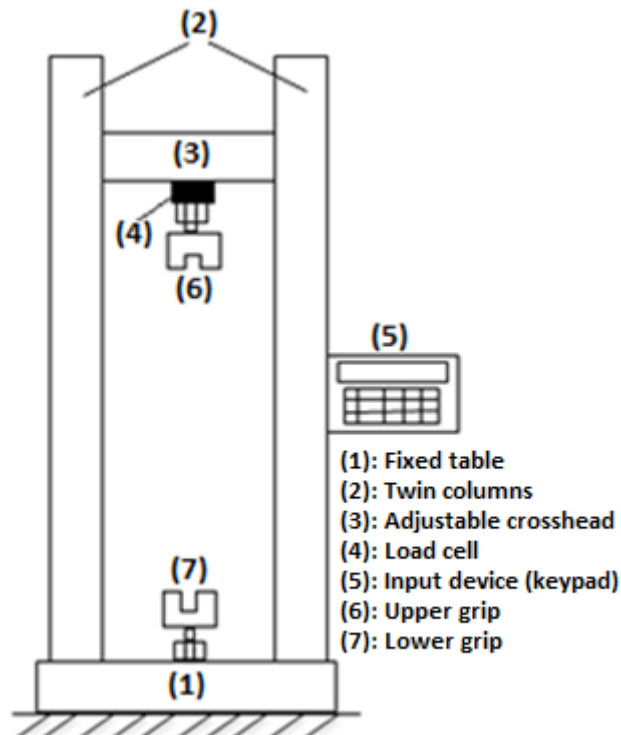
Figure 3-1. Schematic of the tensile testing machine EZ50 (Standard)

3.2. Characterisation of steel fibres

3.2.1. Material definition

The composite material used in this thesis comprises hooked end steel fibres (Figure 3-2.) embedded in an epoxy matrix (see Figure A-2, Appendix A). Steel fibres were manufactured by "Shanghai Shi Wei Ke Industrial & Trading CO. Ltd" for Insimbi Alloy Supplies (Pty) Ltd. Specifications of steel fibres, according to the supplier, are listed in Table 3-1.

Table 3-1. Specifications of the fibre according to the supplier

Length (L) [mm]	Diameter (D) [mm]	Rate of L/D	Appearance quality	Tensile strength [MPa]
60±1	~0.9-0.95	66.6	clear surface with impurities less than 0.1	> 1100
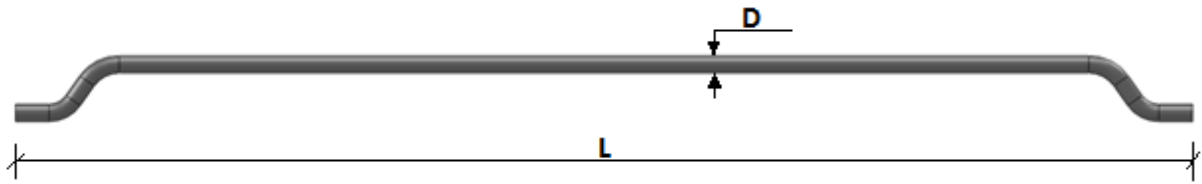
Figure 3-2. Hooked end steel fibre. L=60mm, D=～0.9-0.95 mm

Mechanical properties of steel fibres were determined by means of tensile tests. Parameters of interest in these tests are the following: tensile strength, yield stress and post-yielding behaviour. Force was measured using the built in load cell in the tensile testing machine. Displacement was measured both using the built in displacement measure of the crosshead and, where possible, by a clip gauge. A crosshead speed of 5 mm/min was used in these tests.

A subset of tests was conducted on steel wire (see Figure 3-3) prior to being cut and shaped into hooked end steel fibres. 20 cm of steel wire was used as a tensile testing sample clamped at both ends and the gauging device was installed in the middle far away from stress concentrations.

Figure 3-3. Steel wire prior to be cut and shaped into hooked end steel fibres.

3.2.2. Gripping mechanism

Tensile tests of hooked end steel fibre were achieved after many trials during which particular attention was paid to the manoeuvrability and effectiveness of the gripping system. The early tests were conducted by means of manual mechanical wedge action grips as seen in Figure 3-4. The principle of operation of these grips consists in tightening the spindle wing nut, thus moving downwards two wedges and consequently decreasing the distance between the vertical flat faces of the wedges. These grips were discarded because the tensile tests results were not satisfactory. All the fibres tested with these grips failed either in the upper or lower grips instead of failing in the middle.

(1): Spindle wing nut. (2): Wedges. (3): Load cell of the tensile testing machine. (4): Adjustable crosshead of the tensile testing machine.

Figure 3-4. Mechanical wedge action grips mounted on a tensile testing machine.

It was concluded that the fibre's failure in the grips could be a result of stress concentrations induced in the fibre due firstly to the fibre's dimension (very thin) and secondly to the difficulty in equally tightening the lower and the upper grips. Therefore these grips were

ineffective for gripping the steel fibre. Another approach was tried by gripping the fibre by the custom gripping device illustrated in Figure 3-5. These grips were locally manufactured, in the laboratory of the Civil Engineering Department of the University of Pretoria. This device comprises two hardened steel bars (1) pinned together in the middle by a screw (2). One of these bars has a pressure screw (3) which exerts a certain compressive pressure on the face of the opposite bar. These two bars are fastened together by two thin plates (4), attached on both sides of the bars, by means of bolt and nut (5).

(1): Hardened steel bars. (2): Screw. (3): Pressure screw.
(4): Thin steel plate. (5): Bolt and nut.
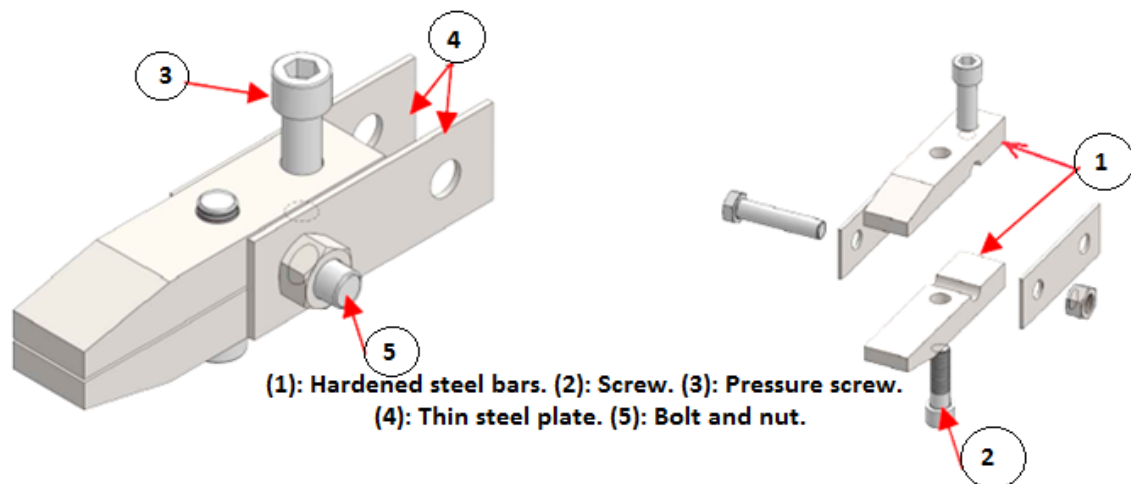
Figure 3-5. Prototype of a tensile testing grip.

As for the previous setup, fibres tested with these grips also failed in the grips as a result of stress concentrations. From the manoeuvrability point of view, both the mechanical wedge action grip and the custom grip seemed to be tedious in the way that the operator has to manually tighten the wing nut or the pressure screw while the fibre is being mounted. This operation should be undertaken with care for fear that torsional stresses could be induced in the fibre.

Hydraulic wedge action grips were found to solve both problems: stress concentration induction and tedious manoeuvrability. These grips are simple to manoeuvre. In order to clamp the fibre, it is sufficient to hold it with one hand and place it between two wedges of the grips. Next the transfer of fluid from the manometer to the wedges of the grips is simply achieved by pressing on the pedal with one foot (Figure 3-6.). Tensile tests of steel fibre conducted with the hydraulic wedge action grips resulted in failure of the fibre in the desired locations, namely between the two grips (lower and upper); and it was observed that the gripping did not alter (damage) the clamping surface of the fibre.
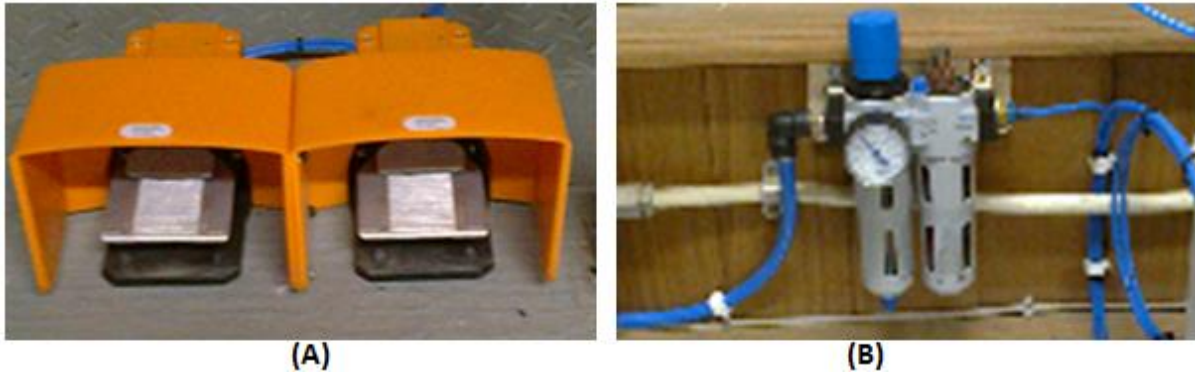
Figure 3-6. Accessories of hydraulic wedge action grips. (A) Set of foot pedals. (B) Pressure manometer with the connectors.

3.2.3. Displacement measurement

Displacement measurements are readily available from the tensile testing machine in form of crosshead displacement, however, these measurements are not an accurate reflection of the deformation in the sample as they include machine compliance. It was desired to install a gauging device (50mm in length) in the middle of the fibre for displacement measurement purposes. Based on the hooked end fibre's geometry (the length), if the gauging device had to be directly placed in the middle of the fibre, there would not be enough space to clamp both ends of the fibre. For this reason, steel wire was tested. Figure 3-7 shows the setup used for tensile test of steel wire. It comprises a steel wire of $20\,cm$ in length mounted (clamped) on a tensile testing machine of type EZ50 (standard) by means of hydraulic wedge action grips. In the middle of the fibre a gauging arrangement of type clip-on strain gauge or extensometer was installed.

The extensometer used includes different ranges of gauge length and extension; standard specifications are given below (AMETEK, 2009):

- Gauge length: $25\,mm$, $50\,mm$, and $100\,mm$
- Extension: $5\,mm$, $10\,mm$, $12.5\,mm$ and $25\,mm$
- Accuracy: $\pm 0.3\,\%$ at gauge length

In the current setup the gauge length used was that of $50\,mm$.

The mounting of the steel wire and clip-gauge was achieved in two steps. First the steel wire was placed in the machine by clamping one of its ends in the lower grip, the free end was

secondly clamped in the upper grip which is rigid with the adjustable crosshead. Once both ends were clamped, the adjustable crosshead was slowly moved up until the steel wire was extended. This could be verified by reading the output on the LCD screen of the testing machine, once it indicated zero load or any other number in this vicinity then the mobile crosshead was stopped. This configuration indicates that the steel wire is well straightened up.

Afterward the gauging device was installed with precautions to avoid slippage during the test. Two blades of the gauging device were tightly held in permanent contact on the adjacent surface of steel wire by means of two elastic bands (one at each blade). The rubber band was attached to the gauging device and criss-crossed as much as possible around the steel wire so that the blades of the gauging device could be permanently pushed against the surface of steel wire.
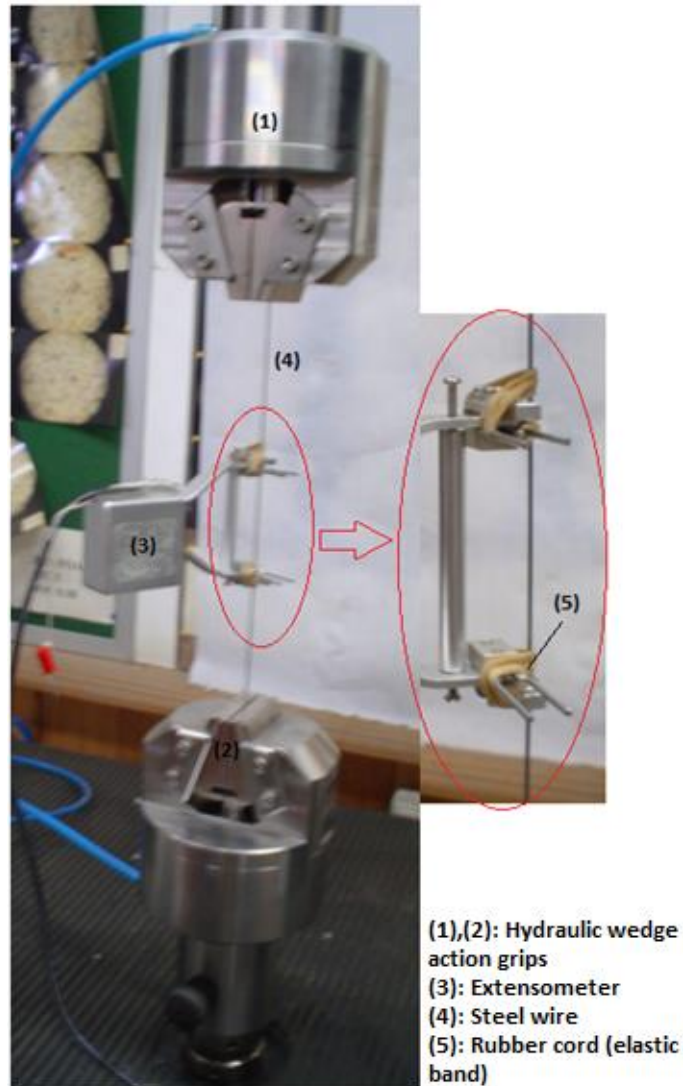
Figure 3-7. Tensile test of steel wire-Experimental setup.

3.2.4. Experimental results

The tensile test was conducted in two different manners: firstly the test was performed on the hooked end steel fibre and secondly on unshaped steel wire. The tests conducted directly on hooked end steel fibre could easily provide the tensile strength, but quantities such as the elastic modulus were difficult to obtain because of inaccuracies in measuring displacement, as discussed previously. Tests conducted on longer samples of steel wire were used to establish the elastic modulus.

Figure 3-8 illustrates the failure area of a hooked end steel fibre after completion of a test. The results of nine tensile tests conducted on hooked end steel fibres, without any gauging

device placed directly on the fibre, are given in tabular form in Table 3-2., and in graphical form in Figure 3-9. These results were obtained after data processing on original test data which presented unnecessary effects such as the machine jumps, etc.
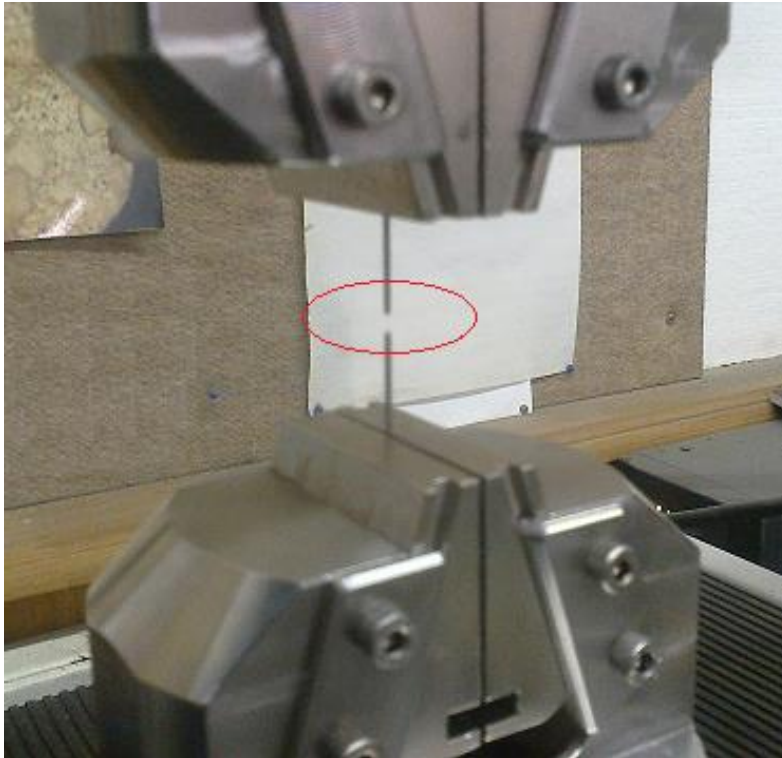
Figure 3-8. Failure of hooked end steel fibre after tensile test.

Table 3-2 presents the maximum load (peak load) and the tensile strength which is obtained by dividing the maximum load by the cross sectional area of the fibre (6.36×10^{-7} m^2). From these results it can be observed that the failure load (load at rupture of the fibre) is equal to the maximum load. Subsequently the engineering fracture strength, obtained by the ratio of failure load with the cross section of the fibre, is equal to the tensile strength.

Table 3-2. Tensile test results of hooked end steel fibres.

Test	Max Load [N] P_{max}	Tensile strength [MPa] σ_u
1	905.2	1422.9
2	925.8	1455.3
3	943.4	1482.9
4	936.4	1471.9
5	974.4	1531.7
6	947.7	1489.7
7	965.6	1517.8
8	889.7	1398.5
9	891.1	1400.7
Standard deviation	30.7	48.2
Average	931.0	1463.5

As far as the magnitudes of tensile loads and axial stresses are concerned, test results have shown small discrepancies (see Table 3-2). The data points tend to be very close to the mean value with a small standard deviations. This indicates that the tests were conducted in a standardised manner and, therefore, testify to the repeatability of the results.
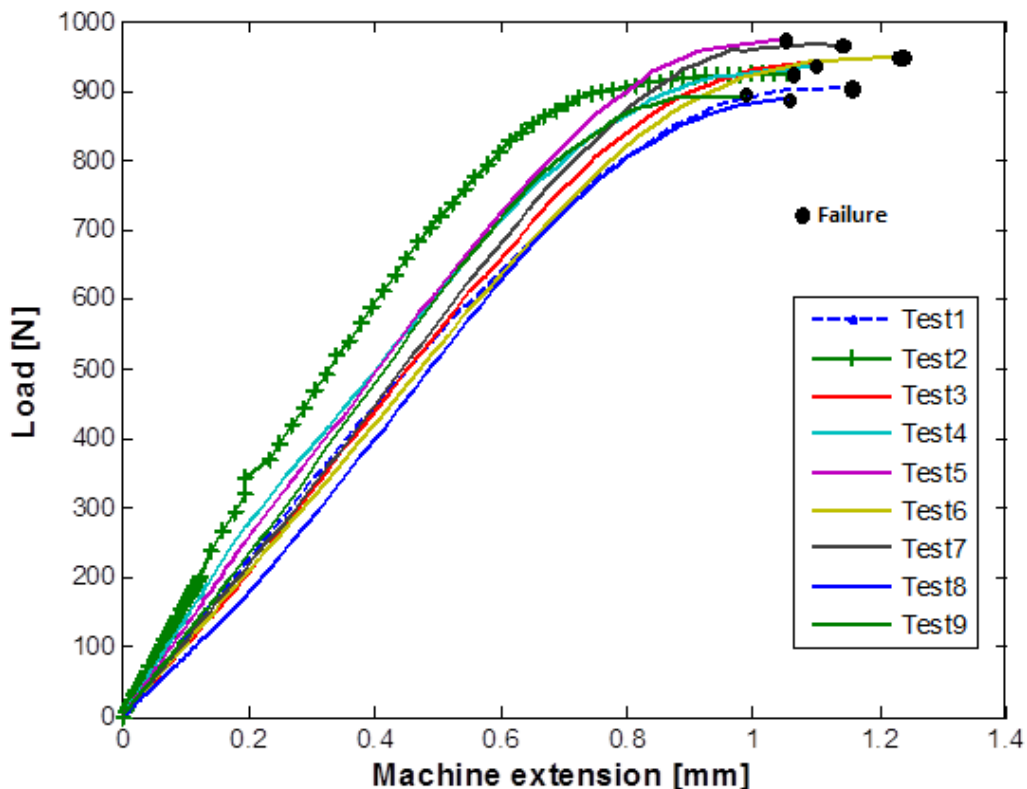
Figure 3-9. Tensile test of hooked end steel fibre.

Accordingly, four tensile tests have been conducted on steel wire with a gauging device installed on the specimen, Figure 3-10 shows the results recorded in form of a graph load

versus displacement during tensile test of steel wire. Table 3-3 shows the maximum loads and tensile strength of the fibre.
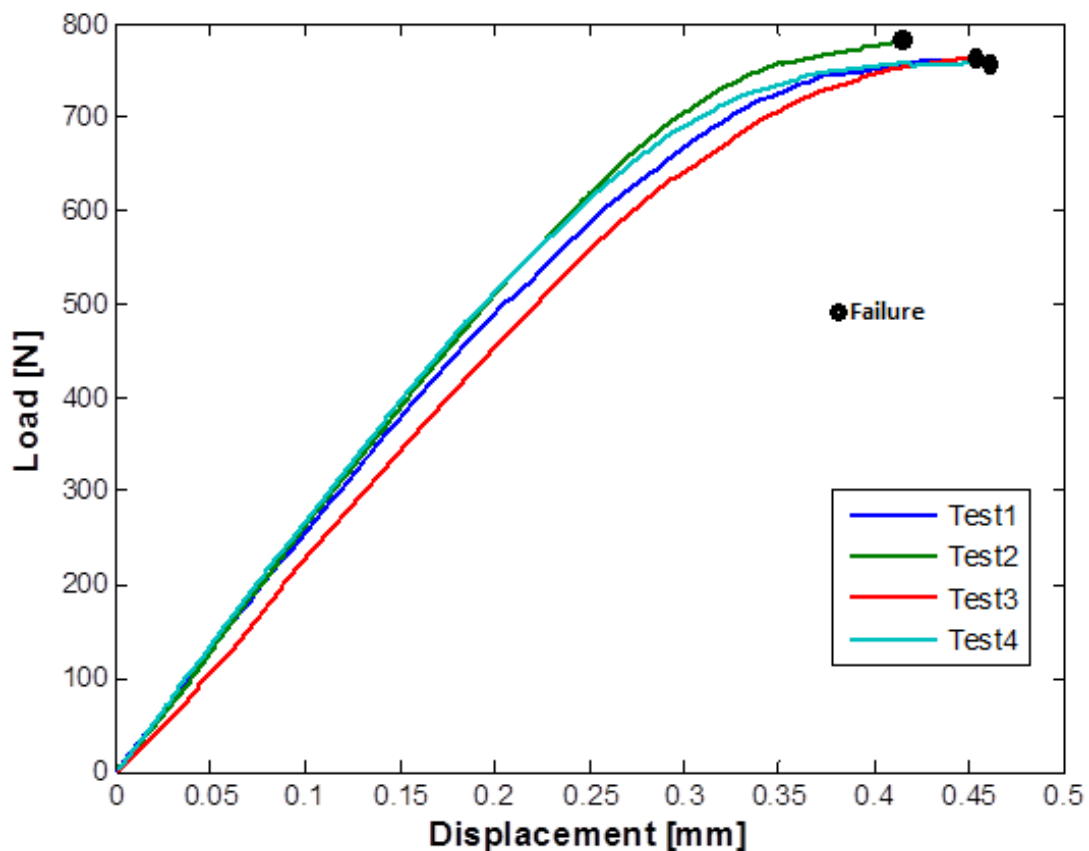
Figure 3-10. Tensile test of steel wire prior to be cut and shaped into hooked end steel fibre-Displacement measured by a gauging device (clip gauge).

Table 3-3. Tensile test results of steel wire.

Test	Max Load [N] P_{max}	Tensile strength [MPa] σ_u
1	762	1198
2	779	1225
3	765	1203
4	759	1193
Standard deviation	9	14
Average	766	1205

Figure 3-11 illustrates the tensile test results of hooked end steel fibre (blue dotted line) on the same axes with results of steel wire (red continuous line). Comparison made between these two series of data, reveals that there is discrepancies in terms of peak loads (ΔN) and displacements (represented in this case as a rate of the machine displacement and gauge length: Δε) at failure, as seen in Figure 3-11. Tensile tests performed directly on steel fibre exhibit higher magnitudes (loads and displacements) than the tests on wire. Note that the

difference between the peak loads is tolerable because they are approximately in the same range, whereas the displacements are far out of range.
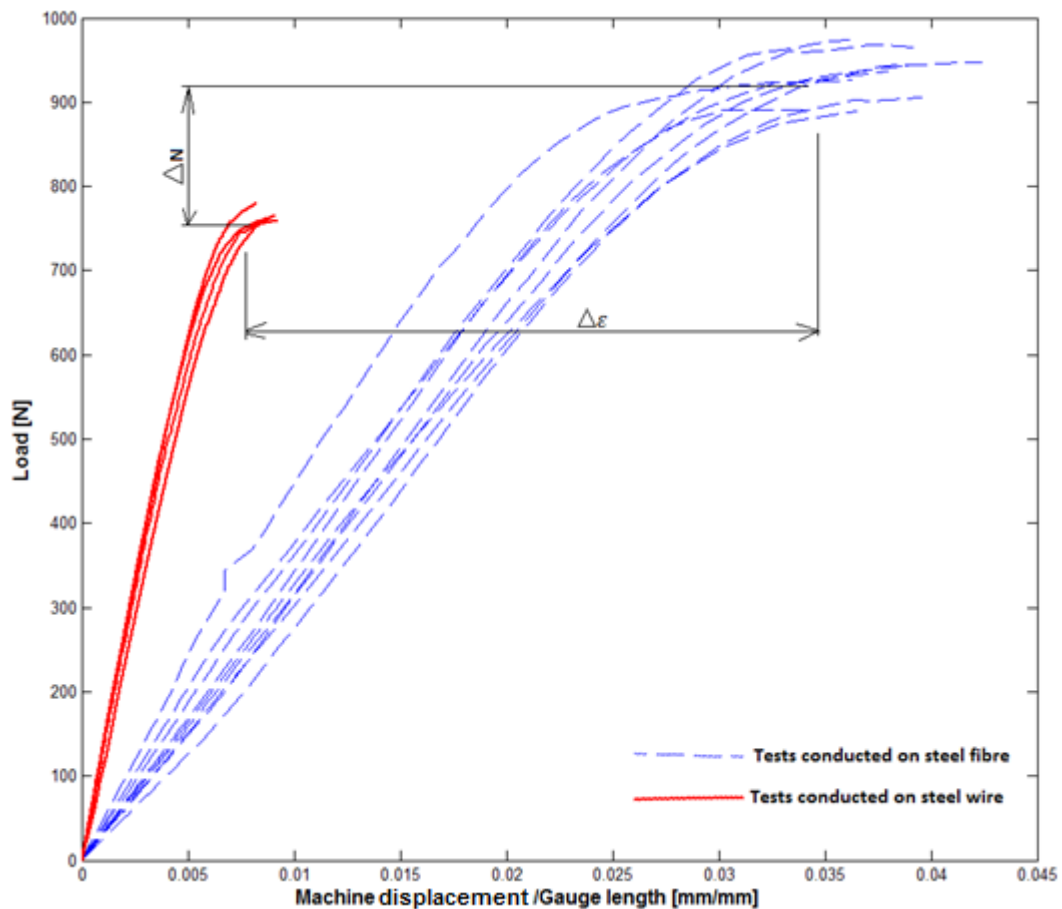
Figure 3-11. Comparison between tests conducted on steel wire and tests conducted on steel fibre.

These effects, displacement discrepancies, could be explained due to the fact that in the steel wire test the measured displacement is directly related to the intrinsic deformation of the fibre which is not the case for the hooked fibre test in which the displacement measured is related to the crosshead of the tensile testing machine. Therefore additional displacements due to extrinsic components, such as assemblies, gripping parts, etc., are also taking into account thus making the displacements larger than that measured for the steel wire.

Notice that even though huge displacement discrepancies arise between these two series of tests, (see Figure 3-11), there still a common feature observed for both series of tests. These graphs have all the same pattern, starting from zero the slope increase linearly up to a certain level then a slight curvature up to the maximum load.

To recap, the main aim of these tests is to determine mechanical characterisations of the fibre. Quantities of interest are the engineering stress, the engineering strain and Young's modulus which will result from the steel wire tensile test. The steel fibre tests have been discarded because unable to exhibit intrinsic behaviour of the fibre. And it has been made clear that the crosshead displacement is not an accurate measurement of deformation in the fibre as it includes the chain effects due to tolerance of mating components of the machine. Therefore, the tensile response defined by the test results of hooked end steel fibres does not perfectly illustrate the behaviour of the fibre.

The elastic modulus (Young's modulus) is evaluated by considering the stresses and strains at two points (A and B, see Figure 3-12) on the linear portion of the curve where the deformation is predominantly elastic (Dowling, 2013). For solids that obey Hooke's law ($\sigma = E\varepsilon$), the Young's modulus is termed to be the ratio of tensile stress (σ) to tensile strain (ε). That is, for these two points (A and B) the Young's modulus is given by the following expression:

$$E = \frac{\sigma_B - \sigma_A}{\varepsilon_B - \varepsilon_A}$$

(3-1)

For accuracy and standardization reasons, data points were taken for each curve (test) at almost the same stresses (220 MPa and 420 MPa, respectively for points A and B) with their corresponding strains. Again the standard deviation has been calculated in order to check whether or not the results are close to the mean value. The results are reported in Table 3-4.

Table 3-4. Young's modulus calculation of steel wire.

Test	ε (x10^{-3})		σ [MPa]		E [GPa]
	A	B	A	B	
1	1.068000	2.153000	214.688	455.362	191.556
2	1.110800	2.099200	220.396	422.639	204.617
3	1.340766	2.414626	220.688	422.116	187.574
4	1.084000	2.085000	220.040	422.150	202.009
Standard deviation					8.172
Average					196.439
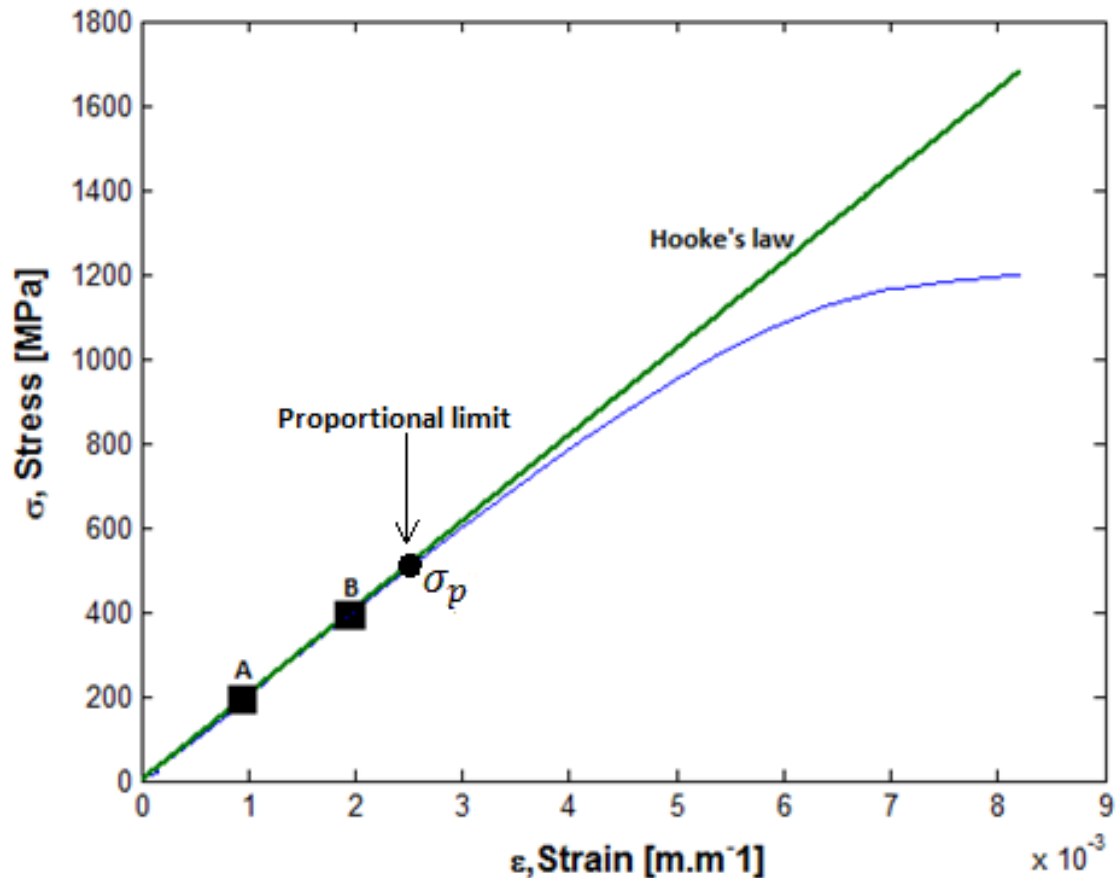
Figure 3-12. Stress-strain curve for steel wire in tension showing the linear part of the curve where Hooke's law can be applied.

The last remaining quantity of interest is the yielding point which is a point where plastic deformations start in the material. By definition the yielding point is defined as the point where the departure from linear-elastic behaviour occurs. Amongst several methods of yield event characterisation, the proportional limit method was applied in finding the yielding point (Dowling, 2013). This method consists in drawing a straight line that has a slope equal to the Young's modulus, and superimposing it on the stress-strain curve. The point where the first departure from linearity occurs is termed to be "*the proportional limit*" represented by $\sigma_p = 480$ MPa (see Figure 3-12).

3.2.5. Remarks

It can be observed in Figure 3-12 that failure occurs at very low strains and the ultimate stress (or peak stress) is equivalent to the tensile strength (which is the stress at which the fibre has failed). Such response suggests a material with ductility (Dowling, 2013). Further investigation of the fibre behaviour has been conducted in order to know exactly whether the response is brittle or ductile. Study of the fracture surface (fractography) has been performed by taking a magnified picture of the surface of the fibre by means of a Scanning Electron Microscope (SEM). A picture photographed in the centre of the fibre's fracture surface is shown in Figure 3-13 which is fairly characterised by fine dimples morphology. This is a characteristic of a ductile behaviour (Tillova *et al.*, 2010). In addition, we know that the hooked fibres have undergone considerable plastic deformation during the forming process, confirming that the material is capable of ductile behaviour. It is possible that the tensile test may not be an appropriate way to characterise the plastic behaviour of steel fibres.
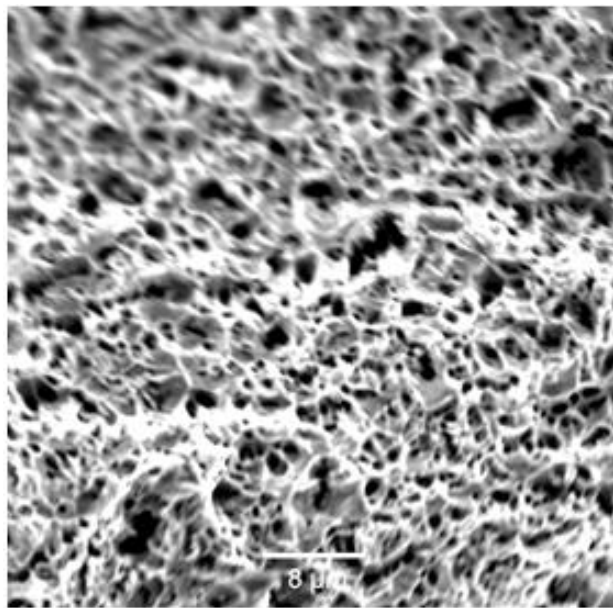
Figure 3-13. Magnified picture, up to 8μm, of the centre of the fibre's fracture surface-Picture taken by means of Scanning Electron Microscope (SEM).

3.3. Characterisation of epoxy

Contrary to previous characterisations which were directly conducted on a final product (hooked end steel fibre or steel wire), in the current case the specimen (epoxy) had to be primarily manufactured based on different raw materials. Then after fabrication of the specimen, mechanical properties of the resulting product were performed with practically the same principles as those used for characterisation of steel wire but with different experimental setup as far as the gripping devices are concerned.

As far as the fabrication of epoxy matrix is concerned, different parameters had to be considered in order to obtain the required properties and qualities. The epoxy matrix was designed to have a clear appearance and a brittle response when subjected to tensile or compressive loading. The transparent appearance of epoxy was designed in order to visualise directly, with naked eye, the plastic deformation of the fibre's hook as the pull-out process evolves. Brittleness behaviour was attributed to the epoxy matrix in order to mimic plain concrete's behaviour when subjected to tensile or compressive loads. This required suitable selection of the raw material, epoxy resins and their corresponding hardeners.

The American Society for Testing and Materials (ASTM), code D638, has standardised the shape of specimens designed for tensile characterisation of unreinforced and reinforced plastics. The adopted standard shape is a dog-bone shaped (ASTM, 2002). The above mentioned shape (dog-bone) is being used in the current study.

3.3.1. Material definition and manufacturing process

3.3.1.3. Material selection

Manufacturing of epoxy matrix requires mixture of two different chemical products which are both high viscosity liquids, namely, the epoxy resin and polyamide hardener. Different operations were involved in the process in order to obtain the final product which was a plain epoxy in a dog bone shape.

There is a plethora of epoxy resin and hardener, their selection depends thoroughly on the properties needed for the resulting compound. Studies were conducted on different epoxy resin systems: CP25 (clear polyester resin) with Merck Catalyst hardener, LR151 with either EH16 or EH96 hardener.

The combination of clear polyester resin with Merck Catalyst hardener resulted in a very brittle compound but which was slightly amber (yellow-orange) in colour. In contrast LR151 resin combined both with EH16 or EH96 hardener produced a clear matrix, but the combination with EH16 gave a soft matrix. Therefore the combination of clear polyester resin with Merck catalyst, and the combination of LR151 with EH16 hardener were discarded. Only the combination of LR151 resin with EH96 hardener was considered since it complies with the user specifications. Supporting results for these decisions are presented in the following sections.

3.3.1.2. Mould preparations

Before any other operation took place, the first operation to be achieved in epoxy matrices manufacturing was the mould preparation. These preparations were mainly intended to ease the casting and then to facilitate, in the end, the removal of the final product from the mould (demoulding). The moulds used in this project were two types of dog bone shapes, one used for casting of small dog bones and the other for large dog bones. The mould preparations are the same for both types, only the mould preparations of small dog bones are presented herein for simplicity reasons.

The mould is composed of three separate parts as seen in Figure 3-14, two halves shaped like a dog bone as well as the base plate, assembled by screw. The base plate is made of cast iron whereas the two halves are made of bronze alloy.
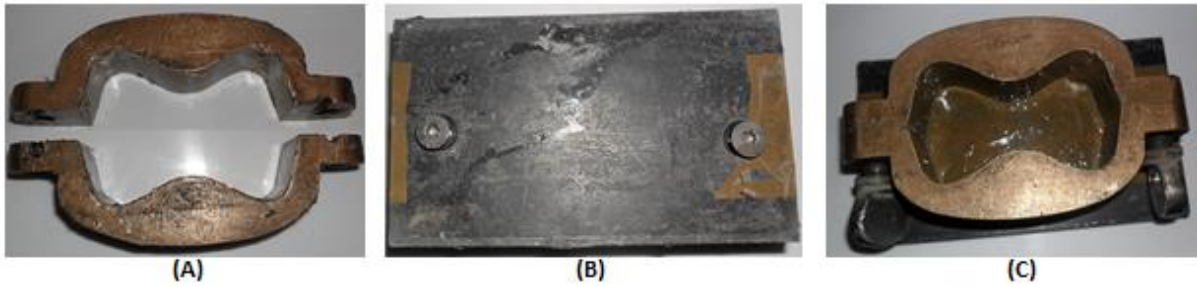
Figure 3-14. Mould composition. (A): Two halves dog bone shaped. (B): Base plate. (C): Mould.

The preparations consisted of a fine sanding of the inner surfaces of the parts of the mould in order to remove residual materials from previous castings. Next the inner lateral surfaces of the mould were overlaid by adhesive tape which overlapped the upper edges of the mould by approximately 20mm. This was done in order to prevent overflowing of the mixture during the vacuum (degassing) process (see section 3.3.1.4.). The interface between the base plate and the lower surface of the two halves of the mould was sealed by a self-adhesive foam sealing strip in order to prevent leakage of mixture. These operations are summarised in Figure 3-15. Finally a thin layer of Vaseline was applied all over the inner surfaces of the mould in order to ensure an easy release of the epoxy matrix (after curing) from the mould without sticking. After all was prepared, the mould was assembled by merely tightening the screws on each side.
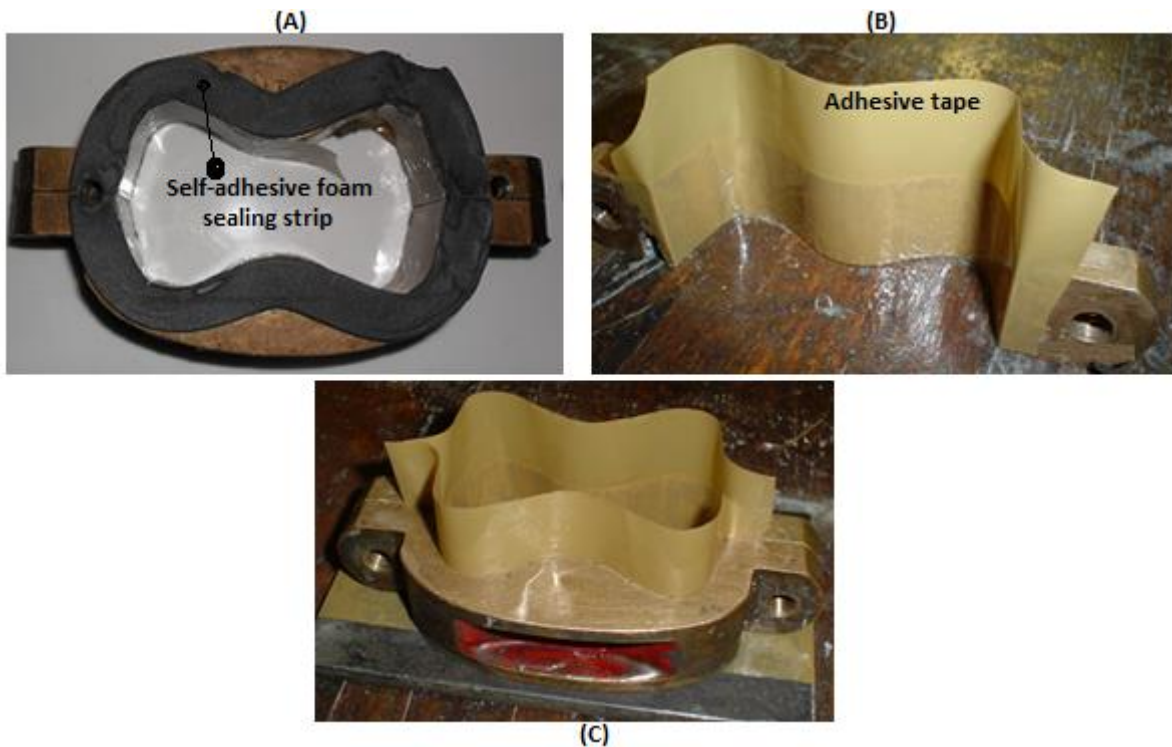
Figure 3-15. Mould preparations. (A): Foam sealing strip stuck to the lower surface of two halves parts. (B): Inner surface overlaid by adhesive tape. (C): Complete mould.

3.3.1.3. Mixing process

The mixing consisted, first, in measuring the resin (LR151) and the hardener (EH96) in the proportions that would result in a hard matrix. It was found that the ratio of $5\colon 1$ by volume gave the desired matrix properties. Knowing the volume of the mould in case of small dog bones, $64120 \text{ mm}^3 \sim 64 \text{ ml}$, and by taking into account losses during mixing the amount of resin (LR151) was chosen to be 64ml which subsequently results in 12.8 ml of hardener (EH96).

The epoxy resin (LR151) was first poured in a measuring cup up to 64 ml and then transferred into a mixing vessel. Next the hardener (EH96) was measured by means of a syringe and then transferred into the mixing vessel containing the resin. Afterward the mixture was stirred, for five minutes, with a spinning T-shaped steel rod (see Figure 3-16) held in the spindle of a portable drill. This process was performed in order to ensure the homogeneity of the mixture. During initial manipulations, it was noted that the mass or volume of the resin / hardener solution needs to be cautiously determined.
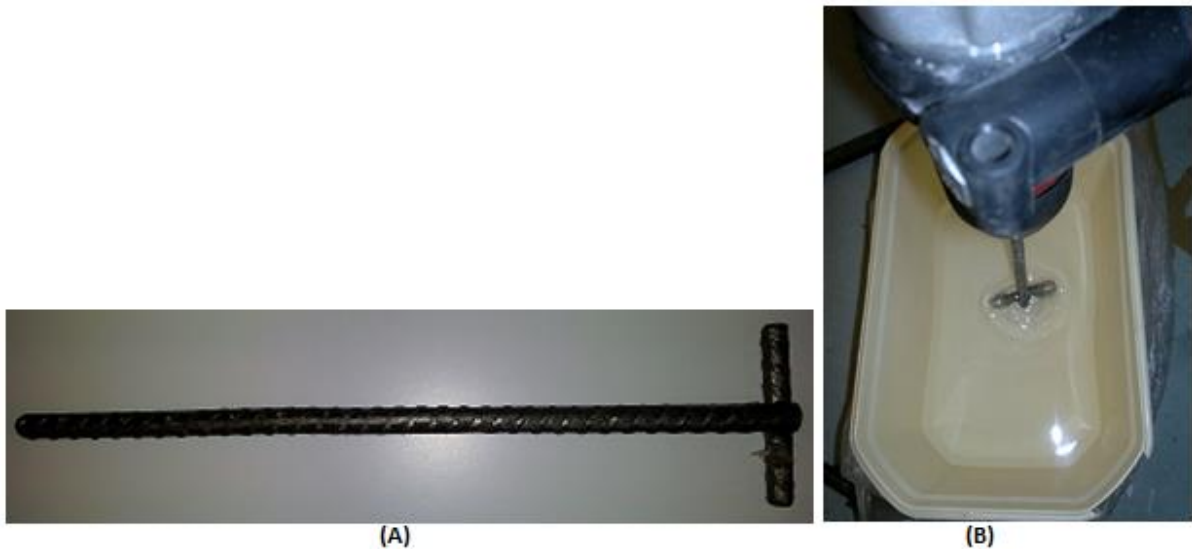
Figure 3-16. (A)-Mixer (T-shaped steel rod). (B)-Mixing process showing the mixture being stirred by the mixer held in a portable drill.

Two mixtures (different in volume) were prepared with the same mixing ratio $(5:1)$. The former was a $154\,\text{ml}$ solution of epoxy resin and hardener for half dog bone casting, whereas the latter was a $2582\,\text{ml}$ solution for cylinder casting. The former mixture was successfully achieved and resulted in two epoxy matrices. However, the larger volume mixture heated up and changed from clear to yellowish-brown. This is due to the exothermic reaction between resin and hardener, with a shorter chemical reaction time for larger volume. Therefore in order to prevent excessive heat generation during mixing process, small amount of solution should be used; otherwise the container should be surrounded by a running water in order to compensate for the heat generation effects and therefore to limit the temperature and the magnitude of residual stresses (Cook *et al*., 1989). Figure 3-17 shows in (A) single hooked end steel fibre embedded in an epoxy matrix resulted from a small mass, and in (B) a cylinder resulted from large mass of mixture. The difference between these two matrices is that in (A) the appearance is clear (transparent) whereas in (B) the appearance is yellowish-brown.
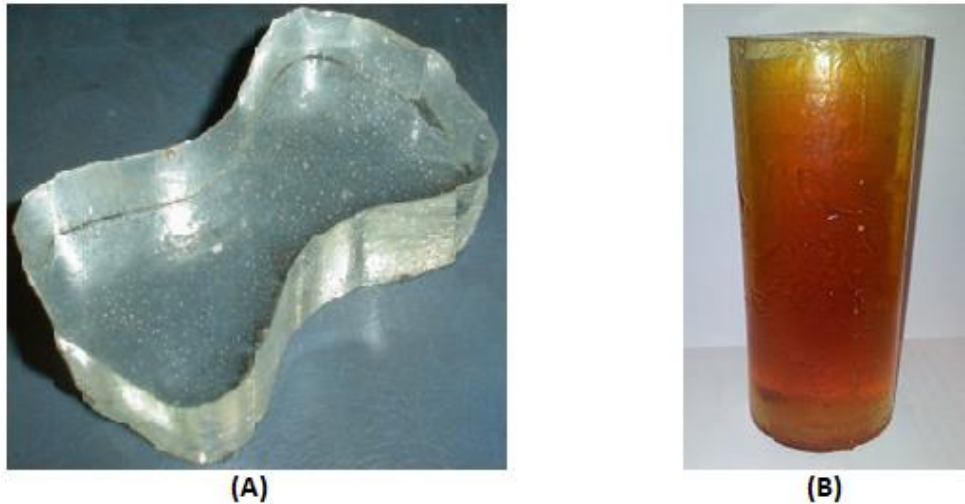
Figure 3-17. Appearance of the final product. (A)- Clear small dog bone, matrix obtained from small mixture (moderate heat generation). (B)-Cylindrical matrix made from large amount of solution (excessive heat generation).

3.3.1.4. Degassing process

During mixing of epoxy resin and hardener, there is air entrapped in the solution due to the turbulence in the mixture caused by the rotation of the mixer. If these air bubbles are not removed from the mixture they will create multiple voids in the matrix once it is cured. The final product, the compound epoxy matrix, should be void free, resulting in a compact and almost homogeneous material. The solution to removing air bubbles from the mixture is the degassing process. The mixture should be put in a vacuum chamber to undergo this operation. The degassing setup, illustrated in Figure 3-18, involves an Edwards vacuum pump (A), one liquid trapper (B), two vacuum chambers (C,D), plastic tubes (E), one two-way ball valve (F) and one three-way T-port ball valve (G).

The degassing process was achieved in two phases. First the mixing container was put in one vacuum chamber, and the other vacuum chamber was bypassed by means of the three-way T-port ball valve (G). Next the vacuum pump was switched on, after one hour the process was stopped and the mixing container was removed from the vacuum chamber. This first stage, called the pre-degassing process, dramatically reduces the air bubbles in the mixture before it was transferred into the mould. The second phase consists of transferring the mixture into two moulds. The mixture should not be poured from the mixing container to the mould for fear that air bubbles could be entrapped again in the mould, especially in the

remote places such as the bottom corners. The transfer from the container to the mould was thus achieved by means of a syringe.

After the two moulds were filled, they were separately put in the vacuum chamber. The pump was switched on again and after two hours the mixture was completely degassed, with all air bubbles removed from the mixture. It should be noticed that the degassing process took long to complete because the vacuum pump was worn out and thus had very low efficiency. The moulds were next removed from the vacuum chambers and allowed to cure at room temperature for 24 hours.
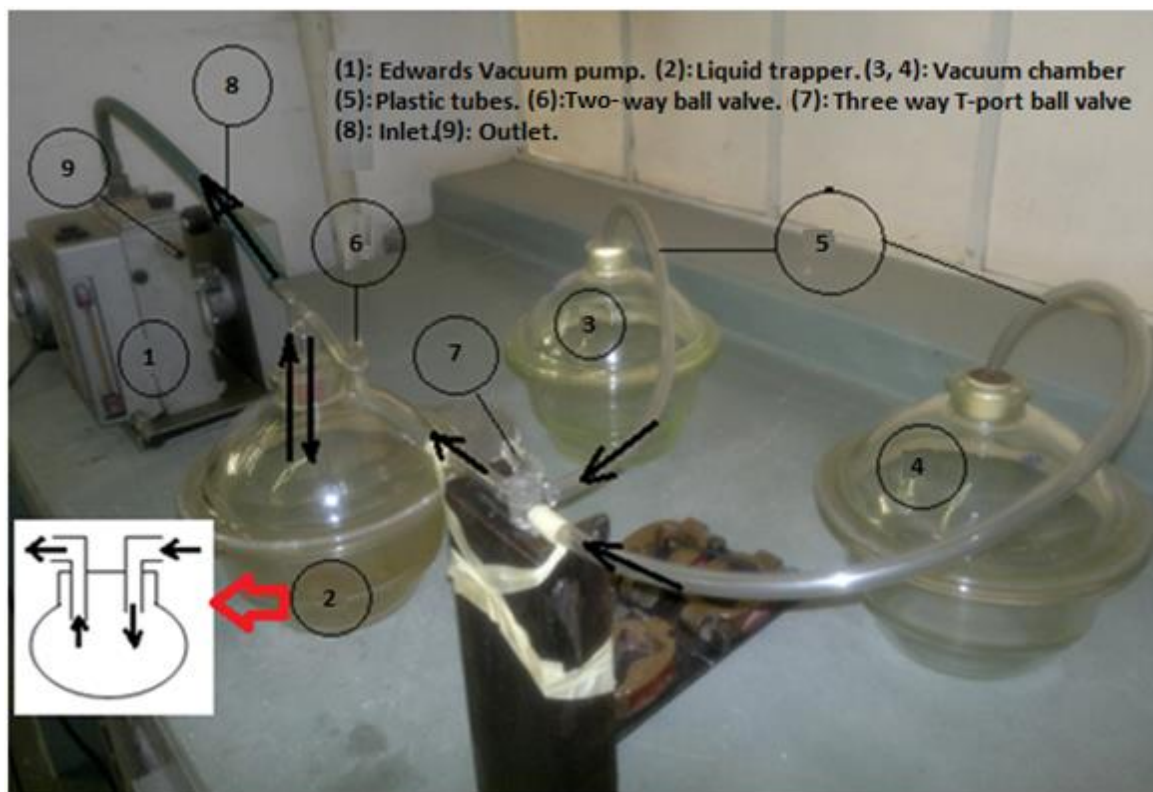
Figure 3-18. Degassing setup of the vacuum pump.

3.3.2. Experimental procedure

The goal in this current test was to determine the tensile strength and the Young's modulus of epoxy matrix. Notice that in this specific case the yield strength of the material was found to be of less importance and thus its evaluation was not performed. The material was characterised by performing two tensile tests conducted on two different epoxy specimens. Two dog bones, identified as small and large (see Figure 3-19), were cast from the same

mixture of epoxy in order to have the same properties. Evaluation of tensile strength was conducted on the small dog bone whereas the Young's modulus was determined by means of tensile test results, in a form of stress-strain curves, of the large dog bone.
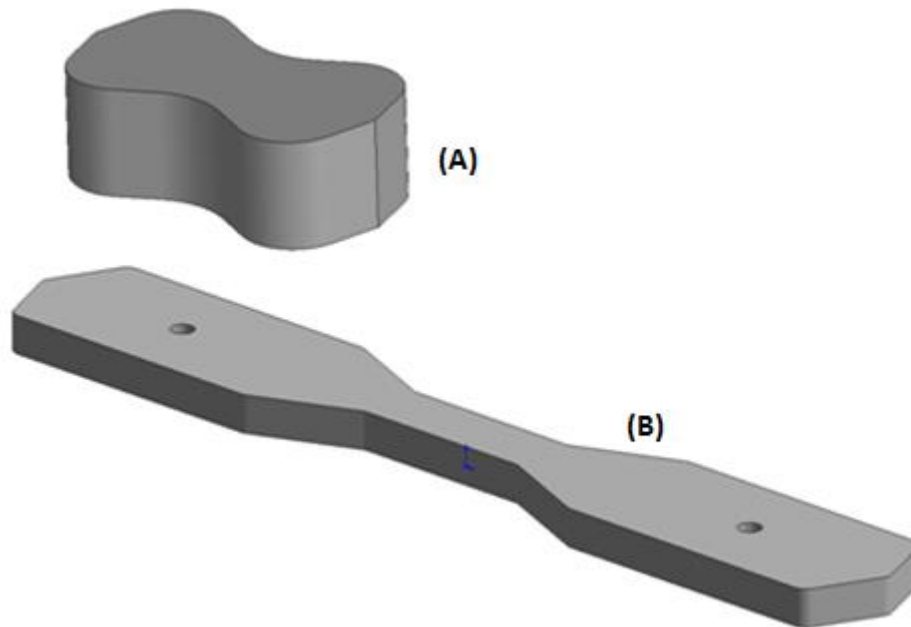
Figure 3-19. Sample specimens. (A)-Small dog bone. (B)-Large dog bone.

3.3.2.1. Experimental setup

The tests were conducted using the same tensile testing machine, as in previous section, but with different clamping systems. Hydraulic wedge action grips were replaced by two different grips depending on the sample that was used, small or large dog bone. The clamping system was adapted to the sample's geometry by merely using the mould which was used for casting. The mould is split in half and could thus form the upper and lower grips which are, respectively, pinned to the crosshead and fixed table of the testing machine (see Figure 3-20 (A)). The mounting of the specimen consisted firstly in inserting the sample into the lower grip and, secondly, in adjusting up or down the mobile crosshead of the machine in order to match the upper grip level with that of the sample which has to be inserted (see Figure 3-20 (B)).

The large dog bone sample was pinned to the tensile testing machine by means of a pair of pins and two metallic plates, as can be seen in Figure 3-21.

As stated earlier, these tests were conducted in order to determine the elastic modulus of the epoxy matrix. This will require a relationship between the stresses and strains. A gauging arrangement for measuring change in length is necessary. The same clip gauge used in previous setups has been utilised in the current setup, and the installation method is the same.
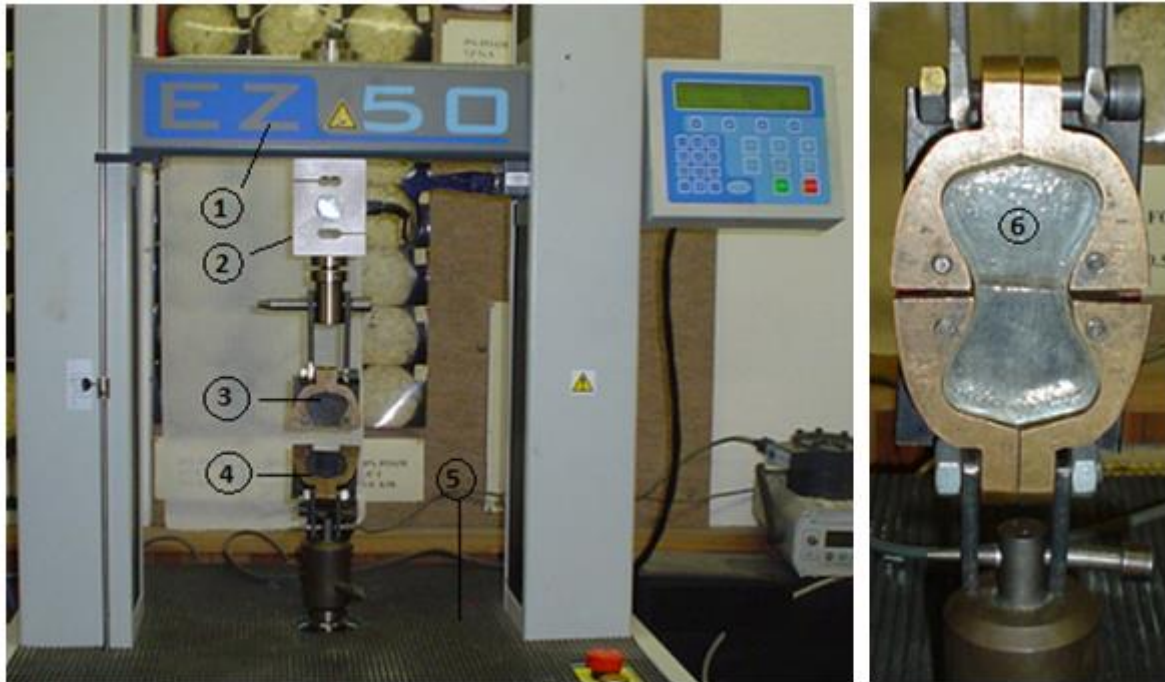
Figure 3-20. Tensile test of small dog bone-Experimental setup. (1): Crosshead. (2): Load cell. (3): Upper grip. (4): Lower grip. (5): Fixed table. (6): Sample.

For accuracy reasons, it was thought of placing the clip gauge in three different positions on the sample, thus leading to three different experimental setups. The clip gauge was placed for the first test on the right flank as shown in Figure 3-21(A), and then the machine was set to operate under a maximum load which was calculated to be the 20 % of the tensile strength of the epoxy. This was done in order to conduct the entire test under elastic conditions without plastic deformation of the sample. Once the machine was automatically stopped according to the setting, the clip gauge was removed and then replaced on the same sample but on another location: front face of the sample (Figure 3-21(B)). Then the second test was initiated under the same conditions as in previous test. The same was done for the third test which refers to the setup involving the clip gauge installed on the left flank of the sample (Figure 3-21(C)). This scheme was developed to access experimental accuracy. All data obtained from each and every setup will be compared. If the results are in the same

range then the setup would be accurate and the final result will be taken as the average of them all; but if discrepancies in the results exist, then the setup would not be accurate.
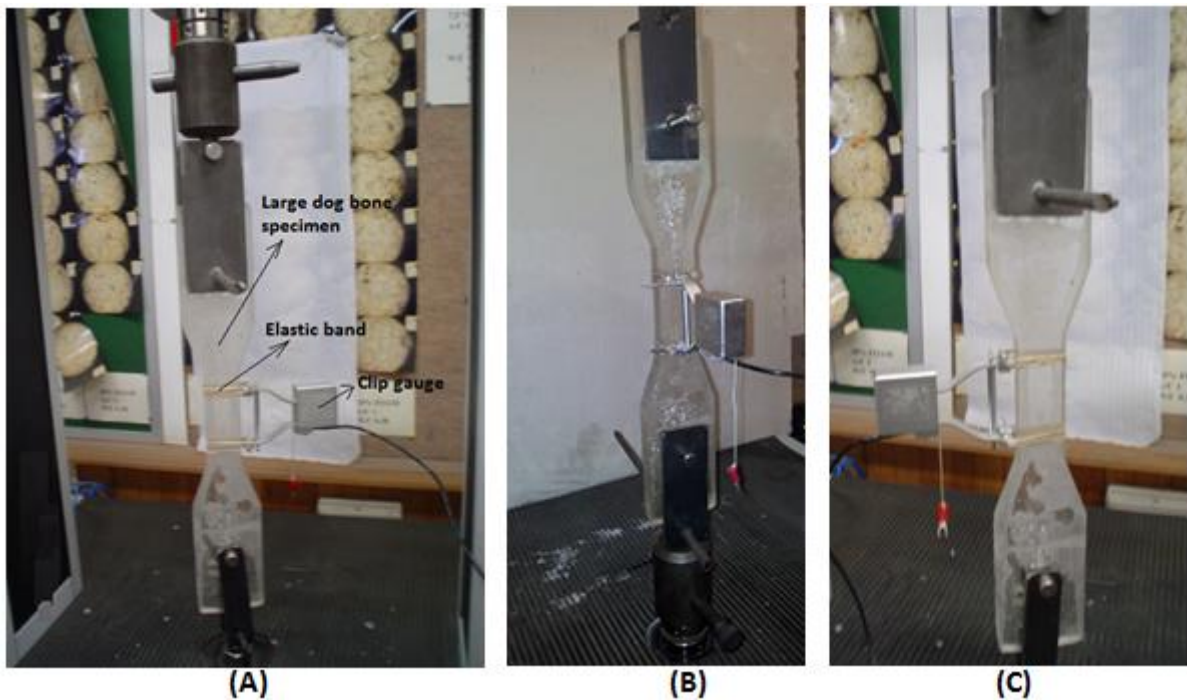
Figure 3-21. Tensile test of large dog bone-Experimental setup. (A)-Clip gauge on right flank. (B)-Clip gauge on front face. (C)-Clip gauge on left flank.

3.3.3. Experimental results

The scope in these tests was the evaluation of mechanical properties of interest of epoxy matrix. The tensile strength and Young's modulus have been determined in this thesis by means of tensile tests. The tensile tests provided qualitative and quantitative data to enable the choice of the appropriate epoxy resin and corresponding hardener. In order to reasonably approximate concrete, the epoxy matrix should be sufficiently stiff and brittle rather than ductile.

3.3.3.1. Strength of epoxy matrix

The three first tensile tests were conducted on three small dog bones of epoxy matrix manufactured respectively by combination of CP25 (clear polyester resin) with Merck

Catalyst (hardener), LR151 resin with EH96 hardener and finally LR151 resin with EH16 hardener.

Experimental results are presented in Figure 3-22, and reveal that matrices obtained by combination of CP25 resin with Merck Catalyst hardener and LR151 resin with EH96 hardener are hard and exhibit brittle behaviour when subjected to tensile test. Matrices made of CP25 resin with Merck Catalyst are even stiffer than the ones made of LR151 resin with EH96 hardener. In the former case the matrix failed at a maximum load of 16.7 kN whereas in the latter case the maximum load (failure load) is 10.4 kN. In contrast, the combination of LR151 resin with EH16 hardener resulted in a compliant and ductile matrix. When tensile loads were being applied to this specimen it experienced large deformations (see Figure 3-23). The sample was continuously elongating until it slipped out of the grip (half dog bone mould) due to Poisson contractions.
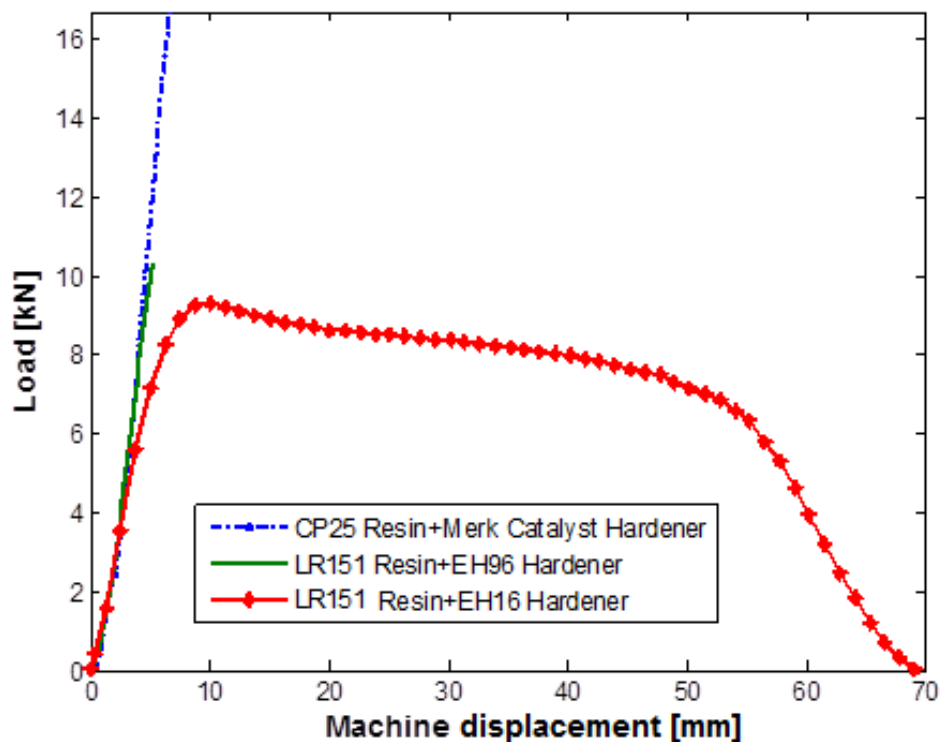
Figure 3-22. Tensile test of epoxy matrices, results for illustrating the matrix behaviours.

Ideally the epoxy matrix needed should be hard and clear. It can be observed, from results presented in Figure 3-22, that only matrices of CP25 resin with Merck Catalyst hardener and LR151 resin with EH96 hardener satisfy the first criterion, therefore they could be used in pursuing the scope of trying to simulate the concrete matrix. When it comes to the

appearance of the matrix, matrices of CP25 resin with Merck Catalyst hardener are not clear thus is not in accordance of the purpose of this study, as far as the appearance of the matrix is concerned. That is, only matrices made of LR151 resin with EH96 hardener are used in this thesis.

Before tensile test   **After tensile test**

Figure 3-23. Appearance of an epoxy matrix (made by combining LR151 resin with EH16 hardener) showing excessive elongation (deformation) after being subjected to tensile loads.

During the tensile test of epoxy specimens, it was observed that the matrix of CP25 resin with Merck Catalyst hardener crushed when maximum load was reached (16.7 kN) whereas the matrix of LR151 resin with EH96 hardener broke in the middle when maximum load was reached (10.4 kN). The dimensions of the middle of the specimen, which broke in the middle, are such that the width is equal to 25.77 mm and the height is 24.04 mm (see Figure 3-24), therefore the cross section area is found to be $619.51 \times 10^{-6} \, m^2$. Thus the mean tensile strength of the epoxy matrix is equal to:

$$\sigma_{u-m} = \frac{10.4 \, kN}{619.51 \times 10^{-6} \, m^2} = 16.8 \, MPa$$

(3-2)
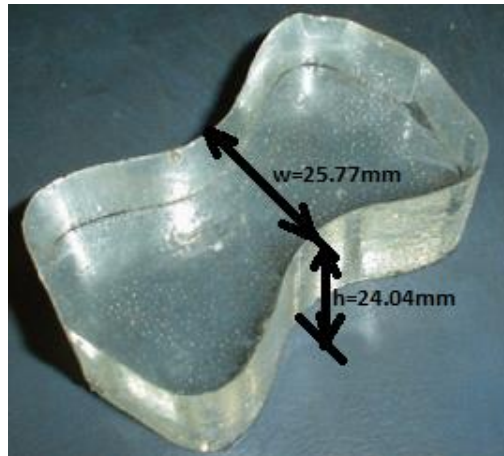
Figure 3-24. Dog bone dimensions at the failure area.

3.3.3.2. Elastic modulus of epoxy matrix

Tensile tests were conducted on two large dog bone samples. Load was recorded by means of the load cell of the tensile testing machine, and displacement was measured by an extensometer that was installed in different locations of the specimen. For accuracy reasons, three different tests were conducted on each sample according to the clip gauge locations (right flank, front side and left flank of the specimen) (see Figure 3-21). The tensile testing machine was set to operate at approximately 20 % of the epoxy tensile strength so that the entire test could be conducted under elastic region without any plastic deformation.

Six tensile tests were performed in total, three per specimen. The first two tests failed due to the fact that problems were encountered in correctly placing the clip gauge on the sample, but the four remaining tests succeeded.

Results are shown in Figure 3-25, for the four successful tests (Sample 1-Test on the right flank (SP1-TRF), Sample 2-Test on the right flank (SP2-TRF), Sample 2-Test on the front face (SP2-TFF), Sample 2-Test on the left flank (SP2-TLF)). The elastic modulus was determined, and the results are given in Table 3-5.
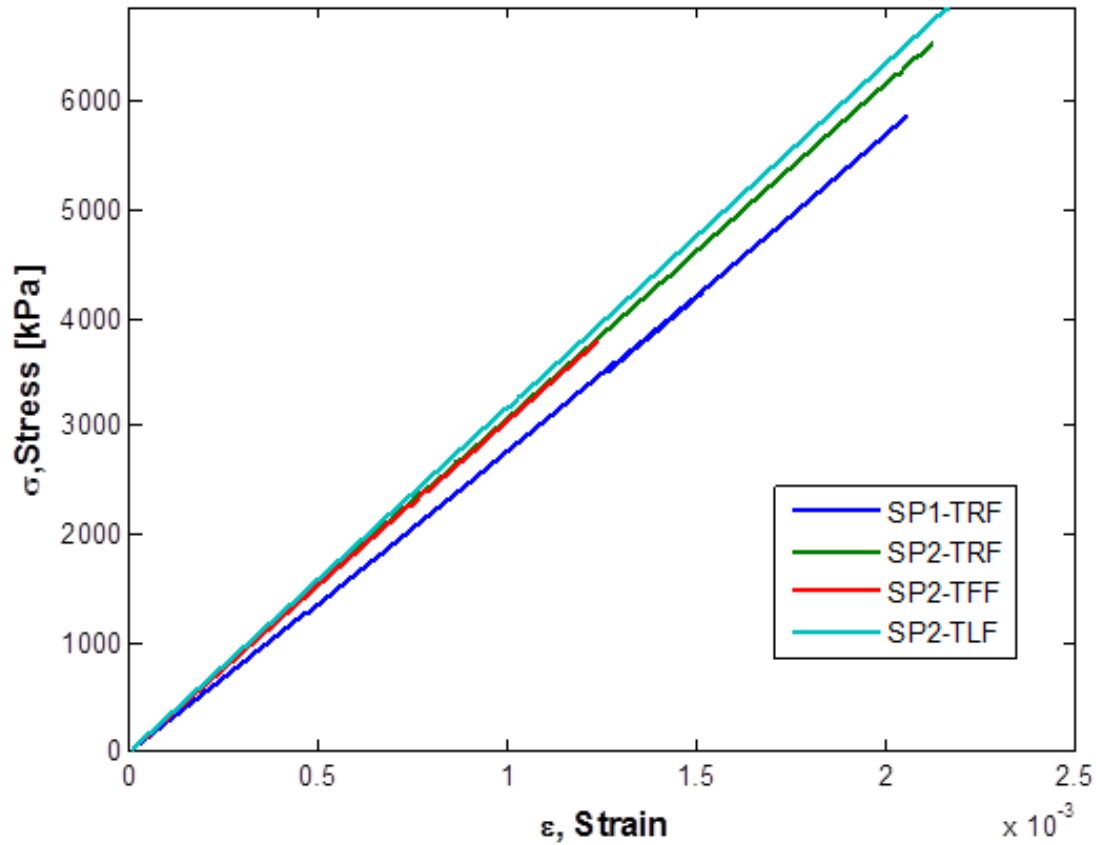
Figure 3-25. Stress-strain relationship, curves obtained by tensile tests of large dog bones.

Table 3-5. Evaluation of Young's modulus of epoxy.

Test	ε x10⁻³		σ [MPa]		E [GPa]
	A	B	A	B	
SP1-TRF	0.7287	1.4290	2	4	2.857
SP2-TRF	0.6500	1.3000	2	4	3.077
SP2-TFF	0.6547	1.2400	2	3.8	3.055
SP2-TLF	0.6313	1.2610	2	4	3.176
Standard deviation					0.134
Average					**3.041**

4. EXPERIMENTAL FIBRE PULL-OUT

In the current chapter, pull-out of hooked end steel fibre from a dog bone shaped epoxy matrix is presented. The main objective is to determine the experimental pull-out response in form of a graph of pull-out load versus fibre end displacement. Plastic deformation of the hook of the fibre is being correlated to the pull-out curve. In addition to the pull-out process, the embedment process of the hooked fibre in a dog bone matrix of epoxy is described.

4.1. Manufacturing process

In order to prepare specimens for fibre pull-out experiments, it was necessary to develop a technique to embed a single hooked end steel fibre in a half dog bone epoxy matrix, as illustrated in Figure 4-1. Notice that the hook of the free end was cut off in order to accommodate the casting procedure, and the embedded length of the fibre (l_f) is 25 mm.
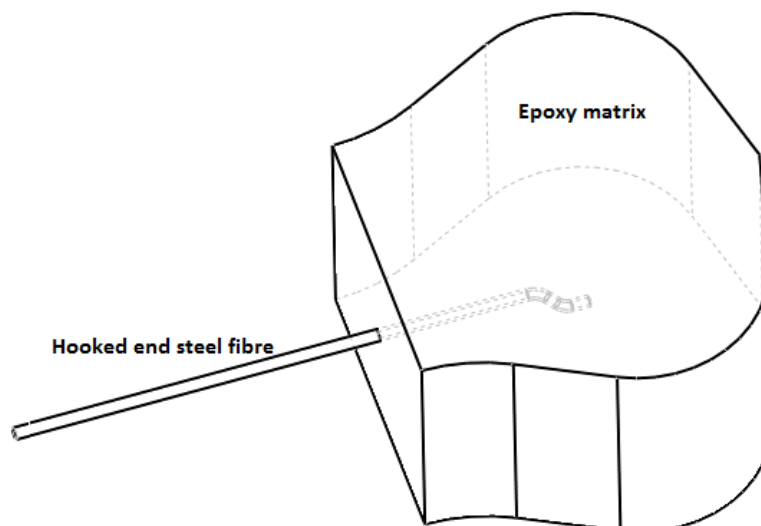
Figure 4-1. Hooked end steel fibre embedded in a half dog bone epoxy matrix.

Theoretically the embedment of a hooked end fibre in epoxy matrix could be achieved in three different operations. Boolean operation theory has been applied to three free-form solids (A, B and C as seen in Figure 4-2) bounded by parametric surfaces. The three solid bodies are respectively two half dog bones (A) and (C), and the hooked end steel fibre (B).
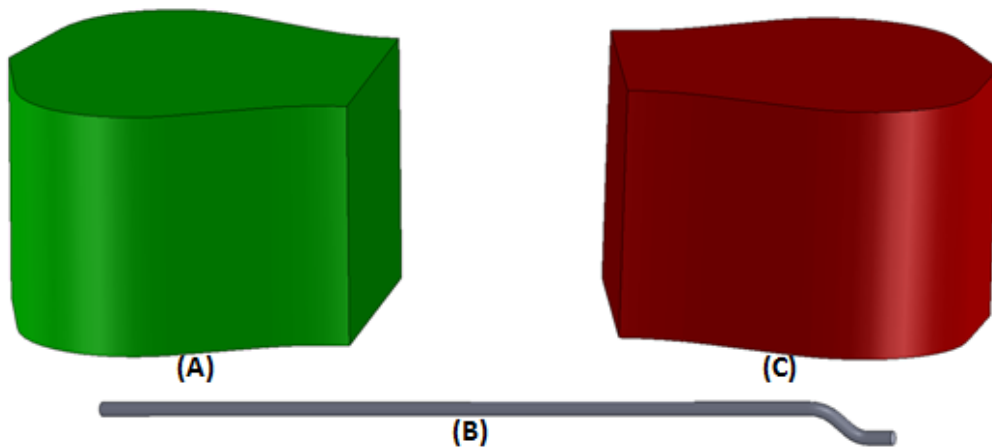
Figure 4-2. Solid bodies involved in the fibre embedment in half dog bone matrix. (A),(C)-Two half dog bones. (B)-Hooked end steel fibre.

The final composite, hooked end steel fibre embedded in half dog bone matrix, can be obtained by adding these three solid bodies (see Figure 4-3) and then by subtracting one of them at the end of all operations. These operations were conducted in the following order:

- Step 1 (union of all three solid bodies): $(A \cup B) \cup C = A \cup (B \cup C)$
- Step 2 (withdrawal of one solid body): $A \cup (B \cup C) \backslash A = B \cup C$
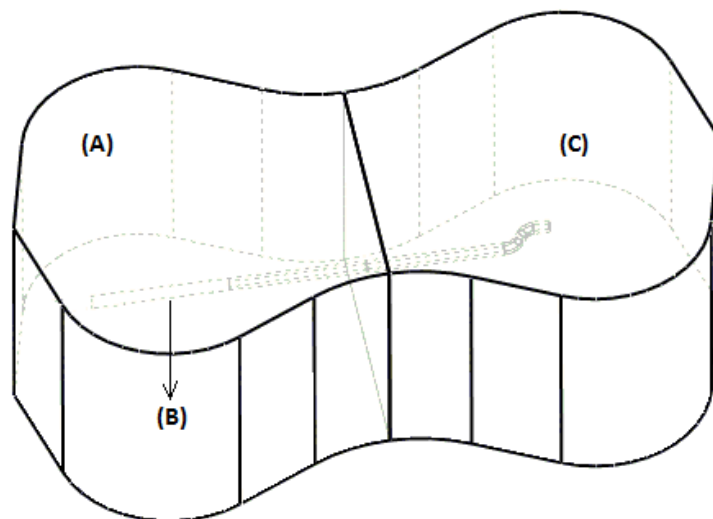
Figure 4-3. Unification of three solid bodies ((BUC)UA)).

The above theory was materialized by first fabricating the half dog bone represented by (A) (see Figure 4-3.). A plain dog bone specimen was normally cast, as explained in Section

3.3.1., and underwent the curing procedure for 24 hours after which it was cut in half. A 3.5mm diameter hole was drilled perpendicularly in the middle of the plane surface which is parallel to the cutting plane. This is illustrated in Figure 4-4.
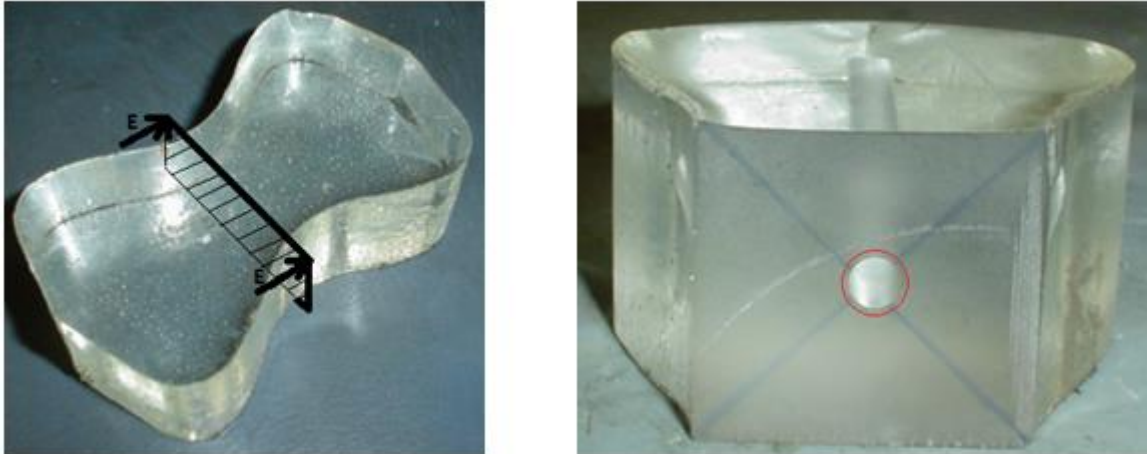
Figure 4-4. Plain dog bone cut in half. Left picture shows the plan of operation whereas the picture on the right shows the hole (3.5mm of diameter) drilled in the middle of the surface.

The first union, (AUB), consisted in inserting the free end of the fibre (end without hook) into the hole as shown in Figure 4-4. Axial alignment of the fibre's free end in the centre of the hole was guaranteed by soft paper wrapped all around; a layer of Vaseline was applied on top in order to facilitate the later separation of the fibre and the half dog bone matrix from the hole. Note that the soft paper wrapped around the fibre prevented the epoxy mixture from entering the hole.

Figure 4-5. Fibre's free end inserted in the hole of a precast epoxy matrix – First union (AUB).

Next the assembly (AUB) was placed in the mould as can be seen in Figure 4-6. The empty space (C) is where the mixture of epoxy will be cast so as to form one part perfectly bonded with the hooked end steel fibre.
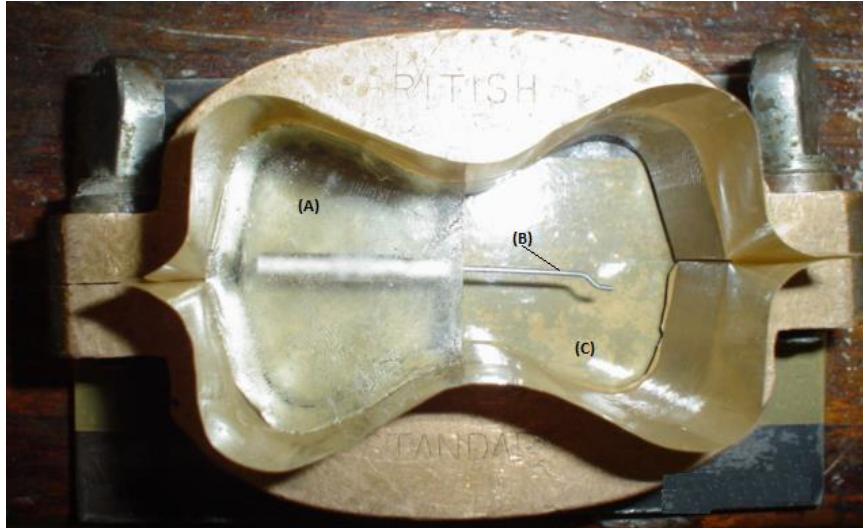
Figure 4-6. Preparation for casting of epoxy.

The compound was vacuum degassed for two hours and then was cured at room temperature for 24 hours, after which the assembly (BUC)UA was released from the mould. The last step consisted in a withdrawal of solid (A) which could easily slide off the free end of the fibre. The withdrawal of the precast half dog bone (A), resulted in a final product which is hooked end steel fibre embedded in a half dog bone epoxy matrix, Figure 4-7.

Figure 4-7. Final product – Hooked end steel fibre embedded in epoxy matrix.

4.2. Experimental setup

The composite specimen, hooked end steel fibre embedded in half dog bone epoxy matrix, was installed on the tensile testing machine as seen in Figure 4-8. The half dog bone matrix was held stationary in a half mould which was pinned at the fixed base of the tensile testing machine as was used in testing the epoxy alone (see Section 3.3.2.). The free end of the fibre was firmly held by means of hydraulic wedge action grips fixed to the adjustable crosshead as were used in testing the fibre (see Section 3.2.4.). In this configuration the epoxy matrix has been totally constrained in the x, y and z directions while the fibre is being moved upward as a consequence of the crosshead motion. This ensures that the failure of the fibre-matrix interface will be a mode II type of fracture.
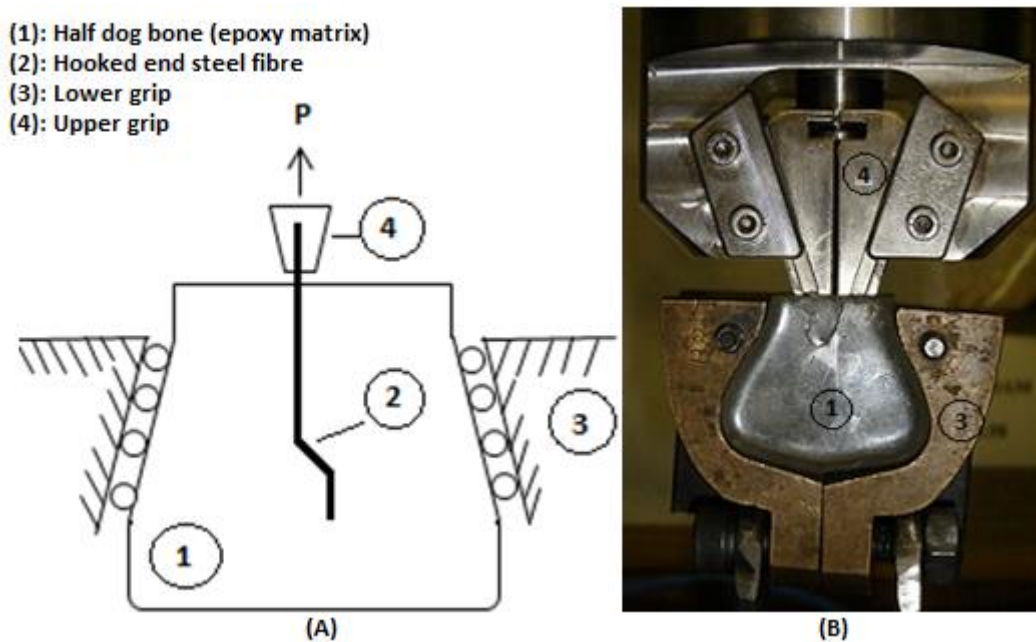
Figure 4-8. Schematic of the pull-out (A) and the pull-out experiment setup (B).

Two series of pull-out tests have been carried out, each series involving 3 distinct tests. As explained in Section 3.3.1., only two specimens could be cast at one time and only three samples could be cast per day. That is, for each series of tests, two specimens pertained to a single mixture and one was prepared with a different mixture but with the same volume ratio of the constituents. The fundamental difference between the set of specimens in to the first and second series is that they were fabricated on different days. Confusion has been avoided, in the results, by assigning all tests of a series by the alphabet "S" with suffix

"1" or "2" corresponding to the series number, followed by letter "T" which stands for test with suffix "1", "2" or "3" corresponding to the test number as listed in Table 4-1.

Table 4-1. Casting day of epoxy.

		Casting day	
		1	2
Mixture	1	S1T1	S2T1
		S1T2	S2T2
	2	S1T3	S2T3

4.3. Experimental results

The relationship between pull-out load and fibre end displacement for hooked end steel fibre pull-out from epoxy matrix is shown in Figure 4-9. The results show a similar appearance for different tests. In order to compare the different curves, it is helpful to develop a nomenclature to characterise key features of the pull-out response. Figure 4-10 shows a schematic view of the experimental pull-out process. The initial fairly linear increase in pull-out load is followed by a first peak load (P_{max1}) which suddenly drops to a first minimum (P_{min1}). The load increases again up to the second peak (P_{max2}) which afterwards drops dramatically to a second minimum (P_{min2}) followed by an almost constant phase (plateau).
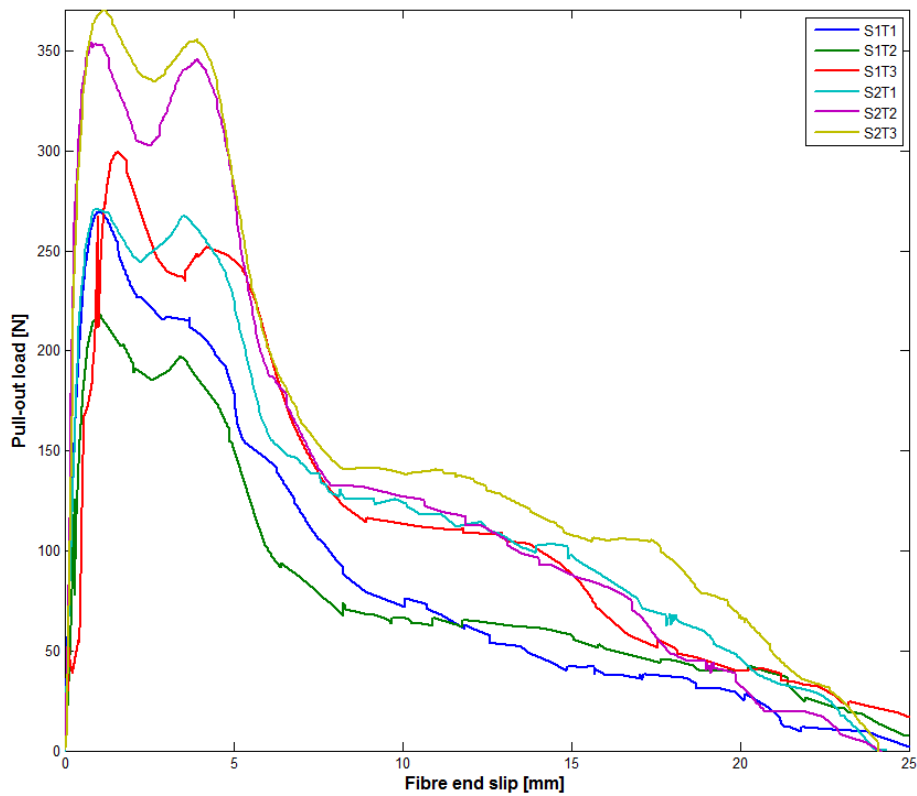
Figure 4-9. Typical experimental pull-out curves.

The constant zone only appears for a short period of time and incorporates small fluctuations in magnitude. In some cases, this plateau is immediately followed by a slight increase in load (P_{max3}) which drops to zero; but in other cases the plateau suddenly decays to zero without any increase in load, shown in Figure 4-10 by the dotted lines.

It can be observed, that for all these curves the first increase, linear, up to the maximum occurred rapidly for very small displacements of the fibre's end (1 mm approximately). On the other hand the minimum and the second maximum are respectively reached at roughly 3mm and 4 mm.

Table 4-2 summarises the pull-out results: the peak and minimum loads with the corresponding fibre displacements. Also included is the pull-out work which is the dissipated bond energy for the entire process and was merely determined by calculation of the area under each curve by means of trapezoidal numerical integration.
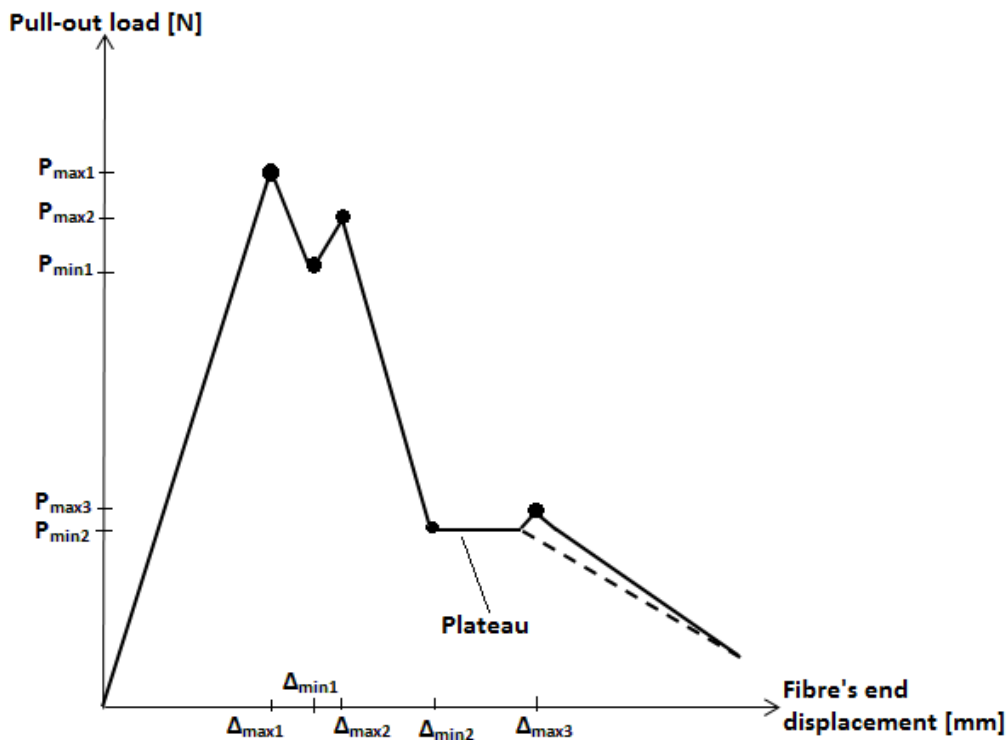
Figure 4-10. Schematic of experimental pull-out.

Experimental results for all six different tests have shown a similar pattern and thus the same pull-out behaviour. It can be observed from pull-out graphs in Figure 4-9., that discrepancies arise when comparing the peak pull-out loads (first and second) and this can be attributed to different parameters. The peak pull-out load is significantly influenced by the fibre-matrix interface bond which depends on the curing conditions and matrix strength (Tuyan and Yazici, 2012). The peak load can also be increased if the fibre was embedded in the matrix at an inclined angle instead of being straight (Lee *et al*., 2010).

The tests were conducted in two series and in different days. The first series comprises three specimens which were manufactured with different mixtures, two were of the same mixture and the other one was separately mixed. The results tabulated in Table 4-2 indicate that the pull-out response is not very sensitive to the epoxy mixture, as the comparison of S1T1, S1T2 and S1T3 to S2T1, S2T2 and S2T3 do not show similarity (in peak loads). Otherwise all tests of the same mixture would approximately have the same peak loads. These discrepancies could be as a result of the following parameters:

- Curing temperature (Tuyan and Yazici, 2012) which can vary, depending on climatic conditions;

- Time to set: specimens of series one were tested after one week whereas specimens of series two were tested after two weeks;

- Inclination of the fibre in the matrix: in the current study, inclination of the fibre could be, first, related to the surface inclination of the precast epoxy matrix (A) resulting in an inclination of the fibre and, second as a result of a misalignment of the free end of the fibre in the whole drilled in the precast matrix, see Figure 4-11.

A: Precast epoxy (which is not part of the final product)
C: Final product (epoxy matrix where should be embedded a single hooked end steel fibre
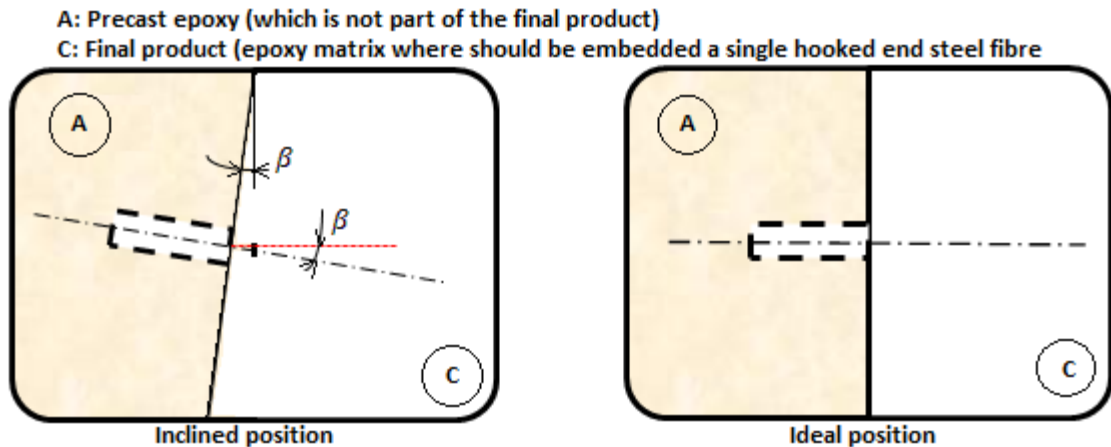
Figure 4-11. Relative positions of mating surfaces of the precast epoxy and the final product (epoxy matrix embedding a hooked end fibre).

On an energetic point of view, test 3 of the second series (S2T3) has the highest pull-out work (3.769 Nm), see Table 4-2. It simply implies that tremendous bond energy was dissipated to break the bonds (chemical and mechanical). This could be the result of a quite good bonding between the fibre and the surrounding matrix, or the fibre could be embedded at a more inclined angle.

Table 4-2. Comparison of pull-out curves for all six tests in terms of peak load, minimum load, fibre's end displacement and dissipated bond energy.

Test	P_{max1} [N]	Δ_{max1} [mm]	P_{min1} [N]	Δ_{min1} [mm]	P_{max2} [N]	Δ_{max2} [mm]	P_{min2} [N]	Δ_{min2} [mm]	P_{max3} [N]	Δ_{max3} [mm]	Pull-out work (dissipated bond energy) [J=Nm]
S1T1	268.9	0.9	215.4	2.9	216.5	3.7	73.8	9.8	N/A	N/A	2.2
S1T2	218.7	1.0	185.4	2.6	197.1	3.4	67.6	8.3	65.3	11.8	2.0
S1T3	299.8	1.5	235.1	3.6	251.9	4.2	114.3	8.9	110.9	11.8	2.9
S2T1	270.8	0.9	244.8	2.9	267.6	3.5	126.0	8.3	N/A	N/A	3.0
S2T2	353.4	0.9	302.5	2.5	345.7	3.9	132.7	7.9	N/A	N/A	3.3
S2T3	370.8	1.1	334.9	2.6	355.8	3.9	140.8	8.4	141.1	11.0	3.8

4.4. Microscopic observations

Pictures captured from a video recorded during pull-out enable direct visualisation of the different stages involved in plastic deformation of the fibre's hook. These stages comprise the times at which the first and the second peak loads (P_{max1} and P_{max2}) occurred, and the time when the tip of the fibre exit the second bend and is engaged in the straight channel of the matrix. Correlations of the fibre's positions, in the duct of the matrix, to the pull-out curve were achieved by means of timestamps recorded by the video camera as the pull-out process evolved. Figures 4-12 to 4-15 show the different stages of interest as the pull-out process evolves for test S2T3. Each figure shows a dot on the pull-out load-displacement curve, indicating the loading, as well as a frame capture showing the fibre. The tip of the fibre is indicated with an arrow.

Figure 4-12 illustrates the initial state; no load is being applied. Figure 4-13 illustrates the position of the fibre at the point at which the first maximum pull-out load (P_{max1}) is reached. The tip of the fibre is about to enter the first bend. At the second peak load (P_{max2}), the fibre tip is entering the second bend (Figure 4-14), and the second minimum (P_{min2}) occurs while the tip of the fibre exits the second bend of the matrix and then enters the straight channel of the matrix (Figure 4-15).
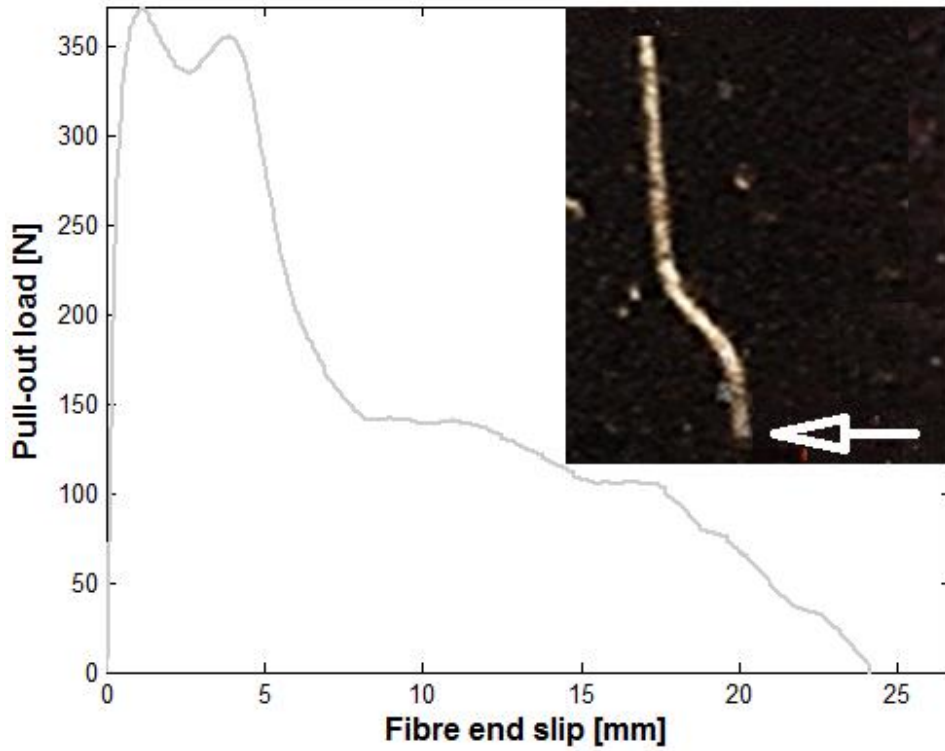
Figure 4-12. Fibre's positions in the matrix duct correlated to the pull-out curve. Stage 1: No load is being applied.
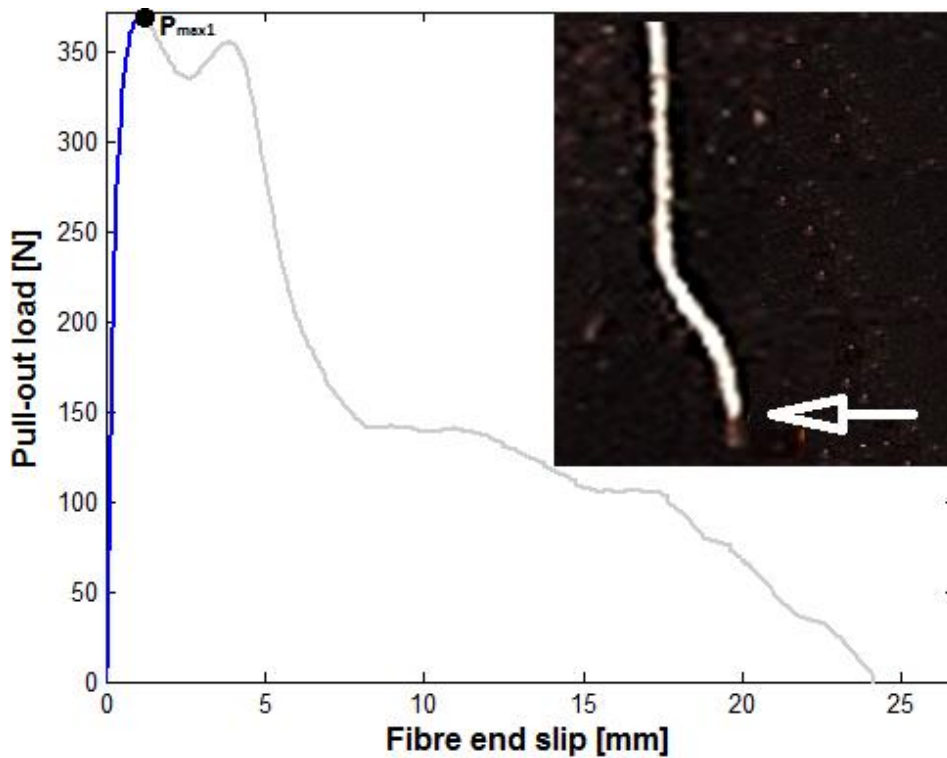
Figure 4-13. Fibre's positions in the matrix duct, correlated to the pull-out curve. Stage 2: Position at which the first peak load (P_{max1}) is reached.
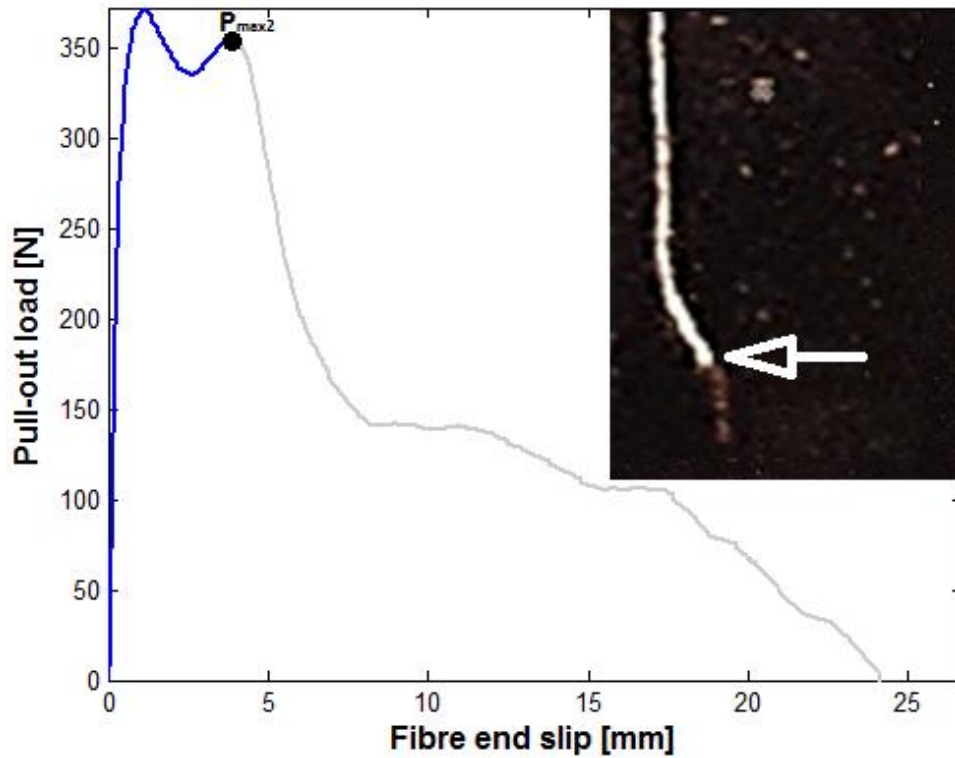
Figure 4-14. Fibre's positions in the matrix duct, correlated to the pull-out curve. Stage 3: Position at which the second peak load (P_{max2}) is reached.
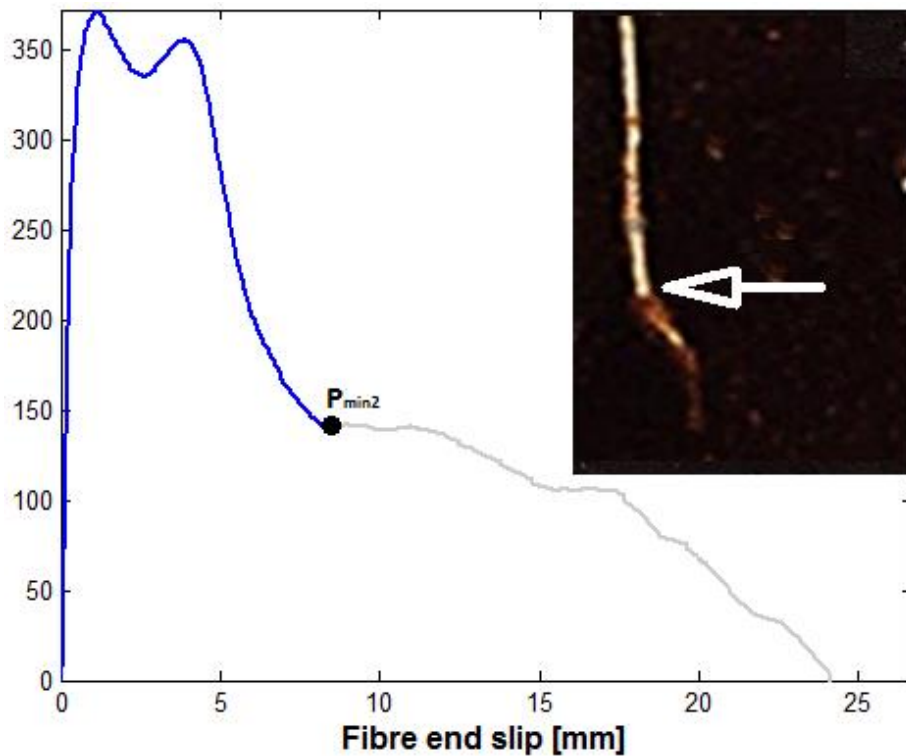
Figure 4-15. Fibre's positions in the matrix duct, correlated to the pull-out curve. Stage 4: Position at which the fibre exits the second bend and is engaged in the straight channel.

Microscopic observations of experimental pull-out have confirmed the veracity of peak pull-out load effects. Slight deformations (spalling) were observed in the near vicinity of curved parts of the epoxy matrix, as can be seen in Figure 4-16(A). Interestingly Figure 4-16(B) shows a broken piece of steel fibre in the oblique straight channel at exactly a position which defines the second peak pull-out load.
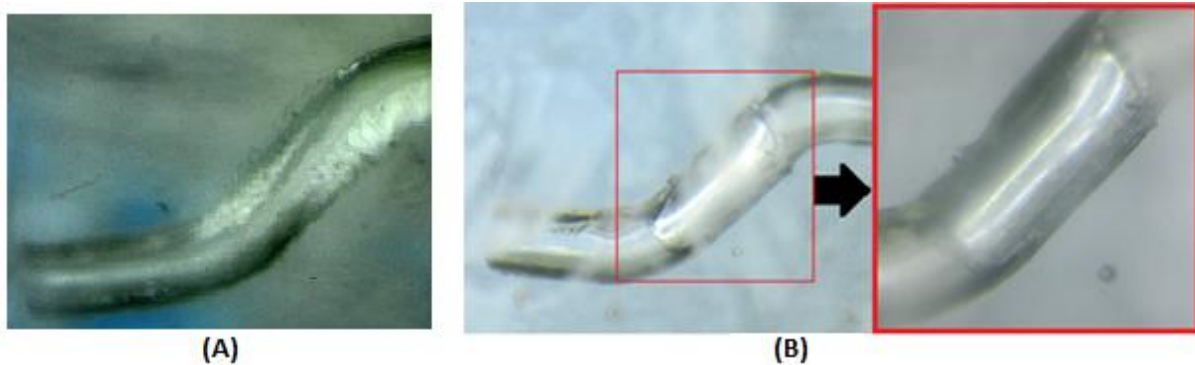
Figure 4-16. Microscopic observations of the pull-out effects on the composite. (A)-Magnified picture of the fibre's tunnel after the fibre has been pulled out, showing slight deformations at the bends. (B)-Picture showing a broken piece of steel fibre in the epoxy matrix.

4.5. Mechanism of pull-out

We are interested in understanding the physical process underlying the material response. The discussion here is for S2T3, as seen Figure 4-9. Initially no load is applied to the fibre (Figure 4-12). Once the load is being applied and as it increases, chemical bonds will break followed by breakage of mechanical bonds along the straight fibre matrix interface.

As stated by Alwan *et al*. (1999), the debonding started from the top point of the fibre (where the load was applied) to the bottom end of the fibre, far away from the applied load point, as seen in Figure 4-17. Other studies have revealed that two series of mechanisms are involved in the bond between fibre and matrix, the chemical bond (based on adhesive and frictional forces) and the mechanical bond due to the fibre's deformation (anchorage in the current case of hooked end steel fibre) (Banthia *et al*., 1992). The first stage in the pull-out process is breakage of chemical bonds between the fibre and the epoxy matrix.

The fibre is deformed elastically from the beginning of the pull-out process up to approximately 230 N, after which plastic deformation is initiated in the curved parts of the fibre. As the load increases, the first bend is forced to straighten and enter the vertical straight channel whereas the second bend is forced to enter the inclined channel, thus

leading to the first peak pull-out load ($\sim$371 N) corresponding to a the fibre's end displacement of approximately 1 mm.
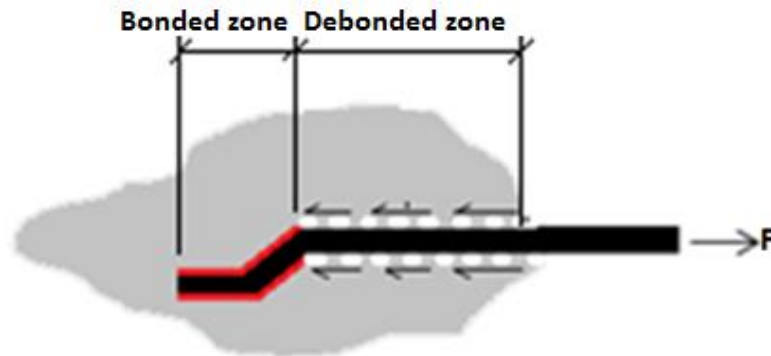
Figure 4-17. Pull out process showing where debonding, of the fibre from its surrounding, starts-(Alwan et al., 1999).

Other research has revealed that the first peak load occurs for a fibre slippage corresponding to half of the arc length of the bends (Laranjeira *et al.*, 2010). The first peak load contains contributions from the debonding of the fibre from the matrix, the initial plastic deformation of the fibre, and frictional resistance during pull-out. This is the state illustrated in Figure 4-13.

Once it has penetrated into the vertical and inclined channel, the fibre is only subjected to slight deformation and the pull-out process is more governed by friction, consequently the pull-out load decreases to a minimum ($\sim$356 N) corresponding to fibre slippage of roughly 3 mm. The pull-out resistance increases again when the last bend point is about to depart from the inclined channel to the straighten one (vertical). Subsequently the pull-out load rises to a second peak load (356 N) corresponding to a displacement of 4 mm, as shown in Figures 4-14.

At the time when the last bend is totally engaged in the vertical straight channel, there is less pull-out resistance, leading to a dramatic decrease of the pull-out load up to the second minimum (Figure 4-15). At this configuration the tip of the fibre is in a transitional stage, the departure from the inclined channel to the entrance into the vertical channel. In this particular stage the fibre's tip is bent and then straightened up in order to enter the vertical channel; consequently the pull-out process will be stabilized for a little while until the tip end is totally engaged in the vertical channel. The pull-out response, after the configuration presented in Figure 4-15, is only governed by the frictional sliding of the entire fibre and the residual resistance of the hook acting on the fibre's tunnel. This residual resistance is due to the fact that the so-called straightening of the hook is generically used; the truth of the

matter is the hook deformation during pull-out is incomplete. Figure 4-18 shows a fibre after being straightened during pull-out. As stated by (Laranjeira *et al.*, 2010), we can clearly see three points of the hook, two of which (G1 and G2) still have tiny curvature and the other one, G3, has a slight inclination. That is, the hook will slip in the horizontal, straight, channel with a three-point contact mechanism. This results in fluctuations of the curve which decays to zero as friction between the fibre and its surrounding is reduced.

Figure 4-18. Detail of hook geometry before testing (left) and after pull-out (right). -(Laranjeira *et al.*, 2010).

The pull-out process of a hooked end steel fibre from an epoxy matrix is summarised in Figure 4-19.
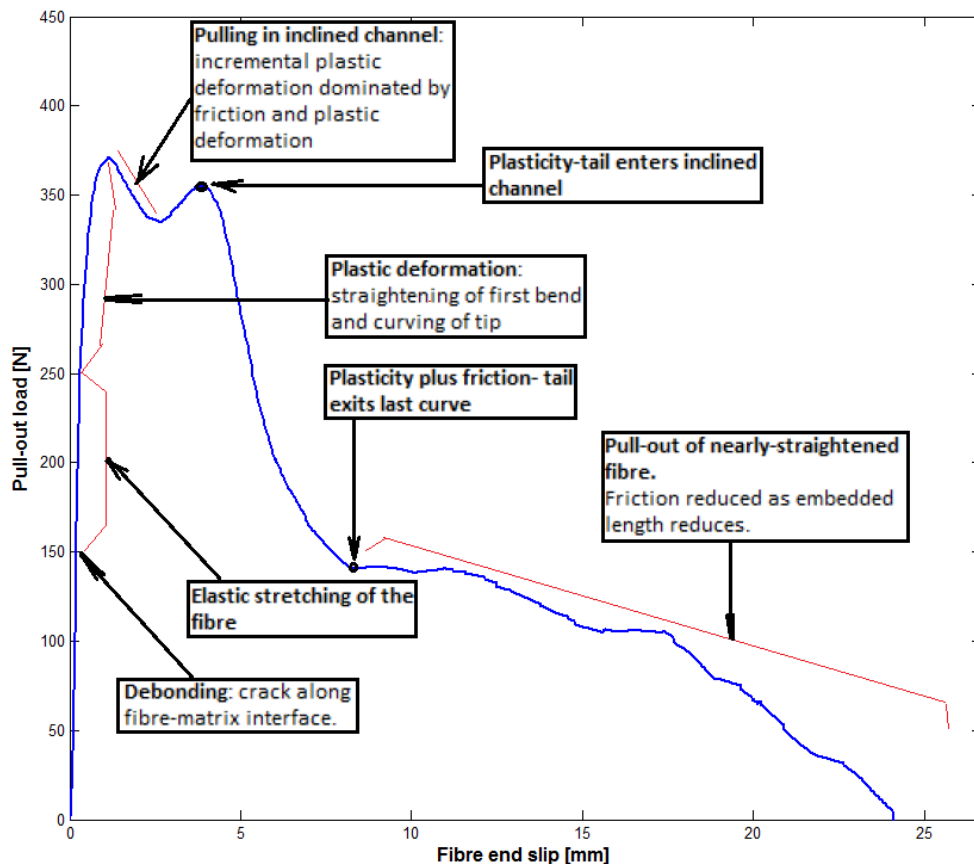
Figure 4-19. Summary of pull-out process of single hooked end steel fibre from epoxy matrix.

5. DEVELOPMENT OF NUMERICAL MODELLING AND RESULTS

The pull-out of a single hooked end steel fibre from an epoxy matrix is to be modelled numerically. A grasp of physical phenomena involved in experimental pull-out is of paramount importance. The key strength of the numerical modelling is that it can provide information of the pull-out that would have been quite challenging to determine solely from experiment. For example, it is quite difficult to predict experimentally the state of stress and strain involved in the composite. In the current study the stress-strain state and the deformation of the composite are going to be determined.

The main objective of the numerical modelling is to mimic experimental results presented in form of a curve pull-out load versus fibre end displacement so as to provide in the end different pull-out behaviours by means of different parameters that could not be provided experimentally.

Experimental results presented in Chapter 4 have revealed two peak pull-out loads which occur in the early stages of the pull-out. The fibre's position within the epoxy tunnel has been correlated with specific points on the load-displacement graph. The numerical modelling should provide similar information: the pull-out response correlated with physical phenomena.

5.1.   Key ideas from literature review

Research dealing with the numerical modelling of the pull-out / or push-out of a single fibre from a cementicious matrix gives insight into modelling choices, and is recapped here.

Modelling of the fibre push-out from a composite material was conducted by Lin *et al*. (2001). A cohesive model coupled with a frictional contact element was used, and the simulation was conducted under two steps including the residual stresses and the axial punch displacement. The axial load acting on the fibre was assumed to only be transmitted to the matrix through shear stresses acting on the interface; the fibre's end surface effects were neglected.

In order to take into account the nonlinearities of the physical model, Georgiadi-Stefanidi *et al.* (2010) analysed the pull-out of a single hooked end steel fibre from high strength cementicious matrix by using a three-dimensional finite element model. The bond strength between the fibre and the matrix was determined experimentally by pulling out a straight fibre and then the results served as input parameters to the numerical model. The physical problem was simulated by two deformable bodies (fibre and matrix). The debonding criterion was based on a yield surface defined by normal and shear strength of the interface. The contact and friction forces were taken into account by introducing unilateral contact and friction conditions between the fibre and the matrix. The von Mises plasticity criterion with an isotropic hardening rule for the expansion of the yield surface was used in the solution. Investigations of different frictional coefficient and the geometry of the hooked end of the fibre were performed during simulations.

A two-dimensional finite element model, of the pull-out of a single straight fibre from a cylindrical cement based composite, was conducted by Mobasher and Li (1998). An axisymmetric formulation was implemented and both the fibre and the matrix were assumed to have linear behaviour. The interfacial zone was characterised as a linear elastic third phase and the effect of residual compressive stresses due to shrinkage was simulated by a clamping pressure applied at the outer surface of the matrix.

5.2.   Modelling

A brief description of the physical model of the composite is presented. As seen in Figure 5-1, the composite comprises a single hooked end steel fibre embedded in a half dog bone shaped epoxy matrix.
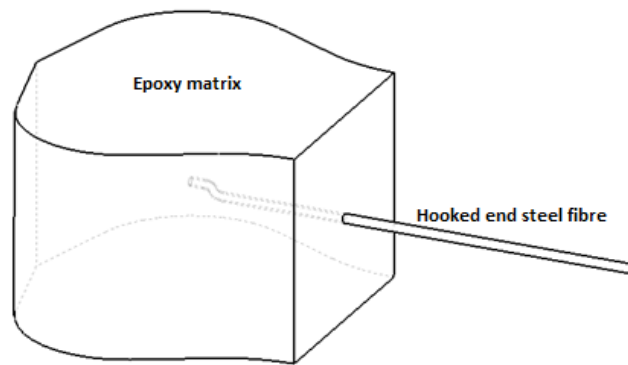
Figure 5-1. Single hooked end steel fibre embedded in a half dog bone shaped epoxy matrix.

At first glance it can be seen that the problem involves contact at the interface between the steel fibre and the epoxy matrix. The numerical model has been informed by the following key experimental observations:

- The fibre constitutive response exhibits both linear (elastic) and nonlinear (plastic) behaviour law (as shown in Figure 5-2);
- The hooked-end steel fibre undergoes extensive plastic deformation during straightening of the bends. This plastic deformation is driven by the contact between hooked end steel fibre and the epoxy matrix;
- After pull-out the epoxy matrix has remained in general intact without large deformation. The epoxy will be modelled as a linear elastic material;
- Resistance of the fibre to pull-out implies the presence of interfacial friction and / or cohesive bonding;
- Contact area between the fibre and epoxy matrix changes during the load history.

The above observations have shown that the physical model is nonlinear, and that accurate modelling requires plasticity and contact. Finite element analysis is being implemented on a static nonlinear three-dimensional model built in Solidworks 2011 and then imported as a Parasolid model in ANSYS Workbench release 14.0.
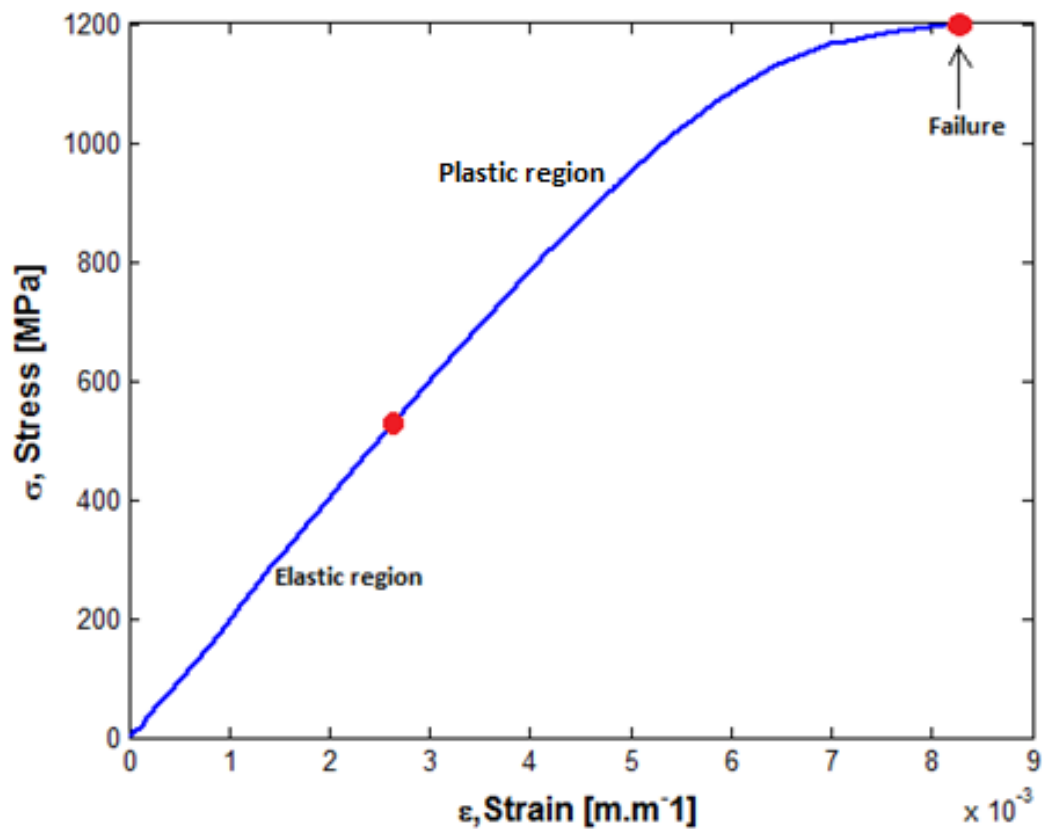
Figure 5-2. Experimental test (Stress versus Strain)-Tensile test of steel fibre showing both linearity (elastic region) and nonlinearity (plastic region).

This chapter describes the development of the finite element model. Completion of the modelling involved the following processes:

- Geometry;
- Meshing;
- Material definitions;
- Contact definitions;
- Boundary conditions and loading;
- Solution.

5.2.1. Geometry

The computational cost of the model has been reduced by substituting the dog bone shape of the epoxy matrix by a cylinder which is 35 mm in height and 10 mm in diameter. The

hooked end steel fibre was symmetrically embedded in the centre of the cylinder. Simplification of the model was justified under Saint-Venant's principle stating that "The stress, strain and displacement fields caused by two different statically equivalent force distributions on parts of the body far away from the loading points are approximately the same"(Martin, 2005). That is, the difference between the effects of two different, but statically equivalent, loads becomes very small at sufficiently large distances from the load. Moreover it has been pointed out in the literature review that the global geometry of the matrix does not influence the pull-out response (Tsai and Kim, 1996).

To take into account the contact between the steel fibre and epoxy matrix, the model comprises two different bodies assembled in one. The cylinder and hooked end fibre were built separately using the drawing software, Solidworks 2011. Next the fibre was symmetrically inserted into the cylinder. This required performing a Boolean operation by subtracting the fibre from the cylinder; consequently the cylinder was left with a hollow duct shaped like the hooked end fibre. Finally the hooked end fibre was inserted in the hollow duct and then assembled to the cylinder. The drawing of the hooked end fibre is shown in Figure A-1 (Appendix A).
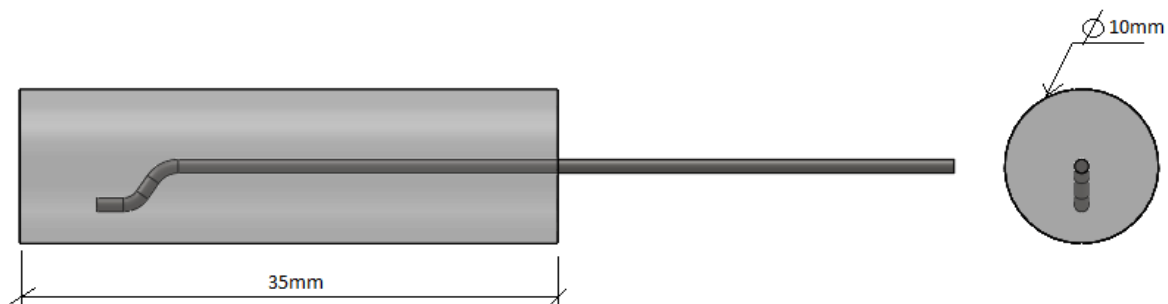
Figure 5-3. The model of a hooked end fibre embedded in a cylindrical matrix, used in the numerical analysis.

The model was saved as a Parasolid which is one of the formats supported by ANSYS Workbench release 14.0. Finally the model was imported in ANSYS for modelling and analysis purposes.

5.2.2.   Meshing

The finite element software, ANSYS Mechanical, has its own way of assigning different type of elements to specific cases, such as contact between surfaces, thus the elements used in this model were assigned by default. Only element sizes were altered. The types of elements used are:

- 10 noded quadratic tetrahedra (SOLID187) for the cylindrical body;

- 20 noded quadratic hexahedron (SOLID186) for hooked end steel fibre;

- 8 noded quadratic quadrilateral for the epoxy side of the interface surface (Targe 170).

- 6 noded quadratic triangular for the fibre side of the fibre-epoxy interface surface pertaining to the fibre (Conta174);

Table 5-1 summarises the different elements used for the model and indicates their corresponding designations in ANSYS (Mechanical APDL) and for other finite element software (NASTRAN and ABAQUS).

Note that the mesh sizing for the whole model was 0.35 mm, resulting in 12551 elements and 21814 nodes.

Table 5-1. Element type's summary.

Generic element type	Mechanical APDL	NASTRAN	ABAQUS
Type name	Name	Name	Name
Quadratic tetrahedron	Solid187	CTETRA	C3D10
Quadratic hexahedron	Solid186	CHEXA	C3D20
Quadratic quadrilateral	Targe170	N/A	N/A
Quadratic triangular	Conta174	N/A	N/A
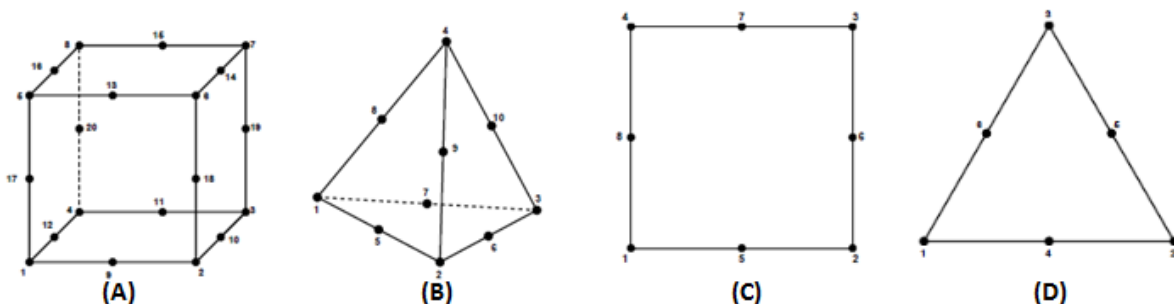
Figure 5-4. Type of elements used in the model - ((A): 20 noded quadratic hexahedron element; (B)-10 noded quadratic tetrahedron element. (C)-8 noded quadratic quadrilateral element. (D)- 6 noded quadratic triangular element. (Taylor, 2011).

5.2.3. Material definitions

Based on experimental results it is observed that the fibre admits plastic deformation during pull-out test (straightening of the bends) whereas the epoxy matrix does not encounter major deformation; only slight spalling was observed in the vicinity of curved parts. From this perspective two material definitions have been assigned for the model. The epoxy matrix is defined as isotropic linear elastic. The steel fibre is defined as a bilinear isotropic hardening material because of its plastic behaviour during pull-out. Table 5-2 shows a summary of material properties obtained from experimental results of both parts, hooked end steel fibre and epoxy matrix.

Table 5-2. Summary of material properties obtained from tensile test except Poisson's ratio.

		Epoxy	Steel fibre
Poisson's ratio	(v)	0.3	0.33
Tensile strength (σ_u) [MPa]		17	1200
Yield stress (σ_P) [MPa]		-	480
Young's modulus (E) [GPa]		3	196

It was initially planned to model the steel fibre as a multilinear isotropic hardening material. Plastic strains and corresponding true stresses had to be input in order to define the multilinearity behaviour attributed to the fibre. First, the true stresses and strains were converted from engineering stresses and strains as follow (Dowling, 2013):

$$\sigma_{True} = \sigma_{Eng}(1 + \varepsilon_{Eng}) \tag{5-1}$$

$$\varepsilon_{True} = \ln(1 + \varepsilon_{Eng}) \tag{5-2}$$

Next plastic strain at each point located on the true stress-strain curve was calculated by:

$$\varepsilon_{plastic} = \varepsilon_{True} - \sigma_{True}/E \tag{5-3}$$

Table 5-3 illustrates ten points selected on the curve (true stress-strain), starting from the yielding point, in order to define the plastic curve (true stress versus plastic strain) which has to be input into the software.

Numerical simulation with this material definition did not result in satisfactory results since the solution did not converge. The problem encountered during the simulation was that for very small plastic strains the corresponding stresses were so high, and exceeded the tensile strength of the fibre (1200 MPa) as it was defined in the material definition. These results

simply mean that the fibre is being broken at the early stage of pull-out because tensile strength is being reached and exceeded. This poses a dilemma in simulating the pull-out response of hooked end steel fibre from epoxy matrix. Experimental pull-out response has shown that the fibre has admitted plastic deformation and has straightened up without being broken; this confirms the result obtained in Section 3.2.5 stating that the tensile response of the fibre is ductile. The experimental fibre's multilinear isotropic definition seems to be not adequate in simulating the pull-out response, in this case.

Table 5-3. Ten points selected to define the fibre's plastic curve (multilinear definition).

Point number	True stress (σ_{True})	True strain (ε_{True}) x10^3	Plastic strain ($\varepsilon_{plastic}$) x10^3
1	481.903	2.4	4.7628E-02
2	685.5	3.443	9.67851E-02
3	850.9	4.359	0.205398
4	954.8	4.987	0.326218
5	1031	5.502	0.469254
6	1080	5.892	0.620064
7	1133	6.384	0.853349
8	1160	6.76	1.09755
9	1181	7.227	1.46204
10	1209	8.193	2.291361

Dealing with nonlinear finite element problem and being interested in finding satisfactory results, a single strategy may not be enough in pursuing the established goal, unless by chance. But sometimes satisfactory results can only be obtained after several attempts and change of strategies (Cook *et al.*, 2002). In an attempt to find the solution, the fibre's material definition was changed from multilinear isotropic hardening to bilinear (two straight lines) isotropic hardening (see Figure 5-5). This definition is simple since it only allows three inputs for its completion instead of defining data points for the whole curve in the case of multilinear definition. The parameters input for the fibre are the Young's modulus (E_f), yield stress (σ_Y) and the tangent modulus (E_T).
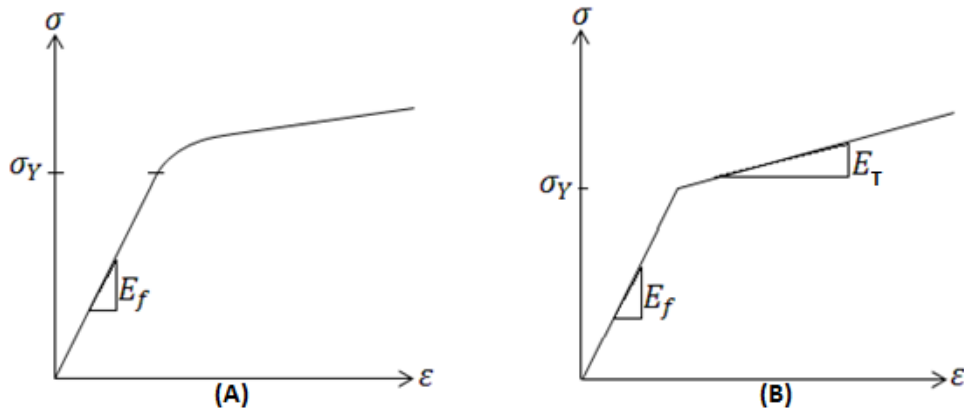
Figure 5-5. Stress-strain relationship for uniaxial stress idealised as: (A)-Multilinear. (B)-Bilinear.

5.2.4. Contact definitions

Contact is one of the major contributors to the geometrical nonlinearity in this problem. The numerical simulation is going to be thoroughly governed by principles which are directly related to contact matters; therefore accurate results will demand a good understanding of the phenomenon.

The ANSYS Mechanical program has two ways of assigning names to the pair of surfaces involved in the contact. One surface can be established as "contact" and the other as "target", which is respectively referred to as "slave" and "master" surfaces in other finite element packages (BHASHYAM, 2002). There are three rules for assigning a surface to be either a contact or a target:

➢ If the materials involved in the contact are the same, for rigid-flexible contact, the "contact" surface is always the deformable (the less stiff) surface and the "target" is the solid surface (the stiffer). But for flexible-to-flexible contact both contact and target surfaces are associated with the deformable bodies (ANSYS-HELP, 2009).

➢ If the pair of materials is the same then the contact surface is attributed to the body that has a finer mesh and the target is the other one with a coarse mesh.

➢ If the materials are the same and the mesh quality is quite identical, then the contact surface refers to the body of interest (the body where solution is needed) and the target belongs to the other body which is referred to as passive. In the case where the solution is needed for both bodies involved in the contact, symmetry is to be

© University of Pretoria

defined in the contact. The symmetry implies that during contact solution, the contacting surfaces will be alternatively assigned to be contact part so as to provide the solution for both bodies.

According to the above theory and based on experimental observations that the steel fibre is stiffer (E_f = 196 GPa) than the matrix (E_m= 3 GPa), the first criterion is applied. The contact surface in the current study is the surface pertaining to the cylindrical matrix (epoxy) and the target surface is the surface pertaining to steel fibre. Confusion is to be avoided regarding the deformability of both bodies, indeed they all deform but differently. The matrix deforms elastically whereas the fibre deforms plastically.

Two contact regions were defined: the interfacial contact between steel fibre and epoxy matrix; and the contact between the circumference of the fibre's tip with the tip of the epoxy matrix tunnel (see Figure 5-6). The former is a frictional contact surface to surface whereas the latter is a frictionless contact node to surface. This contact was introduced in order to prevent residual interpenetration of the fibre's end into the resin without introducing tangential stresses. The two contacting parts are free to separate (slide) without resistance.
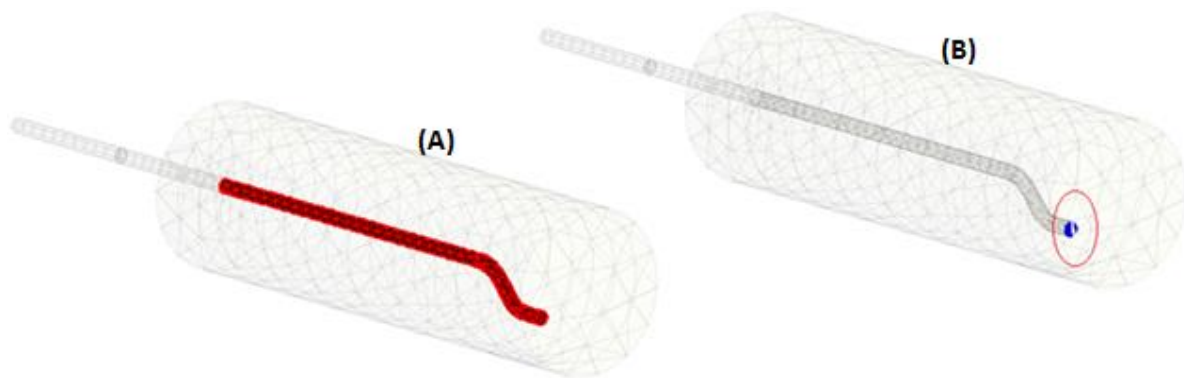
Figure 5-6. Contact definition: (A)-Frictional contact surface-to-surface (Interfacial contact fibre-Epoxy).(B)-Frictionless contact node-to-surface (Interfacial contact fibre's end circumference-epoxy matrix's).

Before any attempt to solve the problem, particular attention was paid to the initial contact status, that is, checking whether the two parts are touching, (Imaoka, 2009). ANSYS Mechanical has adequate tools which allow checking initial contact information including initial penetrations and gaps. A rule of thumb is that if after contact analysis it is found that there are too many gaps, this implies that the two parts are not truly touching one another (there is no contact). But if interpenetration of the parts is observed then contact between

the two parts is guaranteed. The key strength of the initial contact checking information is that any flaw regarding to contact can be repaired before attempting to commence the setup of the simulation. Table 5-4 illustrates the result of initial information of the contact between fibre and epoxy.

Table 5-4. Contact initial information.

Contact name	Contact side	Type	Status	Number contacting	Penetration (mm)	Gap (mm)	Geometric penetration (mm)	Geometric gap (mm)	Resulting pinball (mm)
Frictional	Contact	Frictional	Closed	360	9.9e-15	0	1.2e-2	4.5e-16	0.331
Frictionless	Contact	frictionless	Closed	12	0	0	4.9e-16	3.0e-16	0.3464

Contact initial information has revealed that the penetrations and gaps for both defined contacts are small as compared to the resulting pinball. There is almost no penetration, only insignificant gaps are observed at the bends. In general the status of the contact is closed with a sliding behaviour (as shown in Figure 5-7). For more information on the pinball region, see Appendix B.
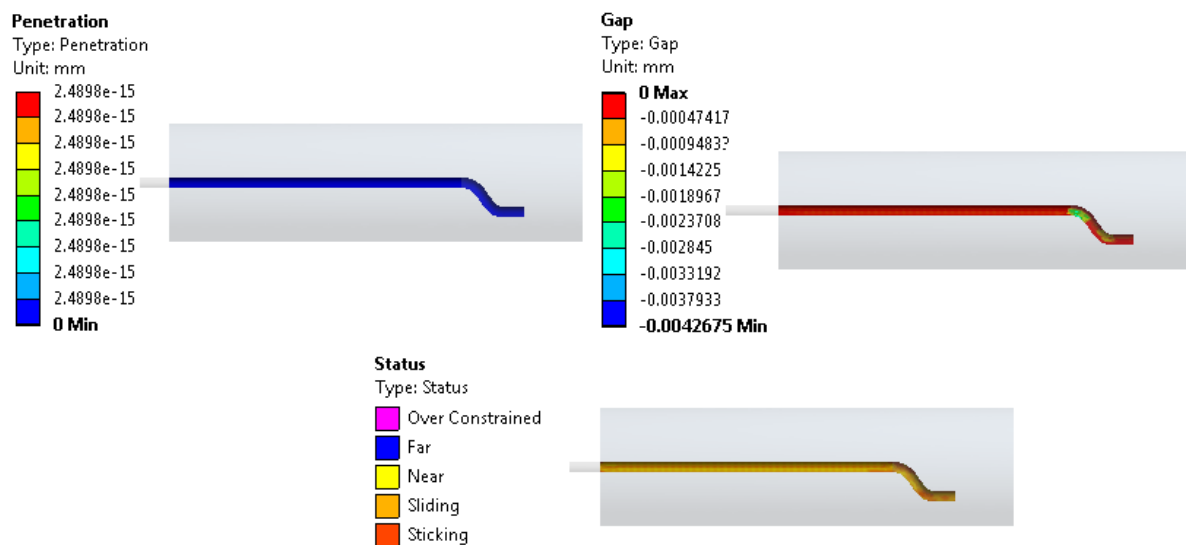
Figure 5-7. Summary of the contact analysis showing interpenetration, gap and overall status of the contact.

5.2.5. Boundary conditions and loading

Successful finite element modelling depends on correctly applying boundary conditions, requiring a good understanding of the physical problem. In the experimental setup, the epoxy matrix was attached to the fixed table of the tensile testing machine via the half dog

bone gripping device. The fibre was firmly held at its free end in a grip mounted to the adjustable crosshead. The pull-out test consisted of pulling the free end of the fibre upwards while the epoxy matrix remained fixed. Numerically, therefore, the outer surface of the epoxy cylinder was defined as a fixed support (that is, constrained in the X, Y and Z axes). The fibre was active in the X-direction but constrained in the Y, and Z-directions. A prescribed displacement was applied in the X-direction to the tip of the fibre. These constraints are illustrated in Figure 5-8.
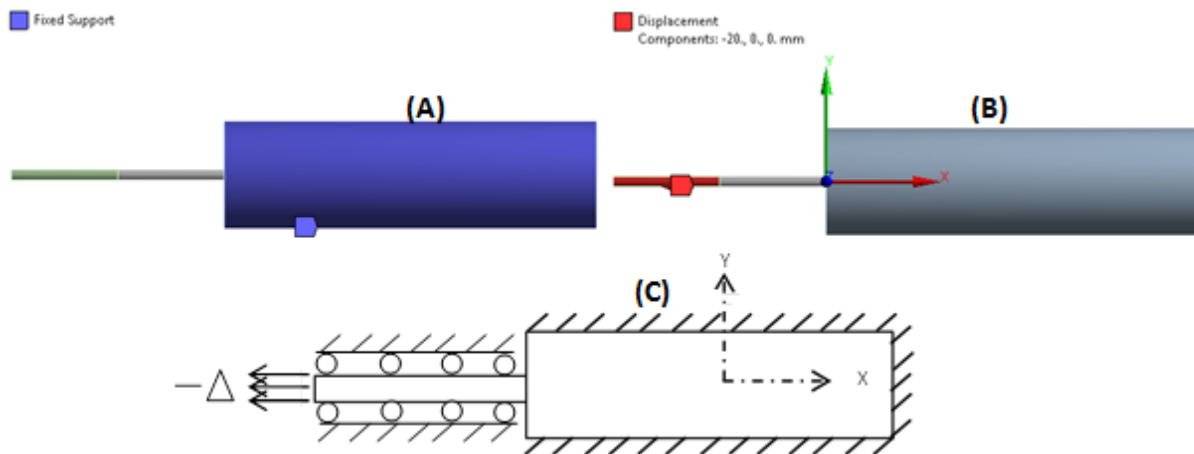
Figure 5-8. Boundary conditions and loading-Finite element model: (A)-Fixed support (epoxy matrix). (B)-Fibre constrained in Y and Z directions, active in the X direction. (C)-Schematic of the pull-out showing constraints.

5.2.6. Solution

The final step in the simulation is to solve the nonlinear equations. The choice of the solver is governed by the requirements of the nonlinear contact algorithm, which is elaborated here.

Contact forces are transferred between the two contacting bodies and interpenetration of one body to the other is not permitted (Imaoka, 2001). In order to satisfy this requirement, one or both bodies must undergo some deformation. In the current study, penetration of the fibre into the matrix is prevented by inserting virtual springs between the two contacting boundaries (see Figure 5-9). Internal forces, dependent on deformation, are thus transferred. Note that the matrix is deforming elastically according to the material definitions.
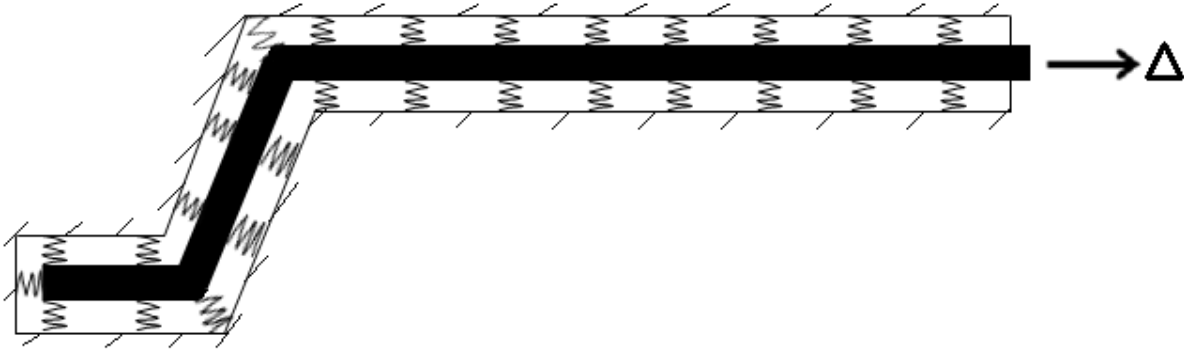
Figure 5-9. Fibre in the epoxy duct showing interfacial virtual contact springs.

Recall that the finite element equations which must be solved are of the form:

$$[K]\{U\} = \{F\} \qquad (5\text{-}4)$$

where $[K]$ is stiffness matrix of the structure, $\{U\}$ is the finite displacement of the structure, and $\{F\}$ are the external forces applied to the structure.

Equation (5-4) includes contact effects which can be written:

$$k_c \Delta x_p = \Delta F_c \qquad (5\text{-}5)$$

where k_c is the contact stiffness, Δx_p is the penetration or gap (i.e. the distance separating two nodes of contacting bodies) and ΔF_c is the contact force. Notice that the spring stiffness k_c must be varied in order to enforce contact compatibility (interpenetration prevention), i.e., as $k_c \rightarrow \infty$, $\Delta x_p \rightarrow 0$. The control of k_c varies according to whether a pure penalty or augmented Lagrange formulation is chosen. Both contact methods are penalty-based formulations, the main difference is that the augmented Lagrange formulation is less sensitive to the magnitude of the contact stiffness k_c due to the fact that this method augments the contact force by an extra factor λ as seen in equation (5-6) (ANSYS-Inc., 2010).

$$k_c \Delta x_p + \lambda = \Delta F_c \qquad (5\text{-}6)$$

Contact problems are characterised by a matrix stiffness which is a function of the displacement, $[K] = [K(\{u\})]$. Additionally, as k_c contributes to the total stiffness matrix $[K]$, varying k_c can result in an ill-conditioned matrix. The solver selected in the current study is the sparse direct solver due to its ability to solve ill-conditioned matrices, and due to its low memory and disc space requirement. The contact formulation selected is the augmented Lagrange method since it guarantees better results from an interpenetration point of view.

The solving method selected is Newton-Raphson formulation due to its capability of being able to auto-control the penetration during analysis. Newton–Raphson method uses an iterative series with linear approximations with correction in order to predict nonlinear responses. The nonlinear equation (5-5) can be rewritten as follows:

$$\left[K_i^T\right]\{\Delta U_i\} = \{F^a\} - \{F_i^{nr}\} \tag{5-7}$$

Where $\left[K_i^T\right]$ is the tangent matrix (Jacobian) at iteration "i";

$\{F^a\}$ and $\{F_i^{nr}\}$ are respectively the applied loads (external forces) and the restoring loads (internal loads);

$\{F^a\} - \{F_i^{nr}\} = \{R\}$ constitutes the residual or the out of balance loads;

$\{\Delta U_i\}$ incremental displacement at iteration "i".

The principle can be understood by considering a simple 1D example, illustrated in Figure 5-10.

The software proceeds as follows (Metrisin, 2008):

1.   An arbitrary value of $\{\Delta U_i\}$ is initially guessed by the software, thus leading to evaluation of the corresponding internal force $\{F_i^{nr}\}$;

2.   As external forces are known, thus the Jacobian $\left[K_i^T\right]$ is computed then the displacement correction $\{\Delta U_i\}$ is computed by solving the linear system for the corresponding iteration $\left[K_i^T\right]\{\Delta U_i\} = \{R\}$;

3.   Next the residual out of balance force, $\{R\}$, is compared to the convergence criterion which states that $\{R\} < 0.1\ \%\{F^a\}$. If this condition is satisfied, then the value of $\{\Delta U_i\}$ was a good guess and thus the solution has converged.
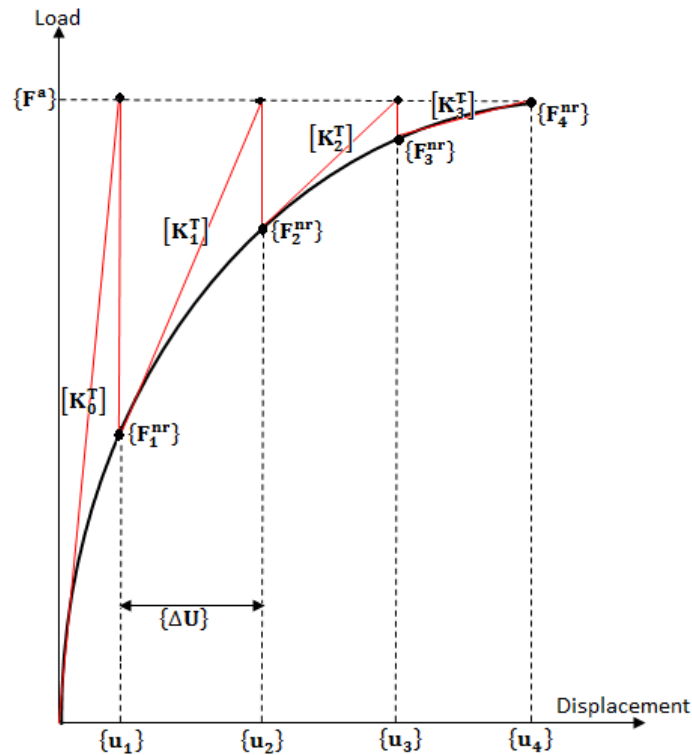
Figure 5-10. Principle of Newton-Raphson scheme-One increment of load corresponding to four equilibrium iterations. (Bothmann, 2004).

4.　　But if the criterion is violated, then another iteration will commence leading to an adjustment of $\{\Delta U_i\}$ to its new value. The residual out of balance force is recalculated and compared again to the convergence criterion. This process carries on until convergence is reached ($\{R\} < 0.1\ \%\{F^a\}$).

In the current study the simulation was conducted in two steps divided in substeps. Initially 10 substeps were defined for step one and 200 substeps for step 2. One substep corresponds to one increment of load as shown in Figure 5-10.

No load was defined for step one, only contact problems were initially treated and then solved (initial penetrations and gaps). Step two was characterized by a prescribed displacement of the fibre, 20 mm in the X-direction (Figure 5-8(C)).

5.2.7. Initial results

A sample curve from this initial numerical model is shown in Figure 5-11. It is clear that the numerical pull-out curve does not correlate with the experimental observations. The numerical pull-out process appears to occur more rapidly and results in a narrower curve than the experimental response. The initial numerical model was overly simplistic, and needed to be improved. Sensitivity studies from this initial model are included in Appendix C for completeness.
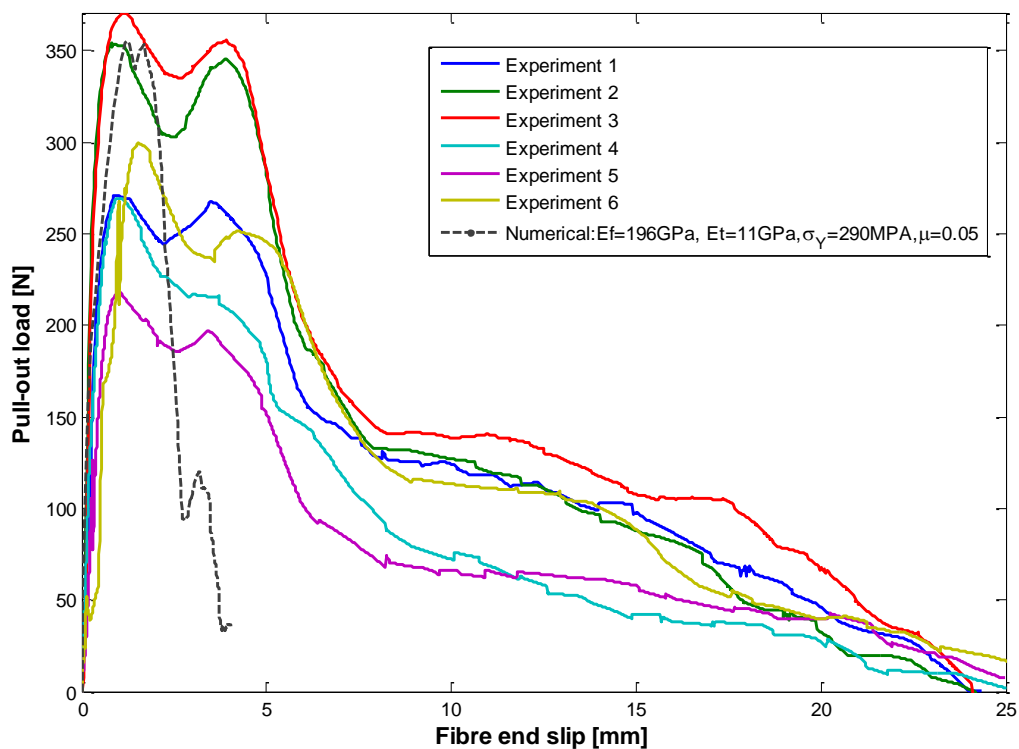
Figure 5-11. Comparison of the initial numerical response to experimental curves.

5.3. Improved model

The initial model, (discussed in Section 5.2.) was missing some interesting physics. in order to improve the correlation between the numerical model and observed experimental behaviour, the following modifications were made:

- Addition of a linear spring in the model to characterise the compliance of the tensile testing machine;
- Material model refinement: improvement of the steel fibre material properties (yield stress and tangent modulus);
- Identification of two distinct regions of the fibre, undeformed parts and work-hardened ones.

Based on the above mentioned improvements the material properties (as seen in Table 5-2) obtained from the tensile test of the steel wire has changed. Two yield stresses have been introduced; the virgin yield stress (σ_{YV}) is refereeing to the undeformed parts of the fibre and the plasticised yield stress (σ_{YPl}) which refers to the bends. In these simulations, the tangent modulus was not guessed (estimated) as previously, but was calculated from the graph (stress versus plastic strains) obtained from a bending test of steel wire.

5.3.1. Addition of a linear spring in the model

The fibre end displacements reported in the experimental curves include the machine compliance (Tsai and Kim, 1996) since measurements were taken from the crosshead of the testing machine. Given that these effects have to be taken into account, the compliance of the machine is simulated by the addition of a linear deformable spring of length $L_{spring}=$ 10 mm. This spring is rigidly attached to the free tip of the fibre on one hand, and held rigid to another body on which a prescribed displacement (Δ) is applied, as seen in Figure 5-12. The stiffness of the spring will be evaluated through sensitivity studies of the model.
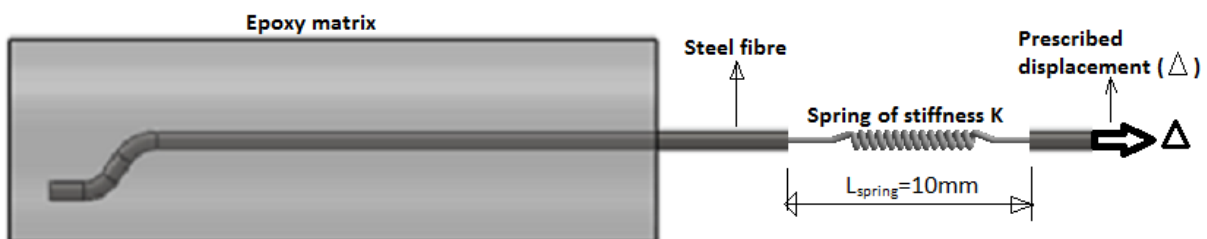
Figure 5-12. Model updated by the addition of a linear deformable spring.

5.3.2. Material model refinement

As noted in Section 3.2.4., the tensile tests conducted on the steel fibre showed very low levels of plastic deformation. This was in contrast to microscopic evidence of ductility, see Section 3.2.5., and pull-out tests (see Chapter 4), requiring substantial plastic deformation. This suggested that the tensile test might not be the best way to characterise such fibres.

Kok (2013) conducted bending tests on the steel wire. Making use of inverse analysis, he characterised the stress-strain relationship for bending up to 50 % plastic strain. The material response obtained from these tests is shown schematically in Figure 5-13.
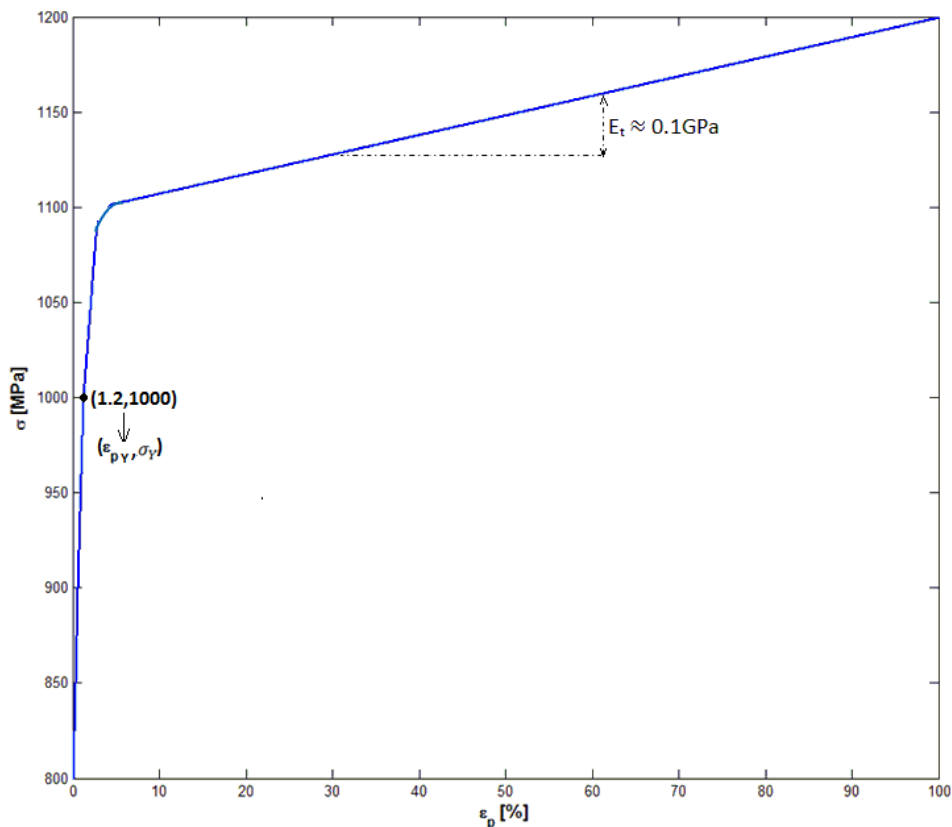
Figure 5-13. Prototype of the stress-strain curve obtained in the bending test of steel wire (Kok, 2013).

Since the material demonstrates very low work hardening, the reason for the anomaly previously discussed is clear - in the tensile test, necking happens very rapidly, making it impossible to observe the plastic deformation. Results obtained for the yield stress (σ_Y) and tangent modulus (Et) are roughly $1\,\mathrm{GPa}$ and $0.1\,\mathrm{GPa}$, respectively. These values were chosen as starting points for simulation, and will be investigated through sensitivity studies.

5.3.3. Two different yield stresses defined for steel fibre

It is noted that the forming of the fibre has involved substantial plastic deformation of the virgin material in order to create two anchorages (bends). The fibre has been work-hardened in the vicinity of these two bends, resulting in a higher yield stress in these regions than in the straight (undeformed) parts of the fibre as indicated schematically in Figure 5-14. Following this reasoning, two yield stresses have been conferred on the steel fibre; one referring to undeformed parts and the other to the deformed ones (bends). The former yield stress has been designated the virgin yield stress (σ_{YV}) and the latter the plasticised yield stress (σ_{YPl}), as illustrated in Figure 6-3.
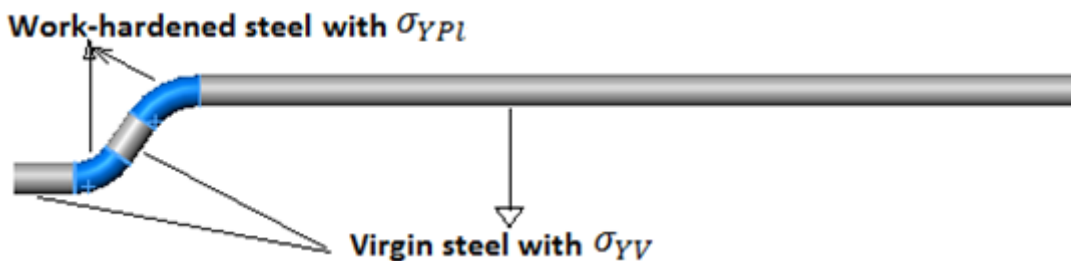
Figure 5-14. New material definition for work-hardened regions of steel fibre.

The virgin yield stress (σ_{YV}) is equivalent to the one obtained from bending test of steel wire, that is $\sigma_{YV} = \sigma_Y$. It should be noted that σ_{YPl} was not calculated in the current study, but was estimated based on the fact that as the two bends have been strengthened by plastic deformation, therefore its yield point can only be higher than the one of the virgin material, this is expressed by the following inequality, (and shown in Figure 5-14):

$$\sigma_{YPl} > \sigma_{YV} \tag{5-8}$$
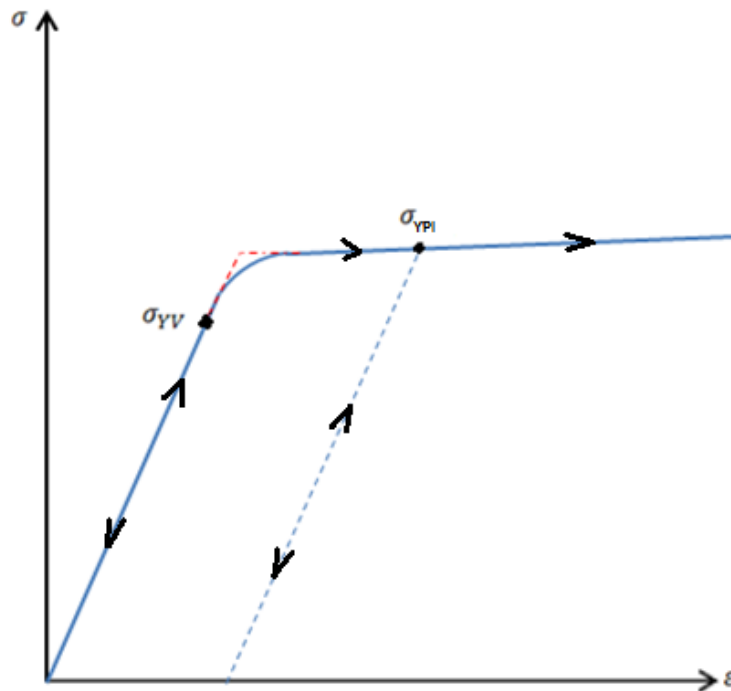
Figure 5-15. Schematic stress-strain curve showing the virgin and plasticised yield stresses with σ$_{YPl}$>σ$_{YV}$.

The value of the work hardened yield stress σ_{YPl} will be investigated through sensitivity studies. Note that we refer to the work hardened yield stress and the plasticised yield stress interchangeably.

5.4. Sensitivity studies

The model has been simulated several times by changing different parameters involved in the model so as to see the impact of each and every one on the pull-out response. During the simulation, only one parameter is being varied, while the remainder were held constant. The parameters involved in these sensitivity studies are:

- Tangent modulus (E_t)
- Fibre elastic modulus (E_f)
- Virgin yield stress (σ_{YPl})
- Work-hardened yield stress (σ_{YV})
- Frictional coefficient (μ)
- Matrix stiffness (E_m)

It is important to notice that in the current study, while conducting the sensitivity study of the model which consists in varying material definitions, some of these changes did not result in a converged solution; further manipulation had to be undertaken in order to force the solution to converge. This was not necessarily done as long as one of the two peaks appeared in the load-displacement curve. In such cases, as it will be observed later, the curve is not shown entirely.

5.4.1. Variation of tangent modulus, E_t

The tangent modulus was varied from the base line value, $0.1\,GPa$, to 1 and $2\,GPa$, as shown in Table 5-5. The other parameters were held constant. Figure 5-16 shows the corresponding curves which interpret the sensitivity of the model to the tangent modulus variation. As the tangent modulus increases, the pull-out load increases as well, but the displacements do not shift. The material definition with $E_t = 2\,GPa$ showed an unconverged solution after the first peak.

Table 5-5. Sensitivity studies: model parameter varying tangent modulus

Simulation number	Steel fibre						Matrix
	Tangent modulus	Elastic modulus	Virgin yield stress	Plasticized yield stress	Coefficient of friction	Spring stiffness	Elastic modulus
	E_T [GPa]	E_f [GPa]	σ_{YV} [GPa]	σ_{YPls} [GPa]	μ	K [kN/mm]	E_m [GPa]
1	**0.1**						
2	1	196	1	1.2	0.05	1	3
3	2						
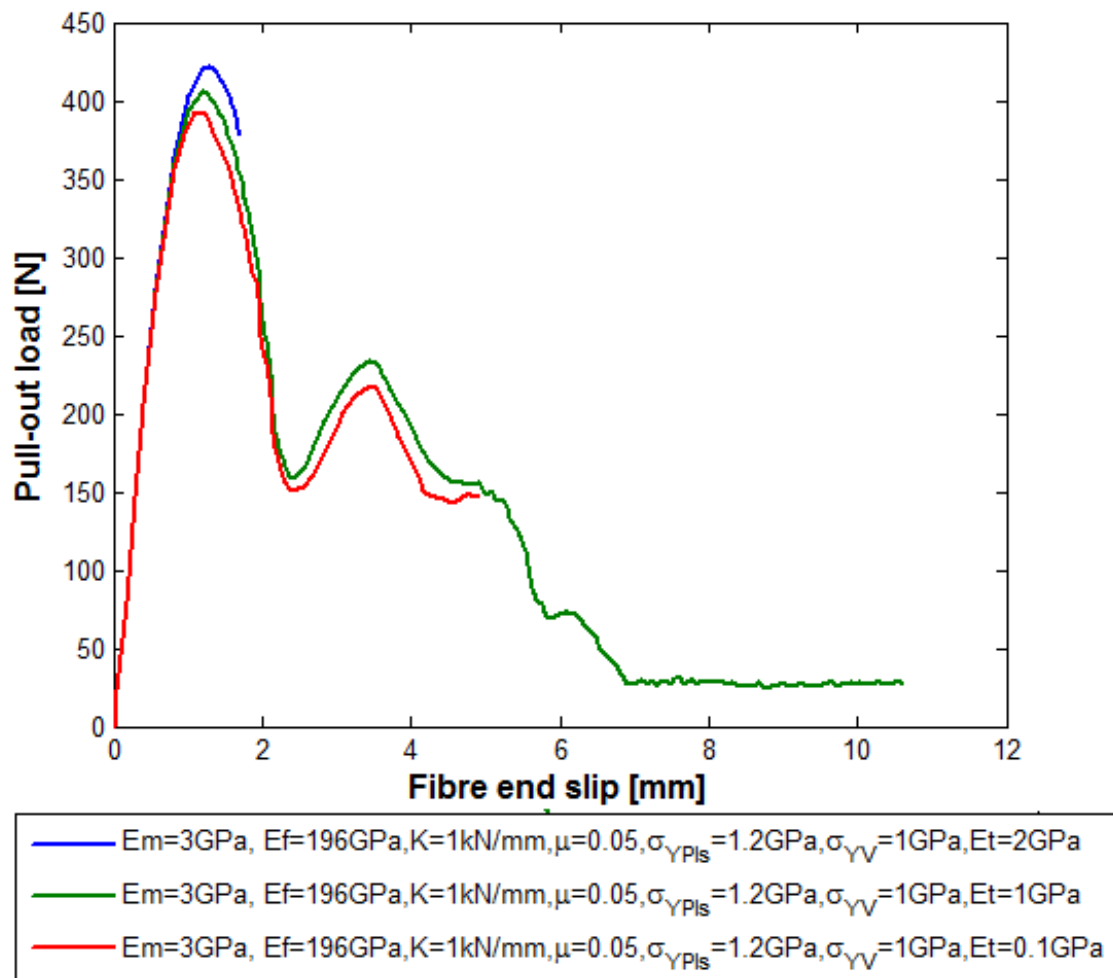
Figure 5-16. Sensitivity studies: Impact of the tangent modulus (E_t).

5.4.2. Variation of the fibre's elastic modulus, E_f

The fibre's elastic modulus was varied from the base line value 196 GPa to 182 and 210 GPa, all the rest were held constant. The material definition for this simulation is presented in Table 5-6. Results shown in form of pull-out load versus displacement (see Figure 5-16) reveal that changes in the fibre's elastic modulus do not influence the pull-out behaviour. However, they do have an impact on the convergence of the solution. For E_f= 210 GPa the solution did not completely converge.

Table 5-6.Sensitivity studies: model parameter varying the fibre's elastic modulus

Simulation number	Steel fibre						Matrix
	Tangent modulus	Elastic modulus	Virgin yield stress	Plasticized yield stress	Coefficient of friction	Spring stiffness	Elastic modulus
	E_T [GPa]	E_f [GPa]	σ_{YV} [GPa]	σ_{YPls} [GPa]	μ	K [kN/mm]	E_m [GPa]
1		182					
2	1	**196**	1	1.2	0.05	1	3
3		210					

Figure 5-17. Sensitivity studies: Impact of the fibre's elastic modulus (E_f).
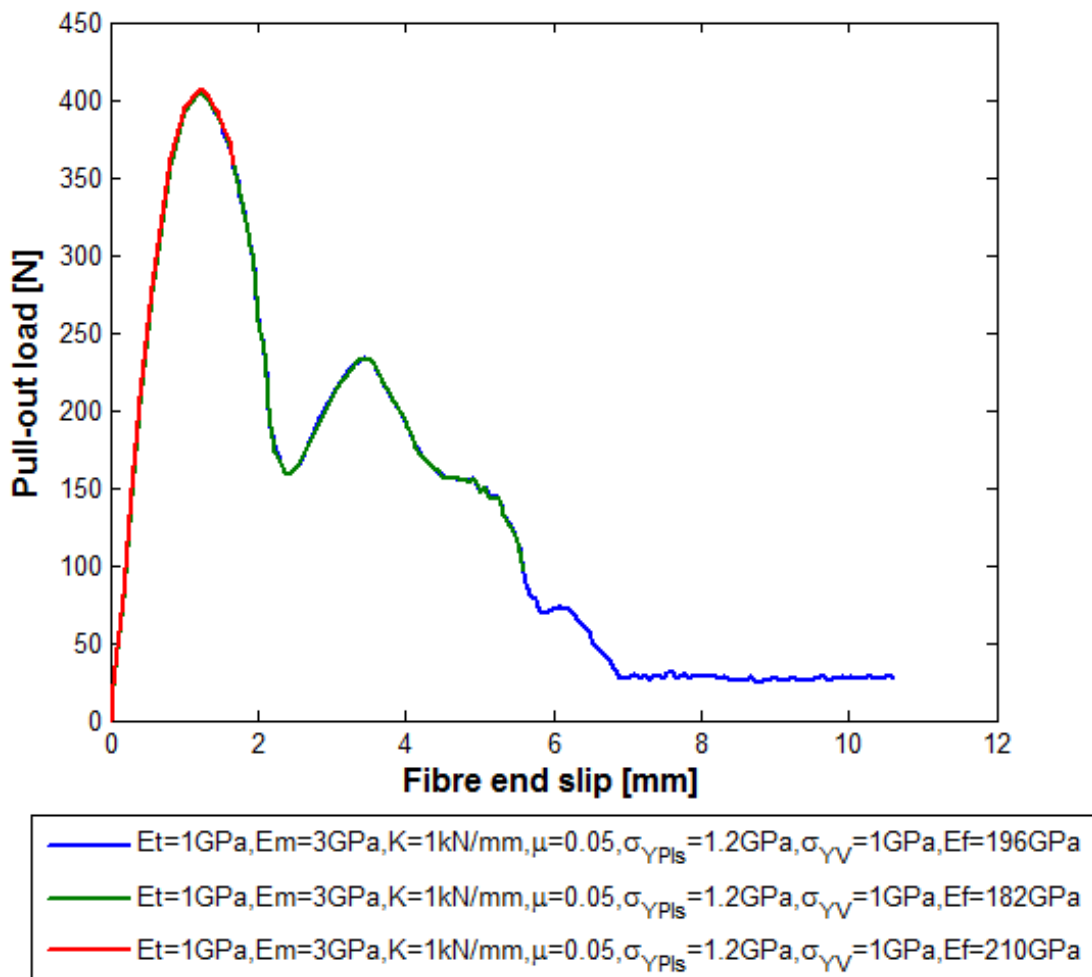
5.4.3. Variation of the plasticised yield stress, σ_{YPl}

The plasticised yield stress (which refers to the yield stress of the two bends) was changed from the base line value 1.2 GPa to 1.5 and 1.8 GPa. The model parameters are presented

in Table 5-7. The numerical pull-out curves, as seen in Figure 5-18, show that variations of the plasticised yield stress have an impact on the pull-out behaviour. As the plasticised yield stress increases, the peak pull-out load increases also. The ratio between σ_{YV} and σ_{YPl} changes the character of the curve, with increasing contrast between the two introducing more peaks.

Table 5-7. Sensitivity studies: model parameter varying the plasticised yield stress

Simulation number	Steel fibre						Matrix
	Tangent modulus	Elastic modulus	Virgin yield stress	Plasticized yield stress	Coefficient of friction	Spring stiffness	Elastic modulus
	E_T [GPa]	E_f [GPa]	σ_{YV} [GPa]	σ_{YPls} [GPa]	μ	K [kN/mm]	E_m [GPa]
1				1.2			
2	1	196	1	1.5	0.05	1	3
3				1.8			
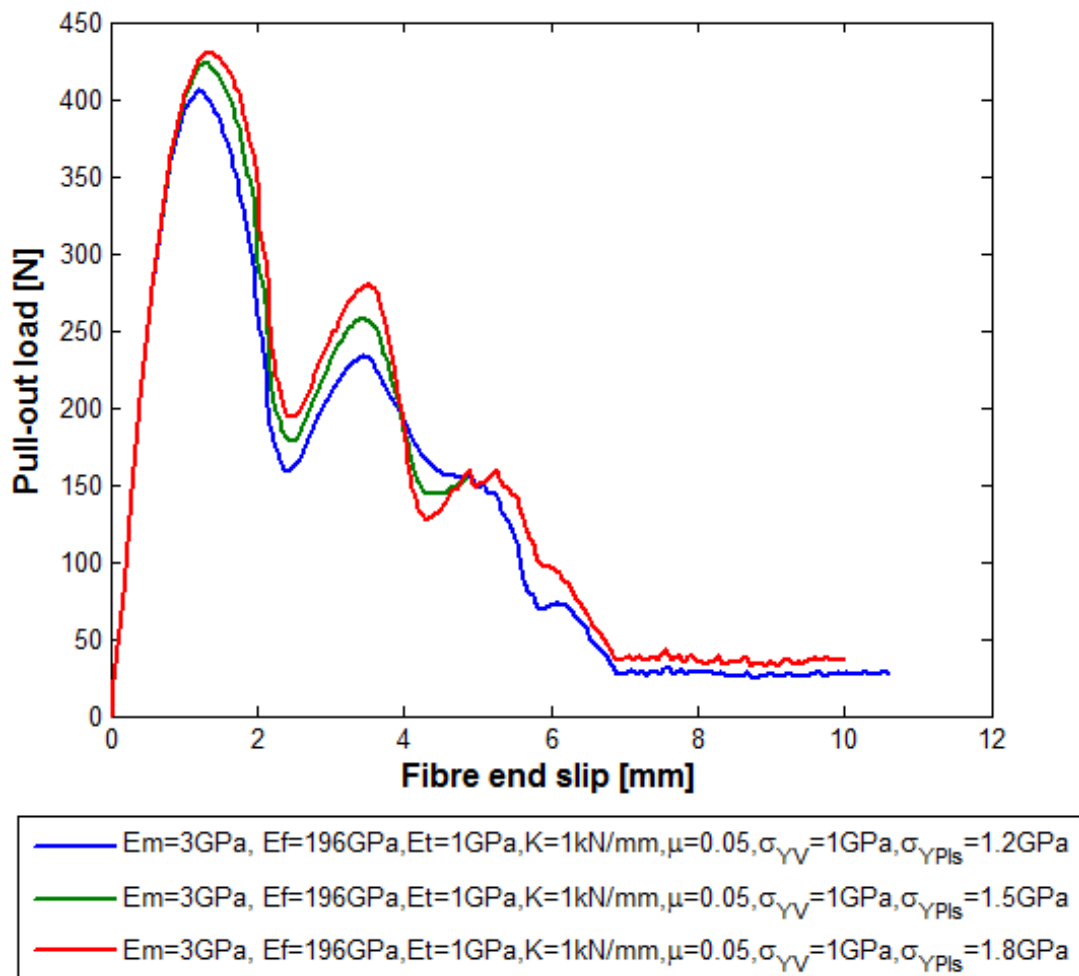
Figure 5-18. Sensitivity studies: Impact of the plasticised yield stress (σ_{YPls}).

5.4.4. Variation of the virgin yield stress, σ_{YV}

The virgin yield stress, which refers to the yield point of the original material of the fibre before any alteration of the material, was changed from the base line value $1\,\text{GPa}$ to 0.8 and $0.6\,\text{GPa}$ as seen in Table 5-8. Results presented in Figure 5-19 have shown that the numerical model is sensitive to the virgin yield stress variations. Increase the virgin yield stress results in an increased maximum pull-out force. Note that when virgin yield stress is decreased significantly, the pull-out curve presents three pronounced peaks instead of two. This may be a consequence of the ratio between σ_{YV} and σ_{YPl} rather than simply an effect of σ_{YV}.

Table 5-8. Sensitivity studies: model parameter varying the virgin yield stress

Simulation number	Steel fibre						Matrix
	Tangent modulus	Elastic modulus	Virgin yield stress	Plasticized yield stress	Coefficient of friction	Spring stiffness	Elastic modulus
	E_T [GPa]	E_f [GPa]	σ_{YV} [GPa]	σ_{YPls} [GPa]	μ	K [kN/mm]	E_m [GPa]
1			1				
2	1	196	0.8	1.2	0.05	1	3
3			0.6				
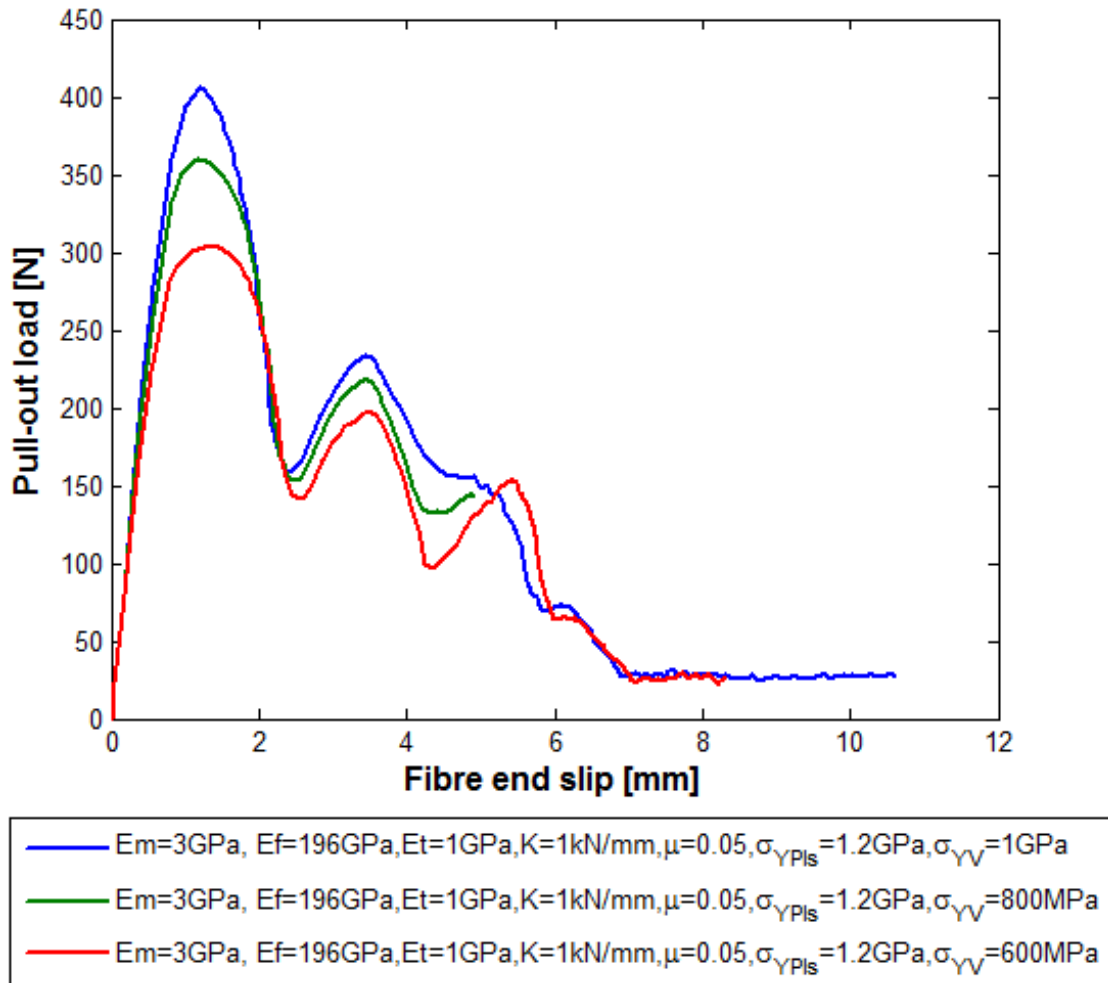
Figure 5-19. Sensitivity studies: Impact of the virgin yield stress (σ_{YV}).

5.4.5. Variation of the static coefficient of friction, μ

The static coefficient of friction was changed from the base line 0.05 to 0.075 and 0.1, while the other parameters are held constant (See Table 5-9). The plots of these material definitions, as seen in Figure 5-20, indicate that the model is sensitive to the static frictional coefficient. The peak load increases as the static coefficient of friction increases. This is in agreement with the results of Georgiadi-Stefanidi *et al.* (2010).

Table 5-9. New sensitivity studies: model parameter varying the static frictional coefficient.

Simulation number	Steel fibre						Matrix
	Tangent modulus	Elastic modulus	Virgin yield stress	Plasticized yield stress	Coefficient of friction	Spring stiffness	Elastic modulus
	E_T [GPa]	E_f [GPa]	σ_{YV} [GPa]	σ_{YPls} [GPa]	μ	K [kN/mm]	E_m [GPa]
1					**0.05**		
2	1	196	1	1.2	0.075	1	3
3					0.1		
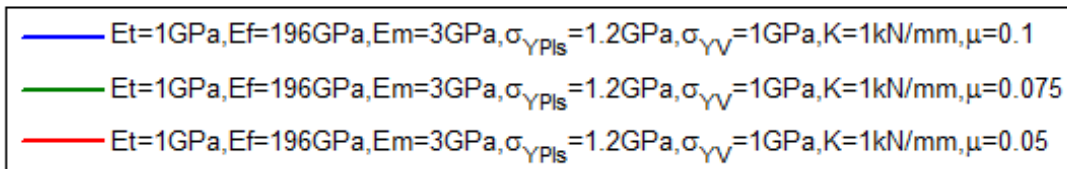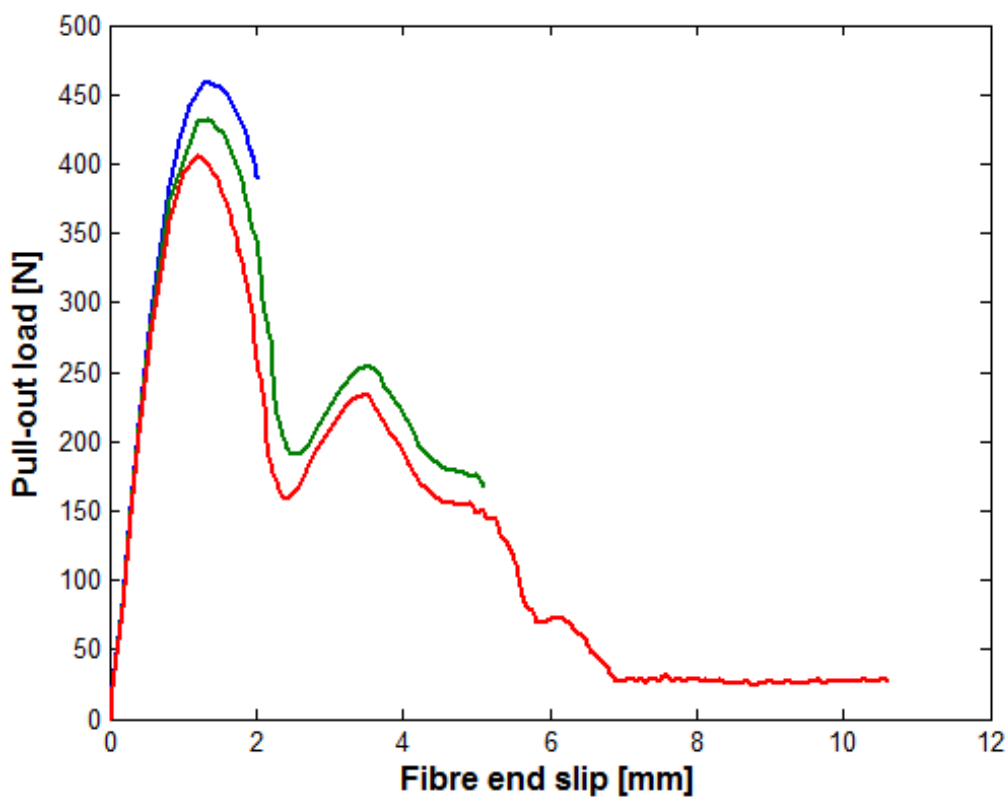
Figure 5-20. Sensitivity studies: Impact of the static frictional coefficient (μ).

5.4.6. Variation of the spring stiffness, K

The spring stiffness was changed from a base line value 1kN /mm to 0.8 and 0.6 kN/mm as seen in Table 5-10. As can be seen in Figure 5-21, the model is sensitive to the spring stiffness. Contrary to previous sensitivity studies in which changes of parameters have influenced the peak pull-out loads, the change of spring stiffness in this case has only influenced the displacements. The less the stiffness the more the curve spreads on the right.

Table 5-10. Sensitivity studies: model parameter varying the spring stiffness

Simulation number	Steel fibre						Matrix
	Tangent modulus	Elastic modulus	Virgin yield stress	Plasticized yield stress	Coefficient of friction	Spring stiffness	Elastic modulus
	E_T [GPa]	E_f [GPa]	σ_{YV} [GPa]	σ_{YPls} [GPa]	μ	K [kN/mm]	E_m [GPa]
1						1	
2	1	196	1	1.2	0.05	0.8	3
3						0.6	
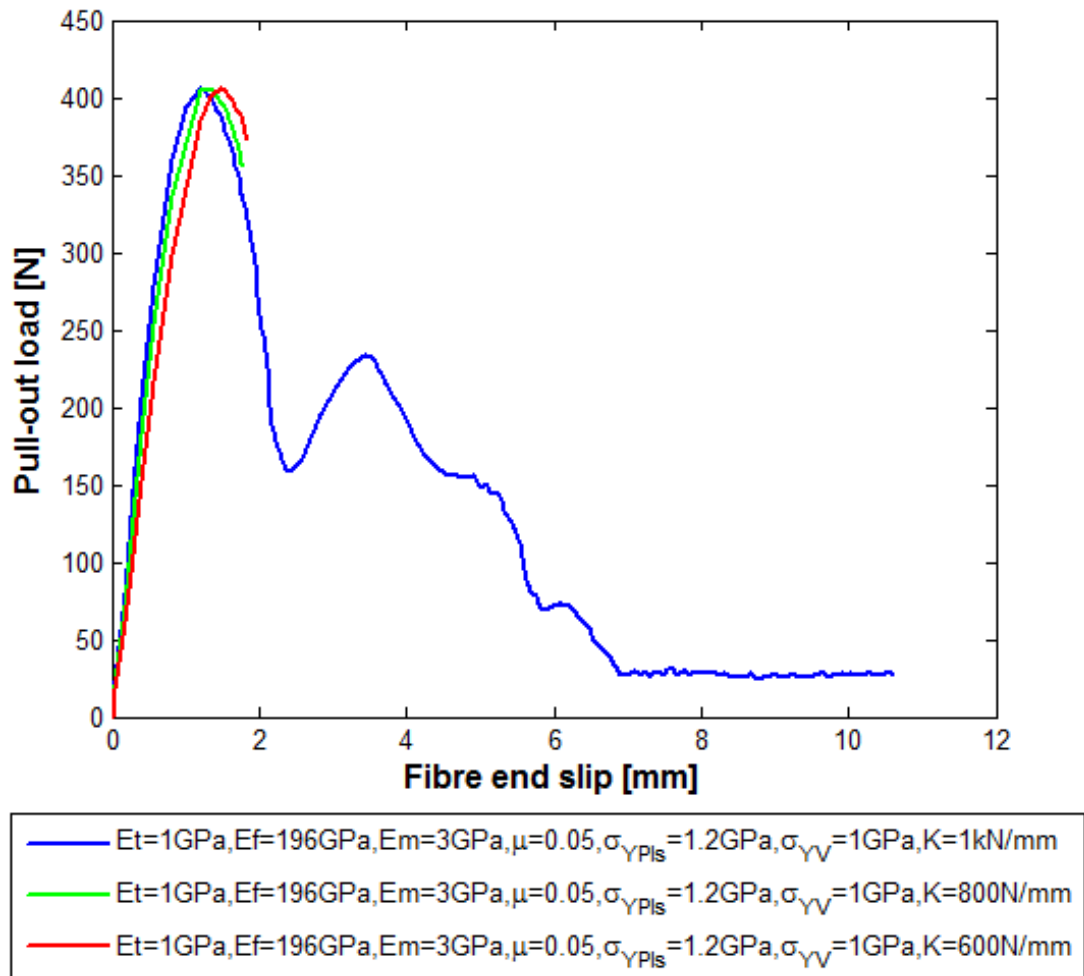
Figure 5-21. Sensitivity studies: Impact of the spring stiffness (K).

5.5.1. Variation of the matrix stiffness, E_m

The last step in the new sensitivity studies is the variation of the matrix stiffness which has been varied from the base line of 3 GPa to 1 and 5 GPa. The material definitions are provided in Table 5-11. These results are presented in form of curves pull-out load versus fibre's end displacement. As can be seen in these curves, see Figure 5-22, the matrix stiffness plays also a very important role in the pull-out process. The stiffer the matrix is, the greater resistance it presents to pull-out will, thus requiring a higher pull-out load.

Table 5-11. Sensitivity studies: model parameter varying the matrix stiffness.

Simulation number	Steel fibre						Matrix
	Tangent modulus	Elastic modulus	Virgin yield stress	Plasticized yield stress	Coefficient of friction	Spring stiffness	Elastic modulus
	E_T [GPa]	E_f [GPa]	σ_{YV} [GPa]	σ_{YPls} [GPa]	μ	K [kN/mm]	E_m [GPa]
1							1
2	1	196	1	1.2	0.05	1	3
3							5

Figure 5-22. Sensitivity studies: Impact of the matrix stiffness (E_m).

5.5.   Numerical investigation of pull-out mechanism

One of the important contributions of the numerical model as opposed to the experimental results is that it is possible to obtain additional information such as stress and strain distributions in both the fibre and the epoxy tunnel, leading to an enhanced understanding of the underlying mechanics. This section investigates the physics of the pull-out behaviour of the hooked end steel fibre from the corresponding matrix. To this end, the fibre positions (while being pulled-out), will be correlated with specific points on the numerical pull-out curve. The material definition of the current simulation is presented in Table 5-12.

Table 5-12. Material definition for the current simulation.

Steel fibre						Matrix
Tangent modulus E_T	Elastic modulus E_f	Virgin yield stress σ_{YV}	Plasticized yield stress σ_{YPls}	Coefficient of friction μ	Spring stiffness K	Elastic modulus E_m
[GPa]	[GPa]	[GPa]	[GPa]	-	[kN/mm]	[GPa]
0.1	196	1	1.2	0.05	1	3

Three points were selected on the numerical pull-out curve, as seen in Figure 5-23; these points represent the following configurations: the first peak (P_{max1}), the first minimum (P_{min1}) and the second peak (P_{max2}).
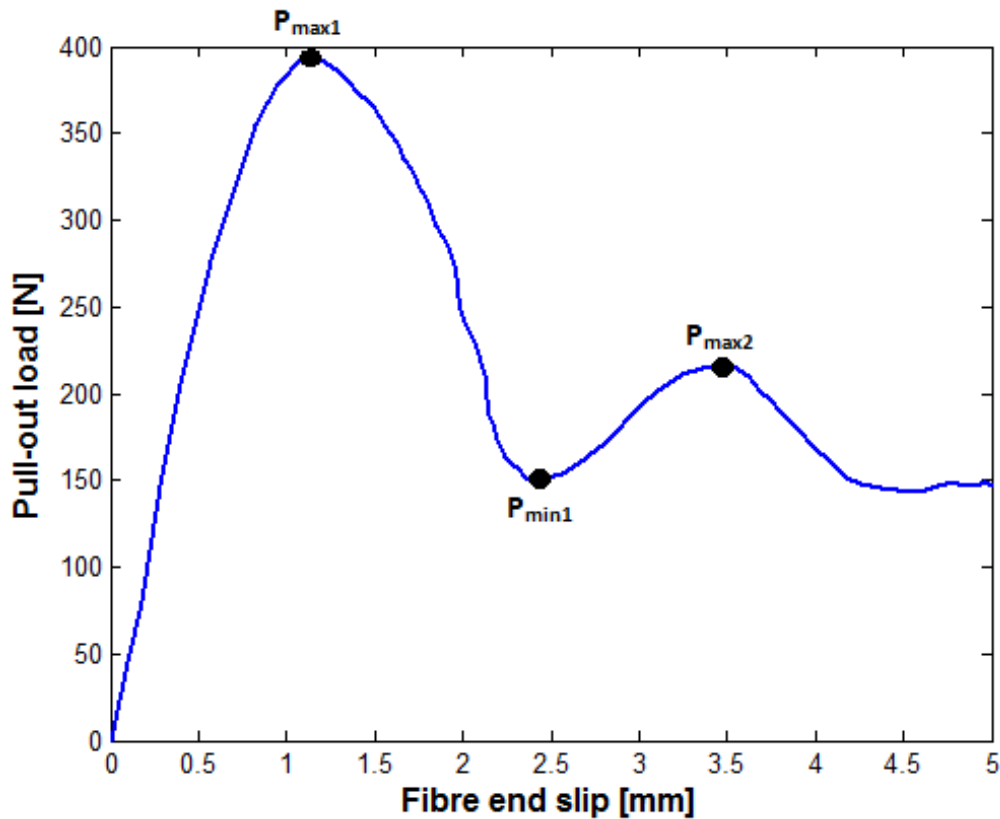
Figure 5-23. Numerical pull-out curve showing selected points for correlations of fibre's positions in the duct of the matrix.

In Figure 5-24, the fibre deformation for the selected points are shown, plotted with contours of equivalent stress (von Mises stress). The position corresponding to the first maximum (P_{max1}) has the highest stress; this is a result of an increase of the force required to simultaneously bend the two work-hardened parts (bends) of the fibre. This stage is accompanied by the penetration of the fibre tip into the duct of the matrix. Figure 5-24(b) shows the position at P_{min1} when the two bends are being straightened, with the second bend engaged in the straight horizontal channel and the first bend engaged in the straight inclined channel. Here, the fibre slips and consequently the force (stress) decreases. It is observed (Figure 5-24(c)) that at the position corresponding to the second peak load (P_{max2}) the stress has slightly increased. This is a consequence of the resistance of the second bend, which has already been deformed while entering the straight inclined channel, to undergoing an inverse bending in order for it to enter the straight horizontal channel.

Notice that interpenetration of the fibre into the matrix is observed, see Figure 5-24, this is normal because the contact model penalises interpenetration but does not prohibit its occurrence.
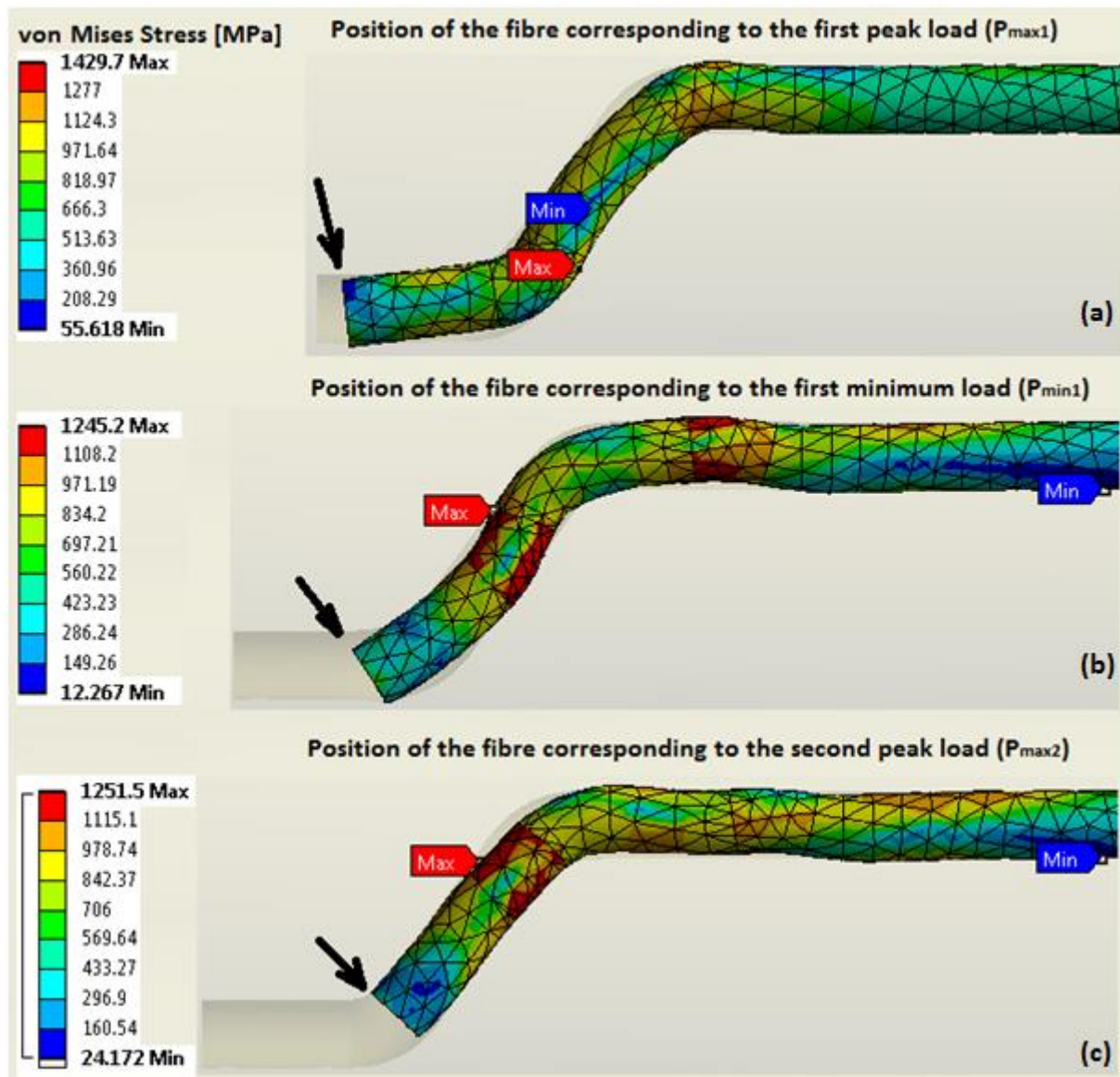
Figure 5-24. Equivalent stress (von Mises) contours plotted on the deformed fibre at (a) P_{max1}, (b) P_{min1}, and (c) P_{max2}.

An overview of the fibre's state of stress and strain is presented in Table 5-13 showing for each selected point the maximum equivalent stress (von Mises stress), the maximum principal stress and the maximum equivalent plastic strain.

Table 5-13. State of stress and strain for different selected points on the numerical curve.

Selected points	Max von-Mises stress	Max principal stress σ_1	Max Shear stress τ_{max}	Max Frictional stress	Max Equivalent plastic strain ε_{1-max}
	[MPa]				[mm/mm]
P_{max1}	1430	1417	787	53	0.19553
P_{min1}	1245	1371	660	49	0.57427
P_{max2}	1252	1680	687	39	0.57546

It should be noticed that these maximum stresses are localised in the structure (fibre), occurring either at an internal or external spot, probably due to interpenetration between the fibre and the matrix or possibly due to a mesh quality problem at that particular zone. Figure 5-25 illustrates for the first configuration (P_{max1}) a closed look at the equivalent stress distribution; as can be seen, the maximum stress occurs on the boundary separating the initially plasticised material from the virgin one. Note that this cut was intentionally introduced into the fibre's geometry in order to vary the material of the fibre as far as the yield stress is concerned (see Section 5.3.3). More information on other cases, maximum principal stress and maximum shear stress, are illustrated in Appendix D.
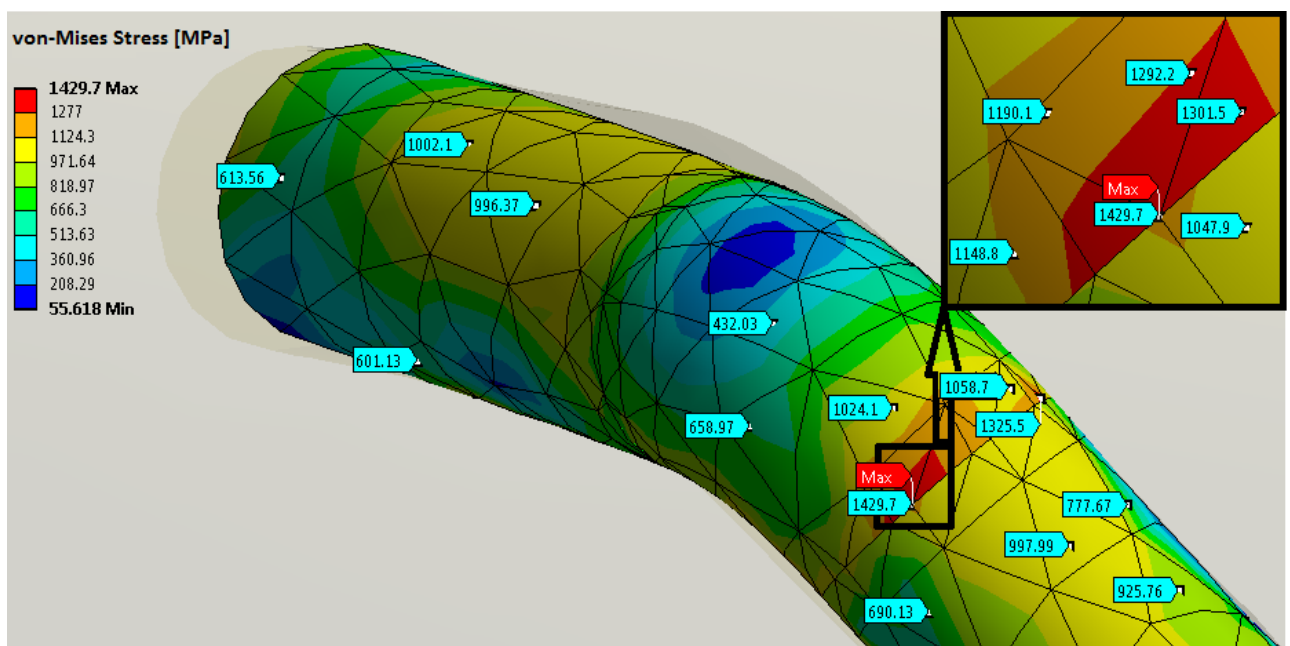
Figure 5-25. Observation of the first bend of the fibre where maximum equivalent stress occurs, at load P$_{max1}$.

5.5.1.   Investigating plasticity of the fibre

The plastic behaviour of the fibre is investigated by studying the equivalent plastic strain experienced by different parts of the fibre. The fibre has been segmented into five parts as seen in Figure 5-26.

1: First straight horizontal part (Tail)   2: First bend   3: Straight inclined part
4: Second bend   5: Second straight horizontal part
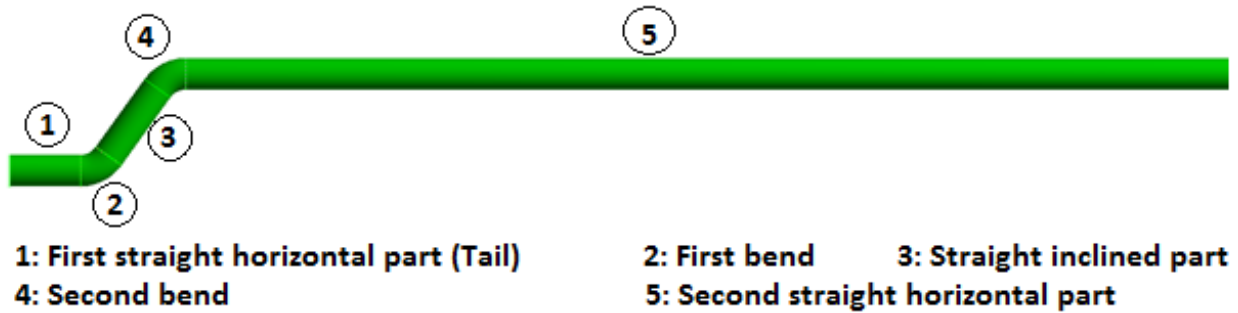
Figure 5-26. Different regions of the fibre for plastic strain studies.

Figure 5-27 shows the maximum equivalent plastic strain distribution, versus the fibre end slip, experienced by the first straight horizontal part of the fibre. Four plateaus are observed in this graph during which the equivalent plastic strain remains constant for some period.

Note that the increment of equivalent plastic strain ($\Delta\bar{\varepsilon}^p$) is strictly positive (Nikishkov and Altluri, 1993).

$$\Delta\bar{\varepsilon}^p \geq 0 \qquad\qquad (5\text{-}8)$$

Thus, the equivalent plastic strain can either increase or remain constant, but is never permitted to decrease. A constant maximum equivalent plastic strain indicates that the material is experiencing elastic loading or unloading.

The tail experiences no plastic deformation up until the fibre has displaced approximately 1mm, after which the plastic deformation of the tail increases while the tail is passing through the first bend of the matrix. Then the plastic strain is stable followed by a slight increase. The most accumulation of plastic deformation of the tail occurred along its passage from the first bend of the matrix to the second one.

Region 2, the first bend of the fibre (see Figure 5-28), experiences progressively increasing plastic strain as the bend is straightened, up until the fibre has displaced approximately 4 mm, then a plateau is observed. The load again increases as the region undergoes reverse bending.

Figure 5-27. Maximum equivalent plastic strain experienced by the tail of the fibre (region 1).
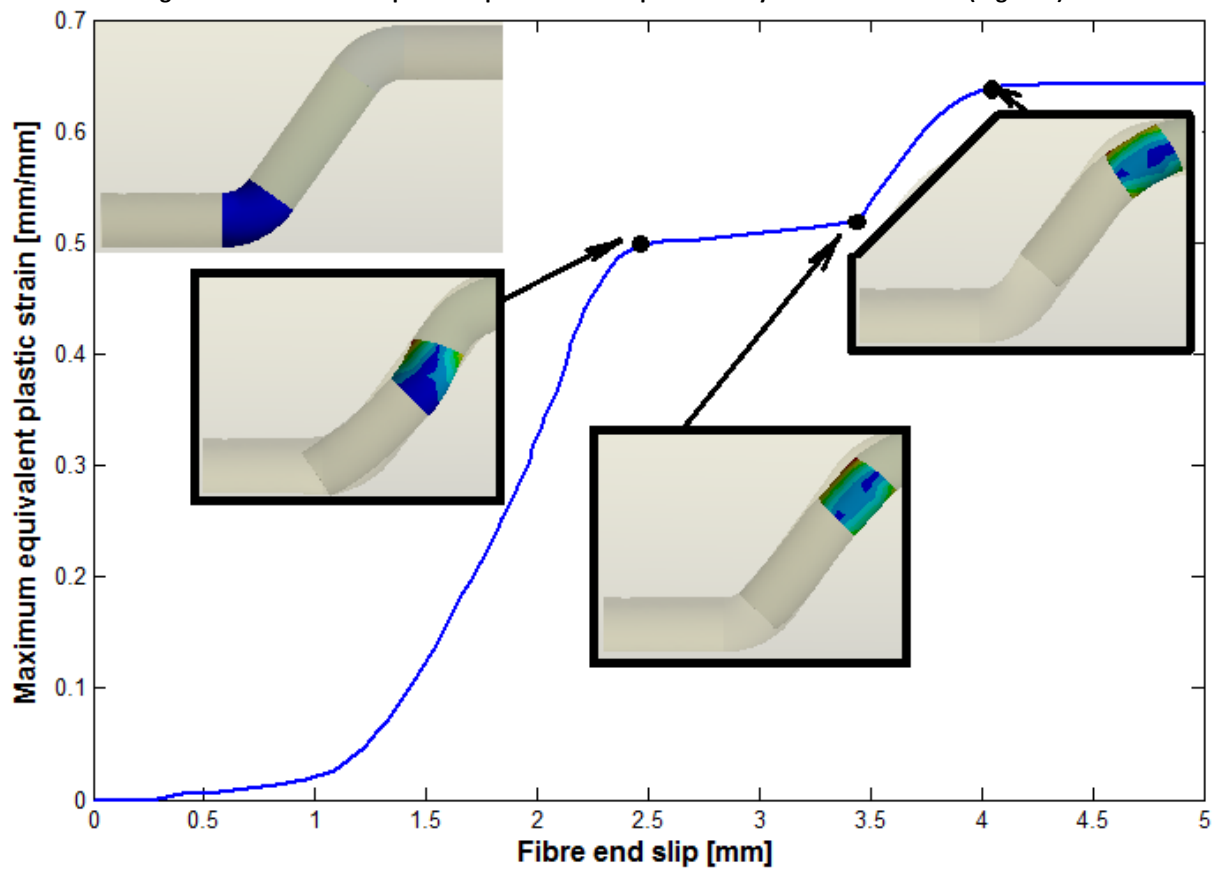
Figure 5-28. Maximum equivalent plastic strain experienced by the first bend of the fibre (region 2).

For the straight inclined part of the fibre, region 3, the plastic behaviour is similar as in previous cases, with plastic strain increasing while the fibre undergoes bending, and then plateauing in the straight region (Figure 5-29). However, it is observed that after the plateau the equivalent plastic strain decreases, which is not theoretically permissible, as discussed previously. This decrease in the equivalent plastic strain could be a result of numerical error. Consider two Gauss points G1 and G2, of an element, located on a stress-strain curve as shown in Figure 5-30(A). These points have become G_1' and G_2' after an interval of time (see Figure 5-30(B)). In the former case G1 is in elastic zone whereas G2 is in the plastic zone. In contrary, G_1' and G_2' are both in the plastic zone. As the maximum value is needed, extrapolation of these points to the surface of the element should be performed and the extrapolated points to the element surface are presented G^* and $G^{*\prime}$. Notice that the former point (G^*) does not define the proper behaviour of the material (because is not on the characteristic curve) and is artificially larger than the latter. This numerical effect could be the reason why the equivalent plastic strain has decreased in this particular case. It appears that the maximum plastic strain occurs in a region with a high gradient of plastic strain from the surface to the interior.
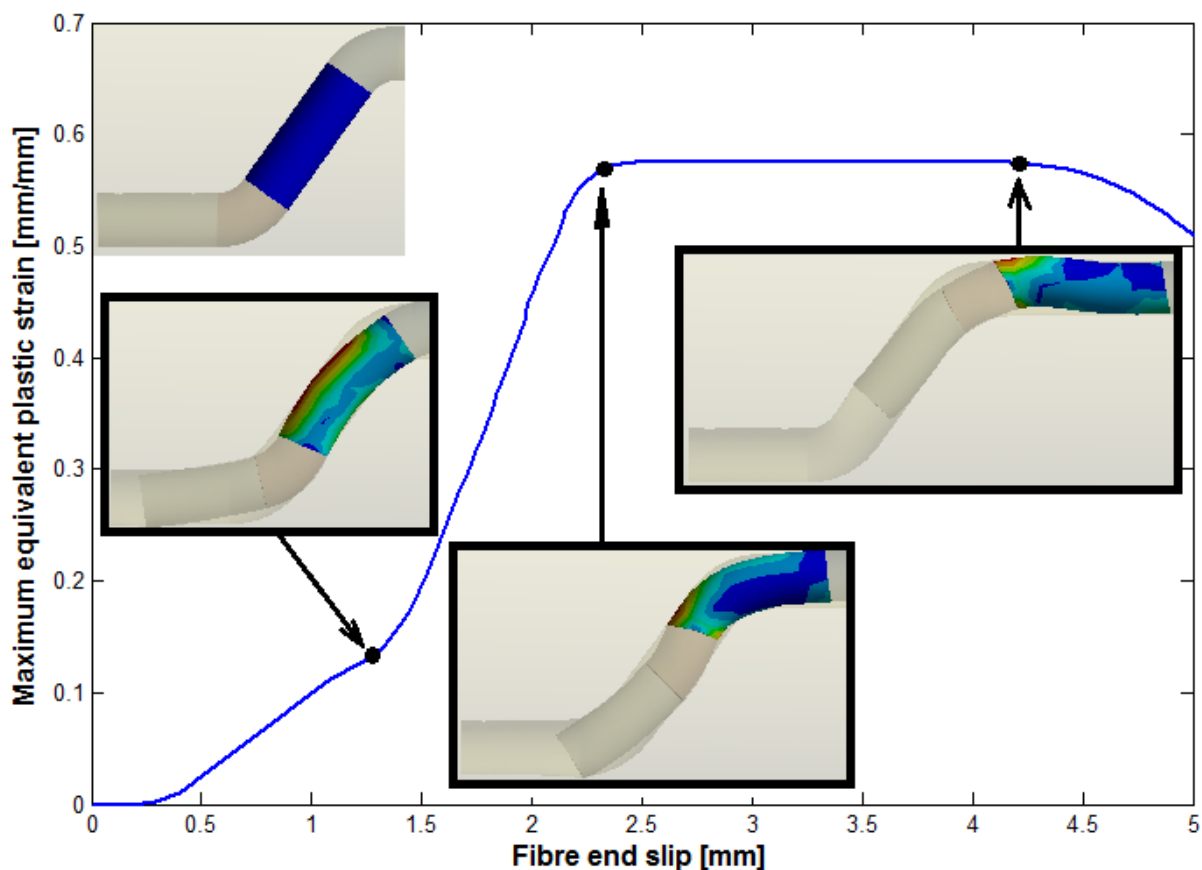
Figure 5-29. Maximum equivalent plastic strain experienced by the straight inclined part of the fibre (region 3).
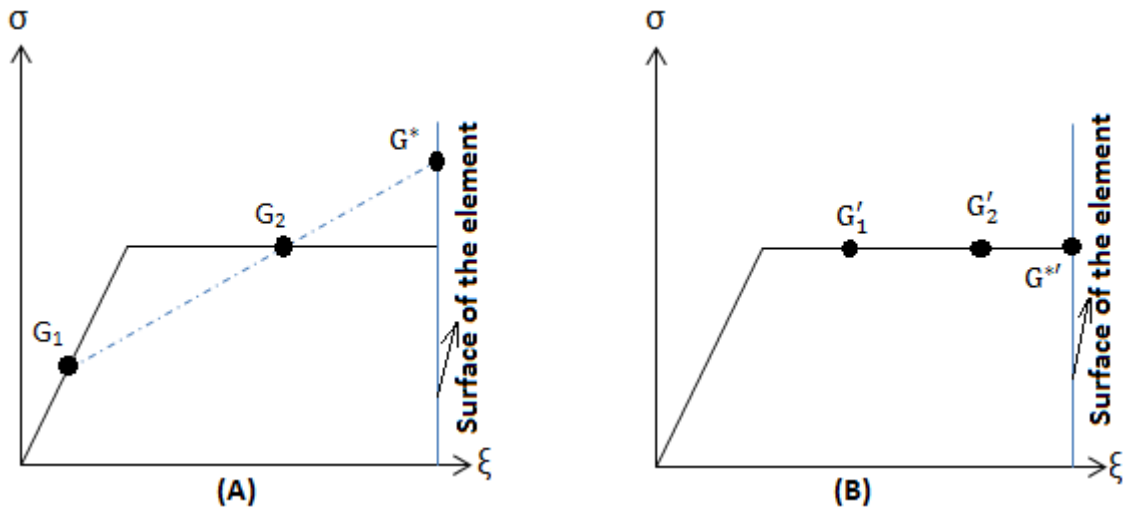
Figure 5-30. Interpolation of two Gauss points to the surface of an element.

The equivalent plastic strain experienced by the second bend of the fibre (region (4)) increases as the bend is straightened and then plateaus once the region enters the long straight part of the curve (Figure 5-31). Finally, region (5), the straight horizontal part of the curve, experiences some plasticity as a result of the straightening of the second bend, after which there is a plateau (Figure 5-32).
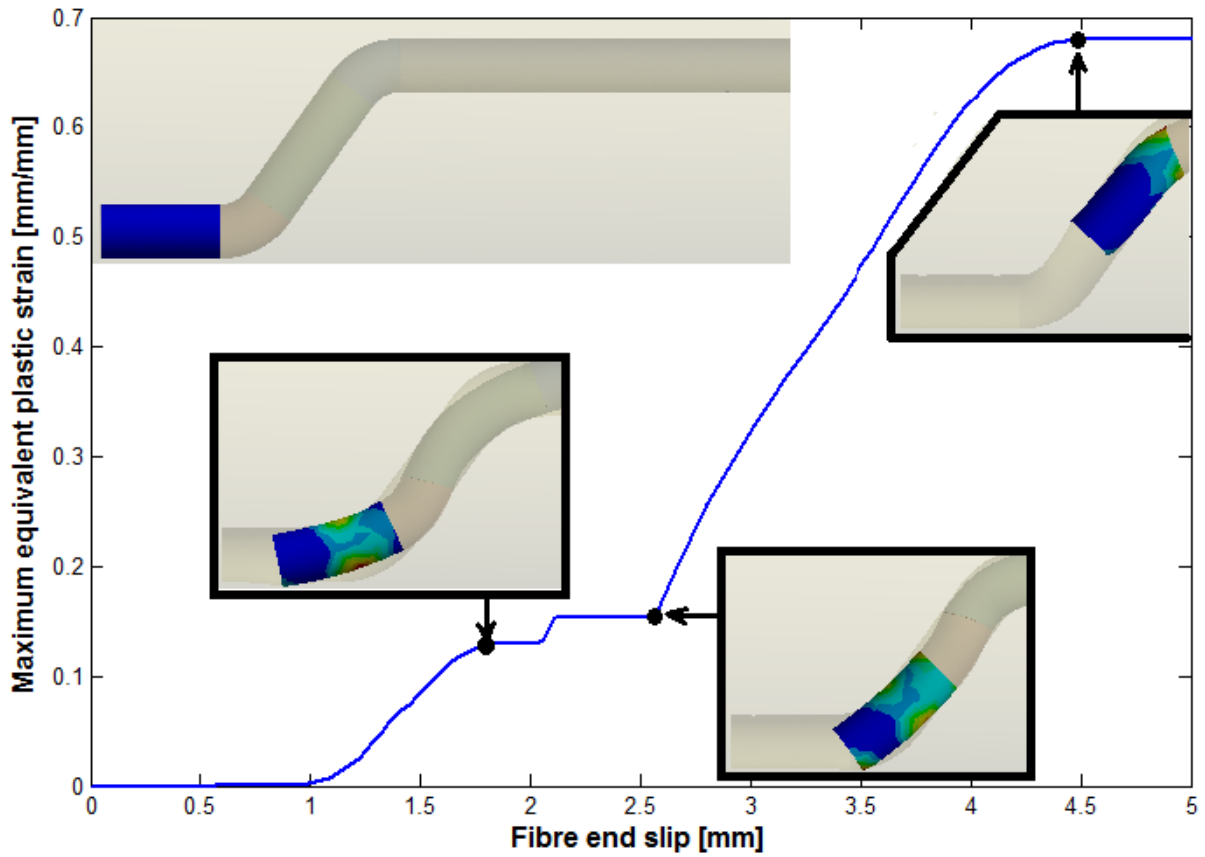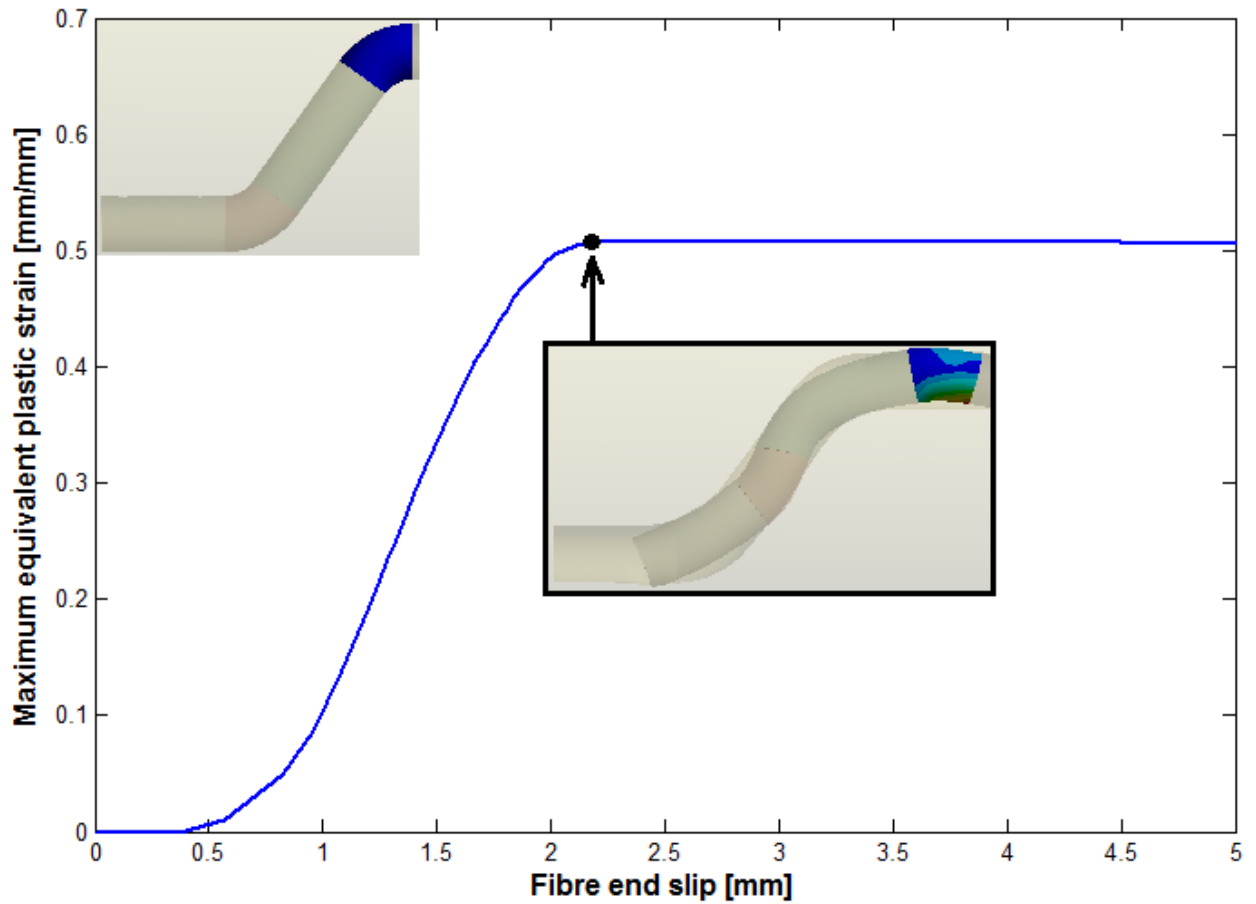
Figure 5-31. Maximum equivalent plastic strain experienced by the second bend of the fibre (region 4).
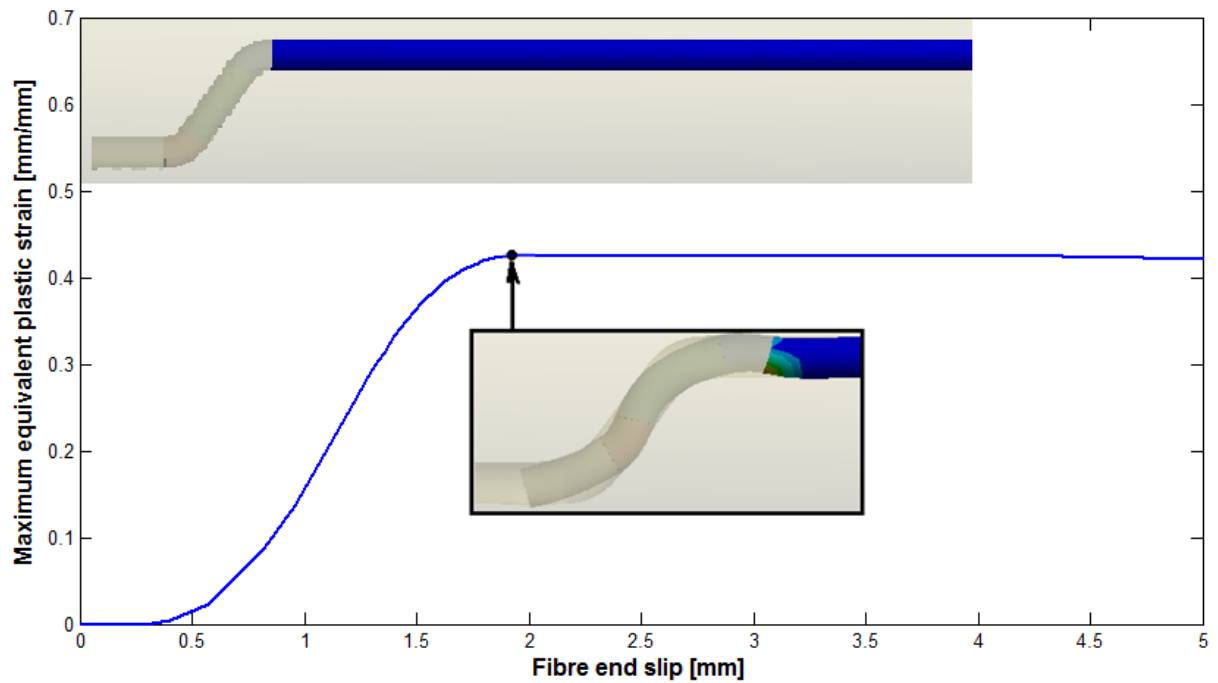
Figure 5-32. Maximum equivalent plastic strain experienced by the second straight horizontal part of the fibre (region 5).

Superposition of the maximum equivalent plastic strain figures allows us to develop a global understanding of the plastic behaviour of the fibre. As can be seen in Figure 5-33, initially there is no accumulation of plastic strain demonstrating that, in the beginning of the pull-out, the fibre first deforms elastically. Plastic deformation begins at different times in the different regions of the fibre, as shown in Figure 5-34, which magnifies the early pull-out stage. It is noticeable that plastic deformation starts in pairs of the fibre regions. The straight inclined part and first bend is the first pair to undergo plastic deformation whilst other parts still deforming elastically. This is followed by the second straight horizontal part and second bend pair. The tail of the fibre is the last to undergo plastic deformation and is the part that went through much more elastic and plastic deformation than the others. Notice that the peak in equivalent plastic strain, for different parts of the fibre, is dependent on the path followed by the material. The tail has deformed the most because it has to deform through the first and second bends of the matrix. Figure 5-33 and Table 5-14 illustrate clearly that the maximum equivalent plastic strains are in the following decreased order: tail, first bend, straight inclined part, second bend, and second straight horizontal part. Additional details of the fibre's plasticity are provided in Appendix D.
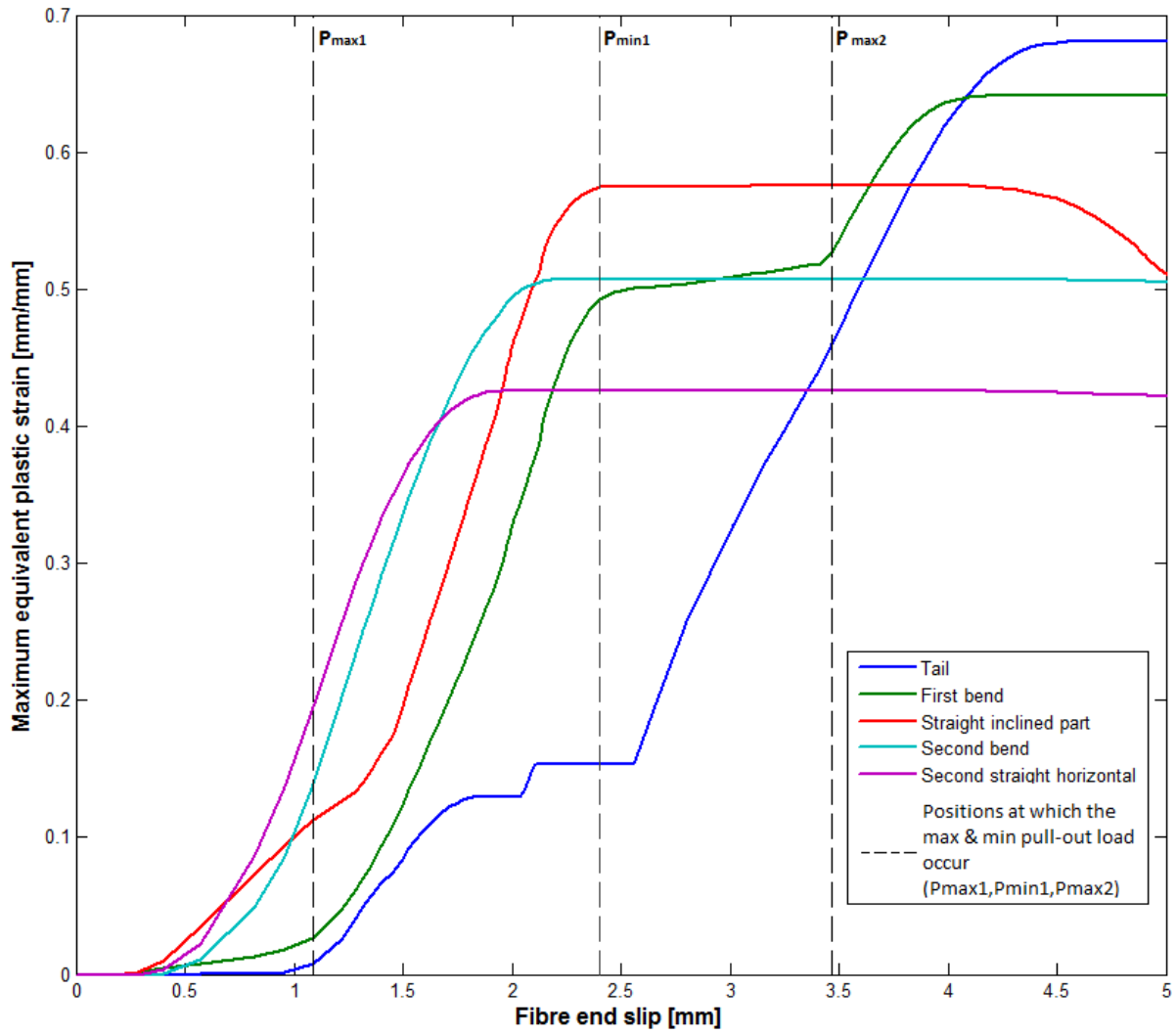
Figure 5-33. Superposition of the different maxima equivalent plastic strains (of the regions of the fibre) with the positions (displacements) at which maxima and minimum pull-out load occur.
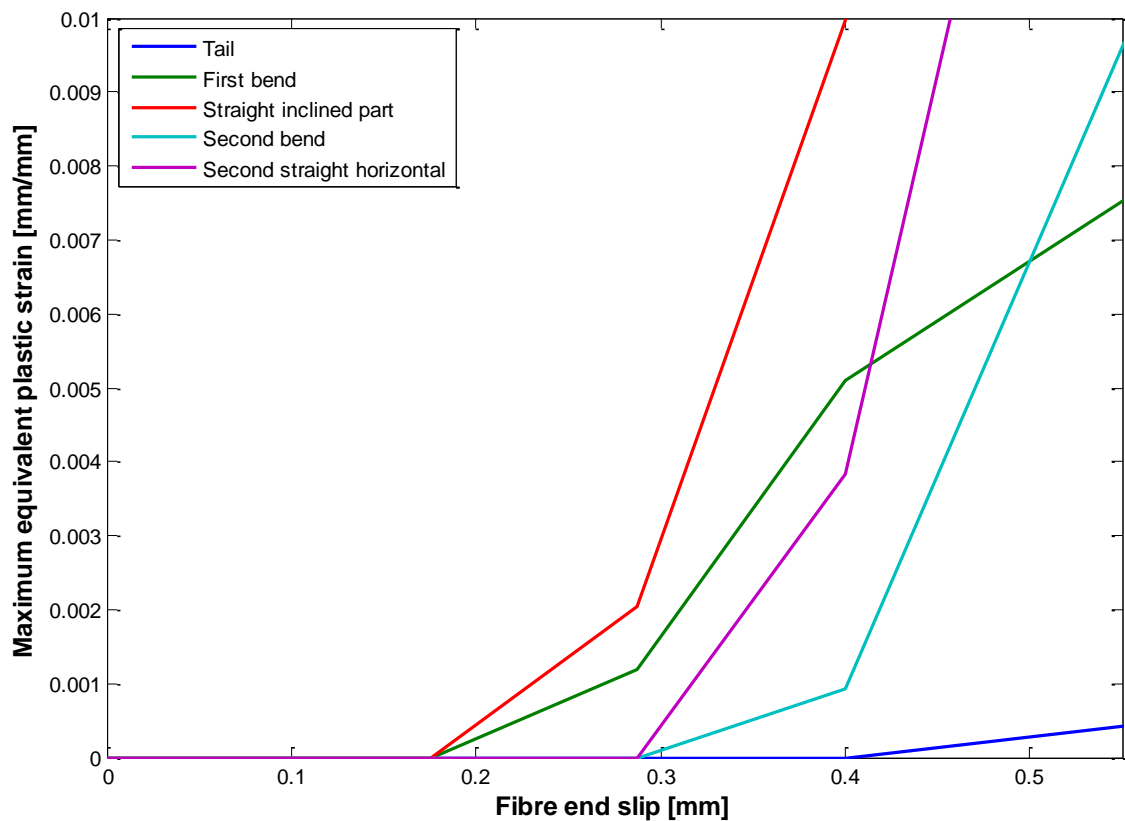
Figure 5-34. Maximum equivalent plastic strain in the early stage of the pull-out.

Table 5-14. Maximum value of the maximum equivalent plastic strain experienced by each part of the fibre.

	Tail	1st bend	Straight inclined part	Second bend	2nd straight horizontal part
Max. equiv. plastic strain [mm/mm]	0.681	0.642	0.575	0.507	0.426

In closing, it is of paramount importance to explain what the maximum equivalent plastic strain plateaus means and to correlate it with the physics of the fibre during pull-out. As has been previously explained, the plateau means that there is no additional plastic deformation during that period of time, only elastic deformations are experienced by the part of the fibre. Apart from the initial plateau, it can be observed from Figure 5-33 that the tail goes through three other plateaus, however the two first can be simulated as one plateau since the variation from the first to the second is not that much. The first bend two plateaus, whereas the remaining regions only show one plateau (see Figures 5-29, 5-30, 5-32). It can be observed that except for Figure 5-32, each plateau corresponds to the passage of a particular part through the bend of matrix. That is, the tail and the second bend of the fibre

have experienced two plateaus, because they have to pass through two bends of the matrix, while other parts experienced only one plateau, because they have to pass through only one bend of the matrix.

The physics of these plateaus can be explained by considering, for example, one element located at position 1 (see Figure 5-35). This element will have to pass all along the tunnel through positions 2, 3, 4 and 5. At position 2 the element has plastically deformed (yielded) through the first bend with increasing plastic strain. As the process continues, the passing of the element from position 2 to 3 will force the element to straighten and thus reverse the direction of straining. Plastic deformation is accompanied by change of positions of atoms in the crystal latice (Dowling, 2013). As the element changes from state 2 to state 3, dislocations are of opposite sign which will cause attraction and annihilation of one another and this will result in the softening of the material (Reza, 2009).
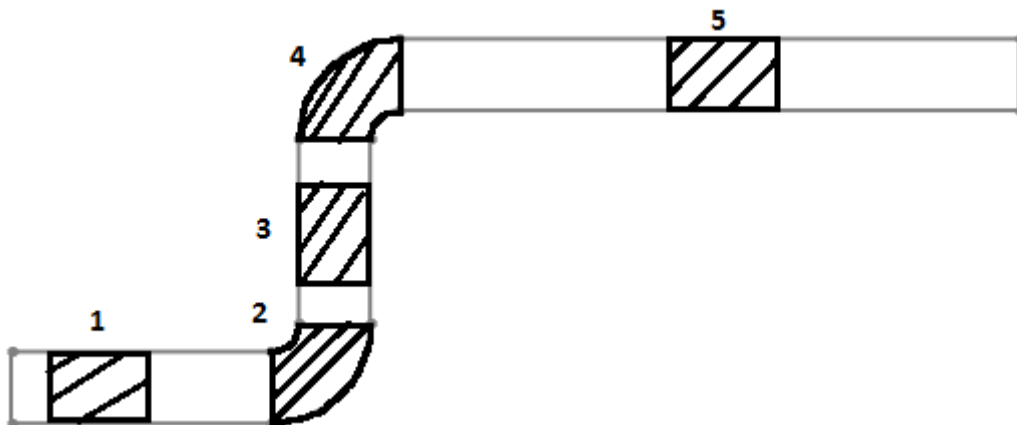
Figure 5-35. Fibre element in the duct of the matrix showing different steps of deformation: 1→2, 3→4: bending; 2→3, 4→5: reverse bending.

The reverse bending, states 2→3 and 4→5, could be simulated as a loading-unloading process for which the state of stress-total strain is shown in Figure 5-36(A) and stress-plastic strain in Figure 5-36(B) which shows a constant plastic strain during unloading process. As this process is twice repeated over two bends of the matrix (see Figure 5-35), thus two increases and two plateaus in equivalent plastic strain should be expected.
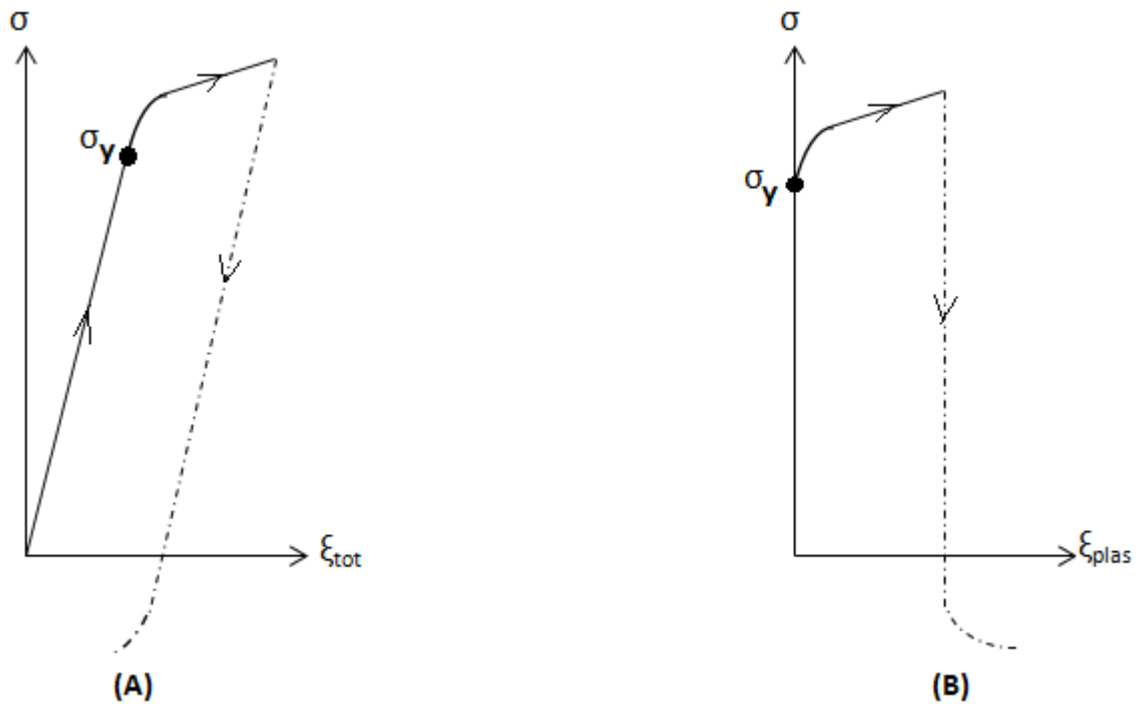
Figure 5-36. Stress-strain showing the loading and unloading process.

5.5.2. Investigating stress in the matrix

As a result of experimental studies which have revealed that the duct of the matrix experiences small deformation at both bends, numerical investigation was conducted in this regard by analysing the state of stress and deformation of the epoxy matrix. Figure 5-37 illustrates the maximum equivalent stress distribution of the matrix versus the fibre's end displacement. Three peaks of stress are observed in the duct of the matrix, C_1, C_2 and C_3, as summarised in Table 5-15.

It is observed that these peaks occur within an interval, which corresponds to the fibre end displacement of 1 to 4mm. As referred to the geometry of the matrix channel, this interval is located in the vicinity of two bends of the matrix. C_1 corresponds to penetration of the fibre tip, just prior to the tail entering the first bend; peak stresses occur at locations where the fibre is resisting straightening. C_2 corresponds to the positions of the fibre where the tail is about to enter completely the straight inclined channel of the matrix, whereas C_3 corresponds to the instant where the first bend of the fibre resists entering the second straight horizontal channel of the matrix.
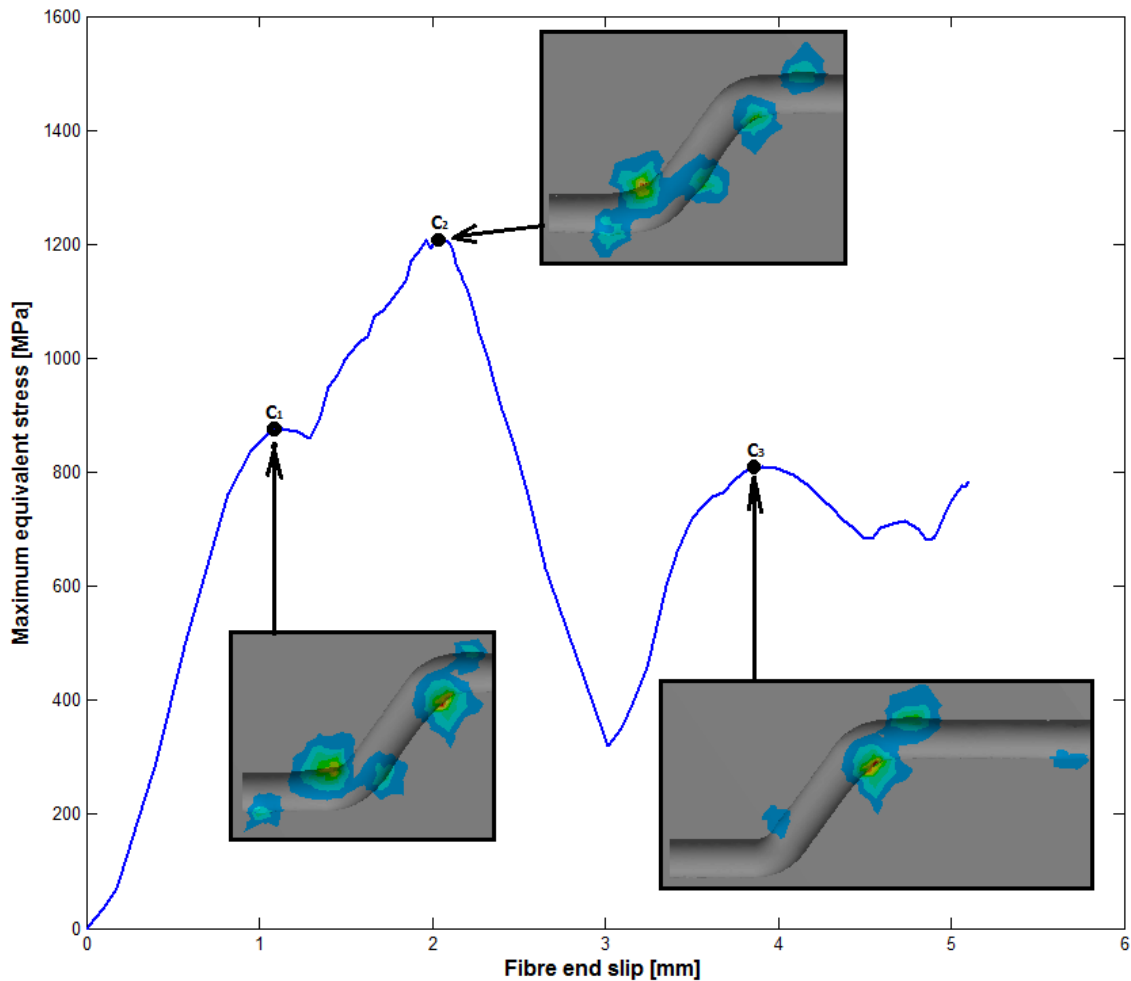
Figure 5-37. Matrix maximum equivalent stress distribution versus fibre's end displacement.

Table 5-15. Matrix maximum equivalent stress for selected points on the curve.

Selected points	Max equivalent stress [MPa]	Fibre's end slip [mm]
C_1	878	1.088
C_2	1210	2.035
C_3	810	3.913

Figure 5-38 shows the total deformation distribution, of the matrix, versus the fibre's end displacement. Two distinctive peaks (D_1 and D_2) are observed at respectively the fibre's end displacements of 1.964 mm and 3.842 mm. Correlations of these peaks (D_1 and D_2) with the deformation contour of the duct of the matrix are illustrated in Figure 5-37 where maximum deformations occur at a location situated in the near vicinity of the bends, and as compared to the results presented in Table 5-14, it is observed that the first maximum deformation (D_1) seems to occur quite at a time which is close to the second maximum equivalent stress (C_2) and that the second maximum deformation occurred near the third maximum equivalent stress (C_3), as seen in Figure 5-36 and Table 5-15.
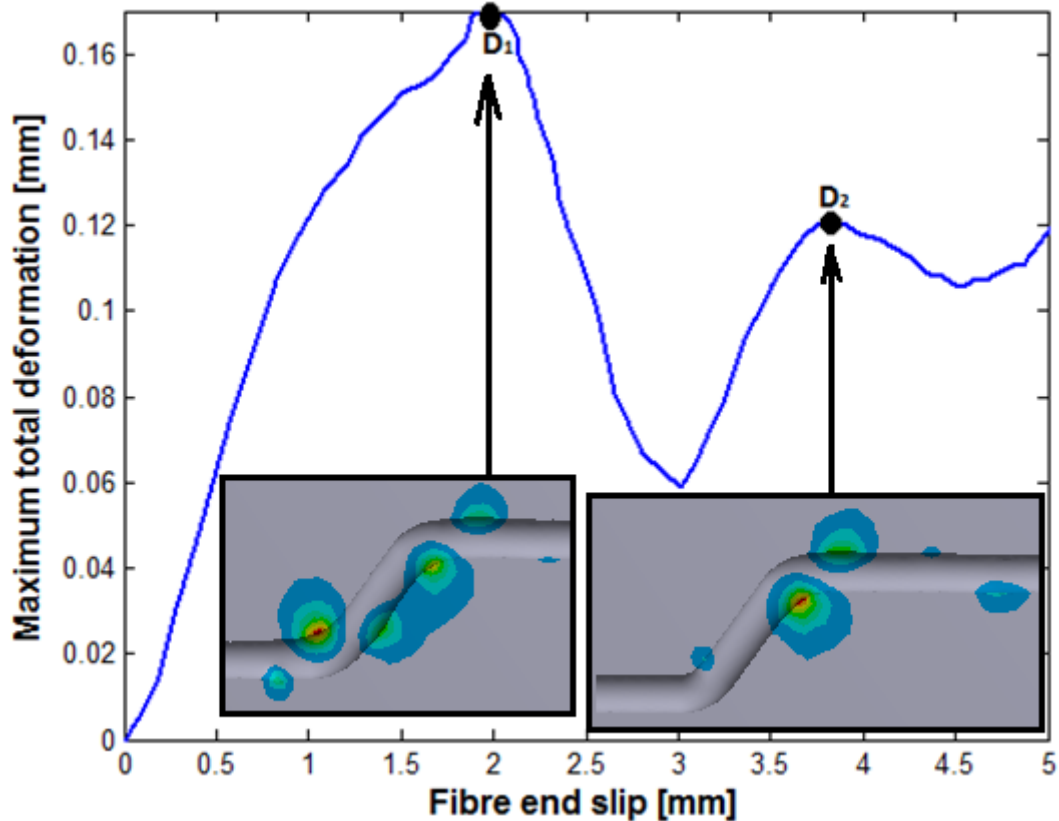
Figure 5-38. Matrix total deformation distribution versus fibre's end displacement.

5.6. Issues encountered during modelling

Most of the convergence issues encountered during numerical simulation were related to contact problems. As discussed earlier, prior to solving the entire problem, it was necessary to check whether or not contacting bodies were initially touching one another. Even though this condition was satisfied, convergence of the problem was not an immediate success as contact problems persisted. It was noticed that the residual outputs of Newton-Raphson (out of balance forces $\{F^a\} - \{F_i^{nr}\} = \{R\}$) were very high and thus influencing the convergence of the solution since these forces could not be reduced below the values required for convergence as stated by the convergence criterion $\{R\} < 0.1\,\%\{F^a\}$). This could be the result of significant interpenetration due to the problem geometry, leading to high Newton-Raphson residual. The solution to this problem was to reduce the contact stiffness; this helped obtaining convergence at reduced equilibrium iterations.

6. COMPARISON BETWEEN THE UPDATED NUMERICAL MODEL AND EXPERIMENTAL PULL-OUT CURVES

Numerical force-displacement results (dotted lines) are shown in Figure 6-1 for model parameters as listed in Table 6-1., with representative experimental results plotted on the same graph. As can be seen in this figure, the pull-out behaviour is similar for both experimental and numerical curves. They exhibit similar patterns, in that there is initially a fairly linear increase of the pull-out load up to the first maximum then a sudden decrease in load to the first minimum followed by another increase to the second peak before a catastrophic drop.

It should be remembered that the experimental curves present a huge variation in load magnitude but displacements of the fibre for specific events are roughly the same. For this reason, in the current study attention will particularly be paid on the comparison of experimental fibre end displacements with the numerical ones. This comparison is shown in Table 6-2 and Figure 6-2, where the locations of interest are those defined in Figure 4-10.

These comparisons are presented in form of a graph showing both, experimental and numerical displacements corresponding respectively to the first peak (P_{max1}), first minimum (P_{min1}), second peak (P_{max2}) and second minimum (P_{min2}).

Table 6-1. Numerical model parameters.

Steel fibre						Matrix
Tangent modulus	Elastic modulus	Virgin yield stress	Plasticized yield stress	Coefficient of friction	Spring stiffness	Elastic modulus
E_T [GPa]	E_f [GPa]	σ_{YV} [GPa]	σ_{YPl} [GPa]	μ	K [kN/mm]	E_m [GPa]
0.1	196	1	1.2	0.05	1	3
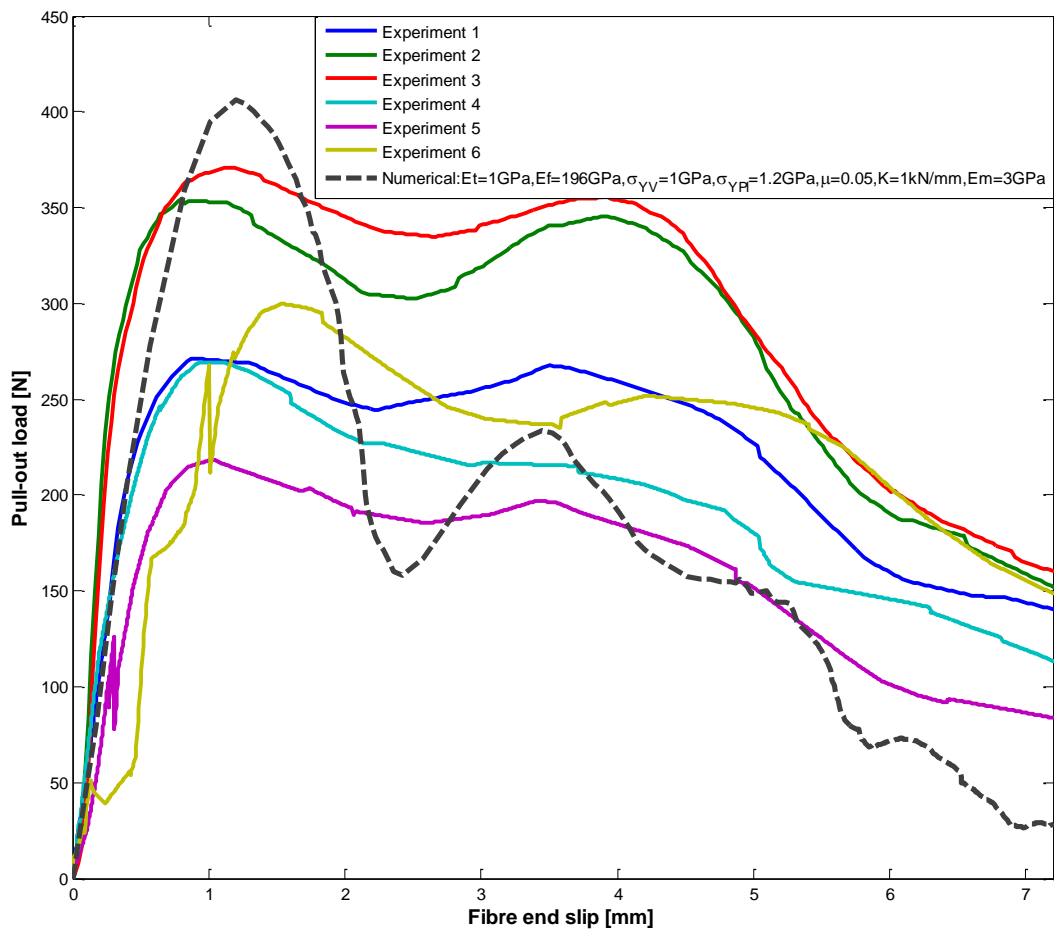
Figure 6-1. Comparison of the updated numerical model to experimental curves.

Table 6-2. Comparison of numerical displacements with experimental ones

Experimental	Fibre's end displacement [mm]			
	Δ_{max1}	Δ_{min1}	Δ_{max2}	Δ_{min2}
1	1.166	2.637	3.922	8.363
2	0.8014	2.506	3.905	8
3	1.539	3.573	4.214	8.937
4	0.9273	2.247	3.538	8.114
5	0.9243	2.89	3.713	10.03
6	1.03	2.59	3.436	8.262
Average	1.065	2.741	3.788	8.618
Numerical 1	1.202	2.421	3.449	6.918
Standard deviation.	0.0685	0.16	0.1695	0.85

Results presented in Table 6-2 and Figure 6-2, show that there is agreement between the numerical and experimental displacements. Only slight discrepancies are observed for the three first events at which the fibre is at a location corresponding to the first maximum load

(P_{max1}), first minimum load (P_{min1}) and second maximum load (P_{max2}). It is also observed that for the last event, where the fibre reaches the position at P_{min2}, the numerical displacement experienced a big delay as compared to the experimental displacement.
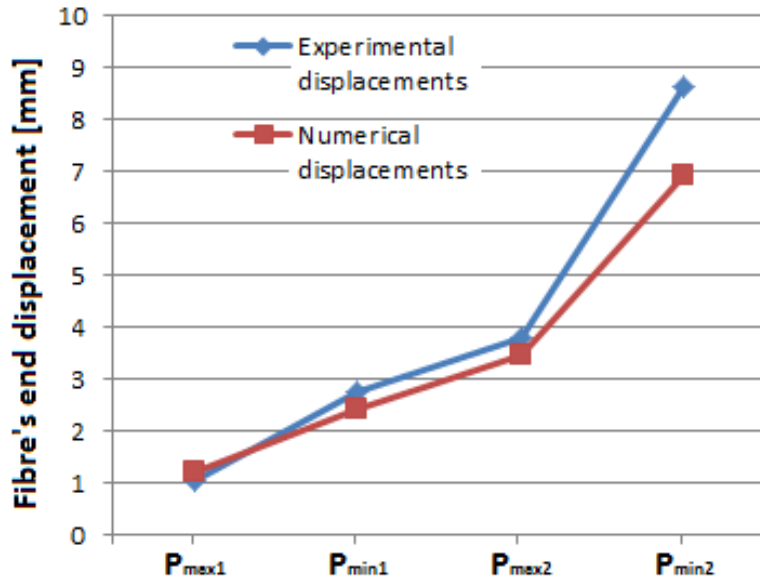
Figure 6-2. Numerical fibre's displacements compared to experiment displacements.

7. FINAL CONCLUSIONS AND RECOMMENDATIONS

The present study dealt with the pull-out of hooked end steel fibre from an epoxy matrix. The main aim was to understand the pull-out behaviour of the mentioned fibres from a concrete matrix. But as plastic deformation of the fibre had to be visualised directly, while the pull-out process evolves, in order to correlate the fibre displacements to specific points of interest selected on the pull-out curve, studies have been conducted by substituting the concrete matrix by a clear material which should almost have the same mechanical properties as the concrete's; the stiffness and the Poisson's ratio of the matrix were the considered parameters.

Experimental studies have provided all processes involved in the composite manufacturing and the characterisation of mechanical properties of composite constituents for numerical implementation purposes. The pull-out behaviour was characterised by means of a curve of pull-out load versus fibre slip correlated with the positions of the fibre in the duct of the matrix during pull-out. Numerical studies were introduced so as to help understand experimental studies by providing extra information which could not be easily determined experimentally.

In Chapter 3, characterisation of hooked end steel fibre and epoxy matrix were conducted by means of tensile tests on specimens. These results provided the tensile strength (σ_{u-f}), the Young's modulus (E_f) and the proportional limit value which was considered as the yield point of the fibre (σ_P).

This chapter also includes the manufacturing process of epoxy. As far as the epoxy manufacturing process is concerned, selection of suitable raw materials involved in the fabrication of a clear matrix with a moderate stiffness was conducted followed by the casting of the composite which is a half dog bone epoxy matrix embedding a single hooked end steel fibre. In order to comply with the established requirements, a clear matrix with a moderate stiffness, it was decided to combine the epoxy resin with a typical hardener. Two types of epoxy resins were utilised, CP25 (clear polyester resin) and LR151, with three different type of hardeners which are Merck Catalyst hardener, EH16 and EH96. Merck Catalyst hardener is combined with CP25 epoxy whereas EH16 and EH96 are the corresponding hardeners of LR151 epoxy resin. Combination of CP25 resin with Merck

Catalyst hardener resulted, after curing in room temperature for 48 hours, in a stiffer matrix with a slight yellowish-orange colour. But LR151 resin combined with EH96 hardener resulted in a clear and moderately stiff matrix. In contrary, LR151 resin and EH16 hardener resulted in a clear and soft matrix. Therefore the only suitable combination was LR151 resin with EH96 hardener, used in a ratio of $5:1$ by volume.

It was found that mixing of epoxy resin with a corresponding hardener results in an exothermic chemical reaction (releasing heat). These effects were not observed in mixing of small amount of mass, but only when large amount of mass of mixture was prepared. Excessive heat generations could be remedied by placing a coolant system around the mixing container, for example a cold running water (Cook *et al.*, 1989).

Chapter 3 provides experimental results as well. Mechanical characteristics of epoxy are determined by means of a tensile test, which provides the tensile strength ($\sigma_{u\text{-}m}$) and the elastic modulus (E_m) of the epoxy matrix.

In Chapter 4, results of experimental pull-out are provided in a form of graphs of pull-out load versus fibre slip. Six tests were performed and all graphs exhibit the same characteristic pull-out behaviour: the initially linear load increases up to the peak pull-out load, then drops off to a local minimum. The load then increases again up to a second peak (lower than the first maximum) after which it drops rapidly. Microscopic observations of the matrix, after pull-out, have shown that slight deformations (spalling) were observed in the duct of the matrix, more precisely in the inclined zone of the duct in the vicinity of the bends.

Chapter 5 dealt with the numerical studies in order to compere to the experimental pull-out results. Based on experiment pull-out results, which show plastic deformation of the fibre and elastic behaviour of the matrix, a 3D nonlinear finite element model involving friction and nonlinear contact was created in ANSYS. The matrix was defined as isotropic elastic and the fibre as von Mises plasticity with bilinear isotropic hardening. Mechanical properties of the fibre and matrix, determined in Chapter 3, were used as input in the numerical model. Results with the initial material definition were not satisfactory since the numerical pull-out curve was too stiff as compared to the experimental response. Improvement of the numerical model was achieved by taking into account physical effects. The model was updated by taking into account the compliance of the testing machine, which was modelled by a linear deformable spring (of stiffness K) attached at the free end of the fibre. It was

also found that the yield point which was determined as a proportional limit (σ_P), by means of a tensile test, was underestimated. Given that the tensile test was unable to capture the plastic behaviour of the fibre, bending tests were conducted on the fibre and that provided the tangent modulus (E_T) and the yield point of the fibre (σ_{YV}). These properties, referred to as the virgin steel wire properties, were only valid for undeformed parts of the fibre (straight sections). Results have shown that the proportional limit (σ_P) characterised in Chapter 3 was under estimated and that the tangent modulus, which in previous simulation was only guessed, was over estimated.

Due to the fact that the bends of the fibre have undergone significant prior plastic deformation during the forming process, a second yield stress pertaining to these work-hardened parts has been defined. The work-hardened yield stress (σ_{YPl}) was found difficult to measure experimentally, but was rather estimated to be higher than the virgin material's yield stress (σ_{YV}).

Based on sensitivity studies of different parameters involved in the numerical model, it has been found that the peak pull-out loads are sensitive to variations of the fibre yield stresses (σ_{YPl} and σ_{YV}), the frictional coefficient (μ), the epoxy stiffness (E_m), and the fibre tangent modulus (E_T). The fibre displacements vary with the spring stiffness (K).

Numerical studies have revealed that the two peaks, observed in the experimental pull-out curve, are caused by bending and straightening of the work-hardened sections of the fibre. Based on plastic strain results of the fibre, it has been found that in the early stage of pull-out the fibre deforms elastically. Thereafter, plastic deformations are initiated in sections of the fibre while the remainder continues to deform elastically. The straight inclined part and the first bend of the fibre is the first to start deforming plastically, followed by the pair of second straight horizontal part and the second bend and finally the tail. Deformation and stress investigations on the epoxy matrix have revealed that only parts in the vicinity of two bends of the matrix were subjected to high stresses and deformations, as revealed by experimental studies.

Comparison of the numerical pull-out response to the experimental results is made in Chapter 6. Although the numerical model captures the physical features observed in the experimental results, there are still discrepancies in the peak loads, as well as the number of peaks observed. Improvement of the model could be achieved by considering debonding

effects, and by accounting for imperfections in the manufacturing process. The present study has modelled friction as isotropic with a single coefficient of friction (μ_{iso}) representing a uniform stick-slip behaviour in all direction. Different stick-slip behaviour in different directions could also be investigated by modelling friction as orthotropic. Furthermore, parametric optimisation of different features involved in the sensitivity study could be conducted.

8. REFERENCES

ACI 1996. State of the art: Report on fibre reinforced concrete. *Committee 544*.

ACI 2006. Reinforcement for concrete- Materials and applications. *Materials for concrete construction/Bulletin E2-00/Committee E-701*.

ALWAN, J. M., NAAMAN, A. E. & GUERRERO, P. 1999. Effect of mechanical clamping on the pull-out response of hooked steel fibres embedded in cementitious matrices. *Concrete Science and Engineering,* 1**,** 15-25.

ALWAN, J. M., NAAMAN, A. E. & HANSEN, W. 1991. Pull-out work of steel fibers from cementitious composites: Analytical investigation. *Cement and Concrete Composites,* 13**,** 247-255.

AMETEK. 2009. *EZ Series, EZ50 50 kN universal material testing machine (Specification sheet-Lloyd Instruments, Ltd, November 2009, SS-MT-B255-0909)* [Online]. Available: http://www.lloyd-instruments.com/Products/Twin-column-bench/EZ50.aspx [Accessed 30-10-2013].

ANDERSEN, T. L., BECH, J. I., LILHOLT, H., QING, H. & PRABHAKARAN, R. T. D. 2011. Modelling and experimental characterization of steel fibre/polymer interface: Pull-out tests. *Composites and Materials Mechanics, Materials Research Division, Risø National Laboratory for Sustainable Energy, Risø DTU, Technical University of Denmark, Fredericksborgvej 399, 4000, Roskilde, Denmark.*

ANSYS-HELP. 2009. *Contact technology guide* [Online]. Available: http://orange.engr.ucdavis.edu/Documentation12.1/121/ans_ctec.pdf [Accessed 30-10-2013.

ANSYS-INC. 2010. *Lecture 3: ANSYS Mechanical structural nonlinearities-Introduction to contact* [Online]. Available: http://inside.mines.edu/~apetrell/ENME442/Labs/1301_ENME442_lab6_lecture.pdf [Accessed 16-10-2013.

ASTM. 2002. *Standard Test Method for Tensile Properties of Plastics (ASTM D638)* [Online]. Available: http://classes.engr.oregonstate.edu/mime/winter2012/me453-001/Lab1%20-%20Shear%20Strain%20on%20Polymer%20Beam/ASTM%20D638-02a.pdf [Accessed 10/10/2013.

BANHOLZER, B., BRAMESHUBER, W. & JUNG, W. 2005. Analytical simulation of pull-out tests—the direct problem. *Cement and Concrete Composites,* 27**,** 93-101.

BANHOLZER, B., BRAMESHUBER, W. & JUNG, W. 2006. Analytical evaluation of pull-out tests—The inverse problem. *Cement and Concrete Composites,* 28**,** 564-571.

BANTHIA, N., FAFARD, M. & MALLIKARJUNA 1992. A new three-dimensional interface (contact) element for fiber pull-out behavior in composites. *Journal of Computers and Structures,* 44**,** 753-764, 1992.

BHASHYAM, G. R. 2002. *ANSYS Mechanical-A powerful nonlinear simulation tool* [Online]. Available: http://ansys.net/ansys/papers/nonlinear/ansys_mechanical_wp.pdf [Accessed 30-10-2013.

BOTHMANN, R. 2004. *Techniques for successfully using ANSYS contact elements* [Online]. Available: http://www.scribd.com/doc/205367275/Contact-Element-Techniques [Accessed 05-03 2014].

BRANDT, A. M. 1995. *Cement based composites materials: mechanical properties and performance,* Warsaw/Poland, Institute of Fundamental Technological Research/Polish Academy of Sciences.

CAPRANI, C. 2006. *Civil Engineering Design (1), Prestressed concrete* [Online]. Available: http://www.colincaprani.com/files/notes/CED1/PSC%20Notes.pdf [Accessed 30-10-2013.

COOK, R. D., MALKUS, D. S., PLESHA, M. E. & WITT, R. J. 2002. *Concept and applications of finite element analysis,* University of Wisconsin/Madison/USA, John Willey & Sons, INC.

COOK, R. F., THOULESS, M. D., CLARKE, D. R. & KROLL, M. C. 1989. Stick-slip during fibre pull-out. *Scripta Metallurgica,* 23**,** 1725-1730.

CUNHA, V. M. C. F., BARROS, J. A. O. & SENA-CRUZ, J. M. 2008. Bond-slip mechanisms of hooked-end steel fibers in self-compacting concrete. *Materials Science Forum,* 587-588**,** 877-881.

DOWLING, N. E. 2013. Mechanical behavior of materials, Engineering mathods for deformation, fracture, and fatigue. *Blacksburg/Engineering Science and Mechanics Department, and Materials Science and Engineering Depatment,* Fourth Edition.

GEORGIADI-STEFANIDI, K., MISTAKIDIS, E., PANTOUSA, D. & ZYGOMALAS, M. 2010. Numerical modelling of the pull-out of hooked steel fibres from high-strength cementitious matrix, supplemented by experimental results. *Construction and Building Materials,* 24**,** 2489-2506.

GROSSE, C. & WEILER, B. 1996. Pull-out behaviour of fibres in steel fibre reinforced concrete. *Otto Graf Journal (Annual Journal on Research and Testing of Materials, Otto Graf Institute, Research and Testing Establishment for Building and Construction [FMPA]-Part of the University of Stuttgart/Germany),* 7**,** 116-127.

HAMOUSH, S., ABU-LEBDEH, T., ZORNIG, B. & CUMMINS, T. 2010. Pull-out characterizations of various steel fibres imbedded in very high-strength concrete. *American Journal of Engineering and Applied Sciences,* 3**,** 418-426.

HUTCHINSON, J. W. & JENSEN, H. M. 1990. Models of fibre debonding and pull-out in brittle composites with friction. *Mechanics of Materials* 9**,** 139-163.

IMAOKA, S. 2001. *Sheldon's ANSYS tips and tricks, "Understanding Lagrange multiplier-Memo Number: STI:01/07* [Online]. Available: http://ansys.net/ansys/tips_sheldon/STI07_Lagrange_Multipliers.pdf.

IMAOKA, S. 2009. *Analyzing nonlinear contact-Convenient tools help analyse problems in which the contacting area between touching parts changes during the load history* [Online]. Available: http://www.ansys.com/staticassets/ANSYS/staticassets/resourcelibrary/article/AA-V3-I2-Analyzing-Nonlinear-Contact.pdf. [Accessed 30-10-2013.

KOK, S. 2013. Unpublished study *University of Pretoria/Department of Mechanical and Aeronautical Engineering, 2013*.

KRASNIKOVS, A., KHABAZ, A., TELNOVA, I., MACHANOVSKY, A. & KLAVINSH, J. 2010. Numerical 3D investigation of non-metallic (Glass, Carbon) fibre pull-out micromechanics (In concrete matrix). *Scientific Journal of Riga Technical University,* 33.

LARANJEIRA, F., MOLINS, C. & AGUADO, A. 2010. Predicting the pullout response of inclined hooked steel fibers. *Cement and Concrete Research,* 40**,** 1471-1487.

LEE, Y., KANG, S.-T. & KIM, J.-K. 2010. Pullout behavior of inclined steel fiber in an ultra-high strength cementitious matrix. *Construction and Building Materials,* 24**,** 2030-2041.

LIN, G., GEUBELLE, P. H. & SOTTOS, N. R. 2001. Simulation of fiber debonding with friction in a model composite pushout test. *International Journal of Solids and Structures,* 38**,** 8547-8562.

MARKOVICH, I., VAN MIER, J. G. M. & WALRAVEN, J. C. 2001. Single fiber pullout from hybrid fiber reinforced concrete. *Heron,* 46**,** 191-200.

MARTIN, H. S. 2005. Elasticity, Theory-Applications and Numerics. South Florida/USA: University of Rhode Island/Department of Mechanical Engineering and Applied Mechanics.

METRISIN, J. T. 2008. *Guidelines for Obtaining Contact Convergence* [Online]. Available: http://www.ansys.com/staticassets/ANSYS/staticassets/resourcelibrary/confpaper/2008-Int-ANSYS-Conf-guidelines-contact-convergence.pdf [Accessed 30-10-2013.

MOBASHER, B. & LI, C. Y. 1998. Finite element simulations of fibre pull-out toughning in fibre reinforced cement based composites. *Journal of Advanced Cement Based Materials,* 7**,** 123-132.

NAAMAN, A. E. 2003. Engineering steel fibres with optimal properties for reinforcement of cement composites. *Advanced Concrete Technology,* 1**,** 241-252.

NIKISHKOV, G. P. & ALTLURI, S. N. 1993. Implementation of a generalized midpoint algorithm for integration of elastoplastic constitutive relations for von-Mises hardening material. *Computers and Structures,* 49**,** 1037-1044.

RAJESHKUMAR, K., MAHENDRAN, N. & GOBINATH, R. 2010. Experimental studies on viability of using geosynthetics as fibres in concrete. *International Journal of Applied Engineering Research,* 1**,** 1-14.

REZA, T. 2009. *Lab course on deformation and fracture-The Bauschinger effect* [Online]. Available: http://lmm.epfl.ch/webdav/site/lmm/shared/TPDefandRupt0910/TPDefFract0910_Bauschinger.pdf.

TAYLOR, R. L. 2011. FEAP- A Finite Element Analysis Program. *Department of Civil and Environmental Engineering, University of California at Berkeley, Berkeley, California 94720-1710.*

TILLOVA, E., CHALUPOVA, M. & HURTALOVA, L. 2010. Evolution of the Fe-rich phases in recycled AlSi9Cu3 cast alloy during solution treatment. *Komunikacie,* 12**,** 95-101.

TREVORROW, T. 1984. *Steel reinforcement,* London and New York, Construction Press.

TSAI, K. H. & KIM, K. S. 1996. The micromechanics of fiber pull-out. *Journal of the Mechanics and Physics of Solids,* 44**,** 1147-1177.

TUYAN, M. & YAZICI, H. 2012. Pull-out behavior of single steel fiber from SIFCON matrix. *Construction and Building Materials,* 35**,** 571-577.

WANG, Y., LI, V. C. & BACKER, S. 1988. Modelling of fibre pull-out from a cement matrix. *International Journal of Cement Composites and Lightweight Concrete,* 10**,** 143-149.

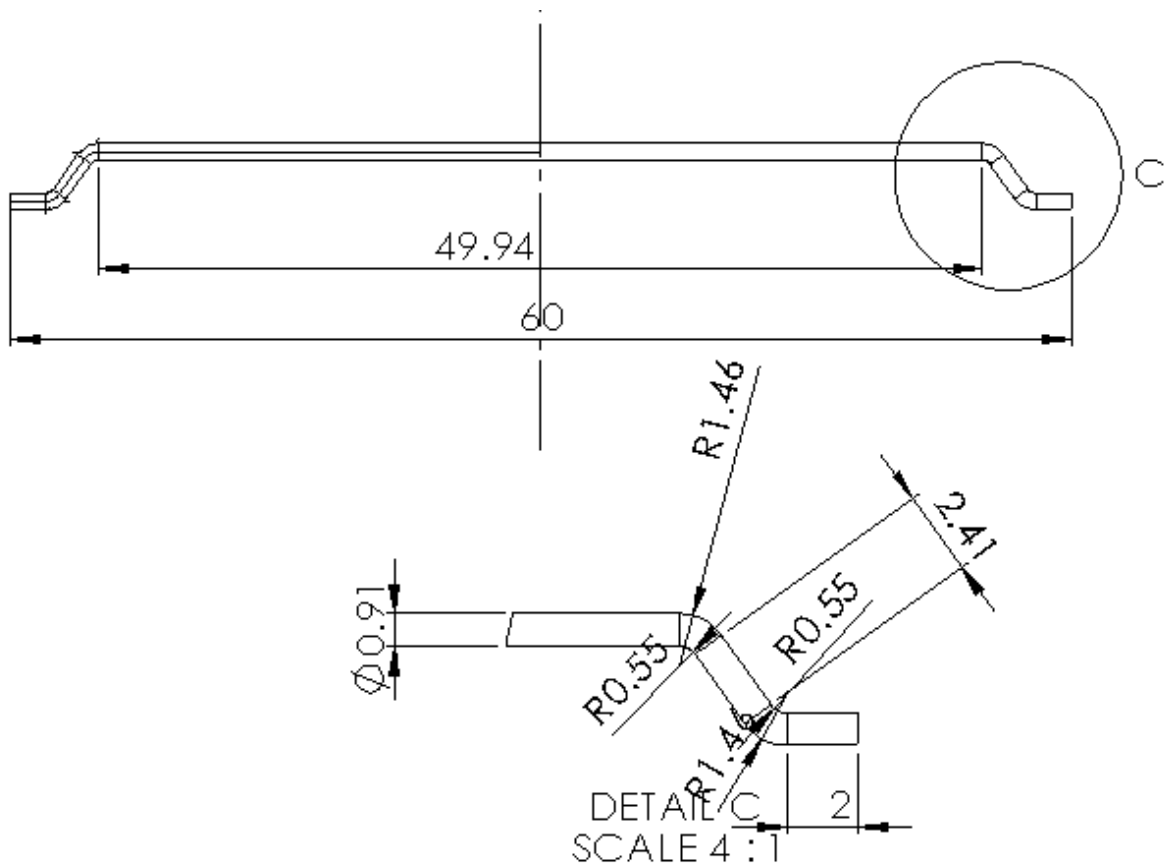## Appendix A   Drawing of hooked end fibre and dog bone shaped matrix

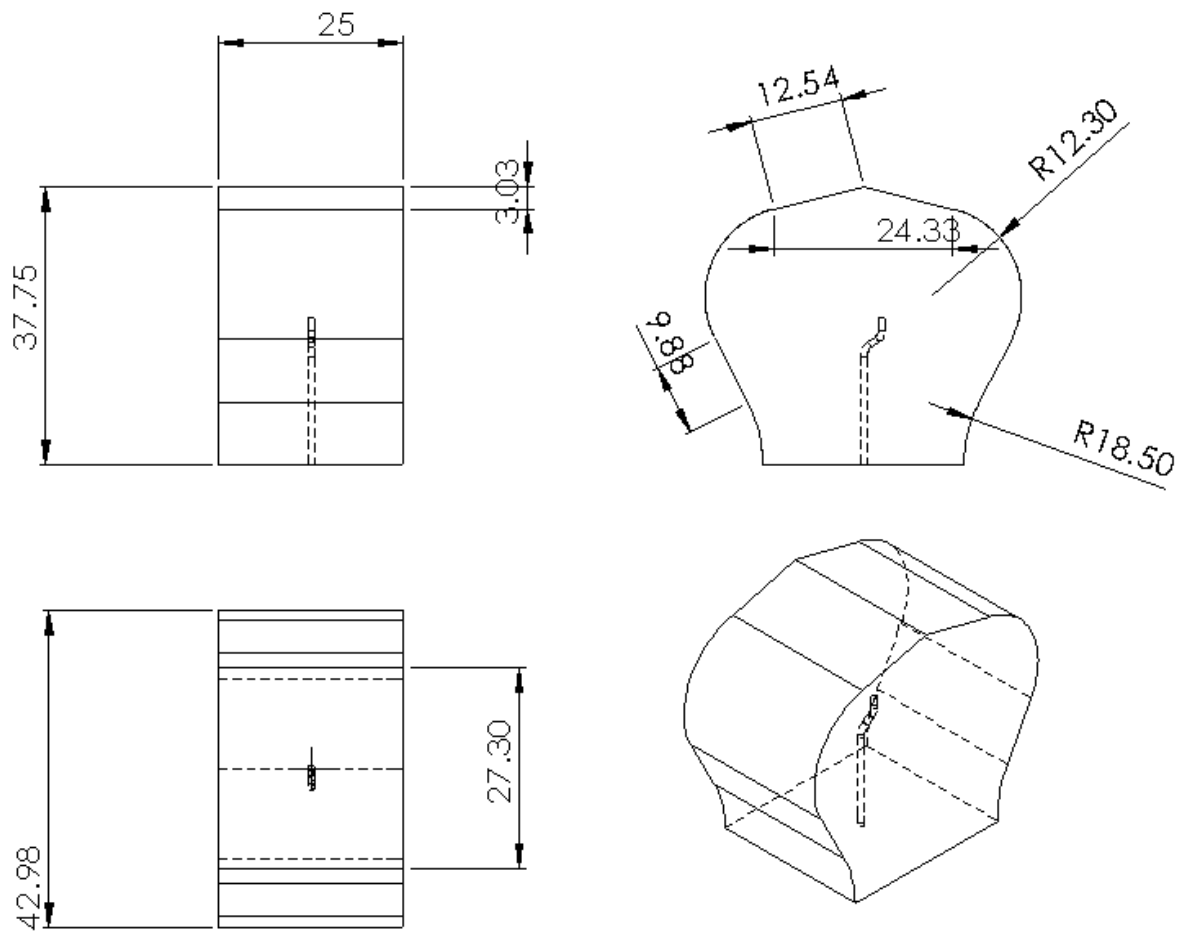**Figure A-1. Hooked end fibre.**

Figure A-2. Small dog bone shaped.

Appendix B   Contact status and the pinball region

ANSYS defines the contacting surfaces by "target or contact", and the position of each contact surface or element relative to the corresponding target surface (element) is characterised, as seen in Table B-1.

Table B-1. Definition of contact status.

		Contact configuration
Status value	0	Open far-field (open and not near)
	1	Open near field
	2	Sliding
	3	Sticking

Notice that near-field contact refers to contact for which the integration points (Gauss points or nodal points) are within some distance, defined by the user, to the corresponding target surface. This distance is called the pinball region which in some case is a spherical (in 3D) or circular (in 2D) boundary surrounding each contact (or target) detection point.
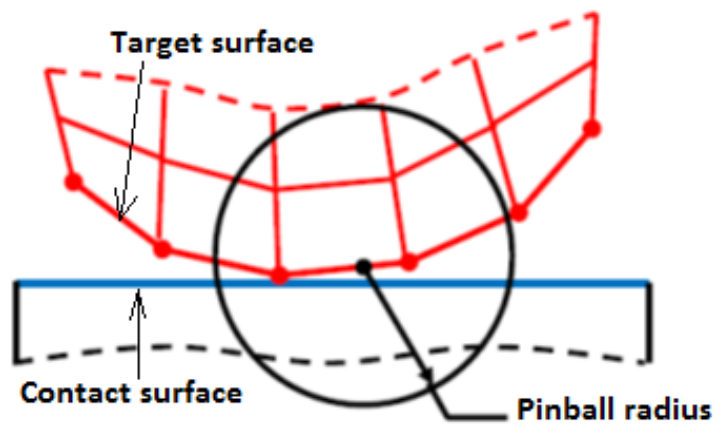

Figure B-1. Example of a pinball region. (ANSYS-Inc., 2010).

The pinball region helps in contact calculation efficiency, it evaluates the allowable gap for bond contact and finally it calculates the depth of initial interpenetration of the contacting surfaces.

Appendix C   Results of the first attempted numerical modelling

The first numerical modelling of the fibre pull-out was performed with the material definition presented in Table C1. The steel fibre is defined as a bilinear isotropic hardening material whereas the epoxy matrix is defined as an isotropic linear elastic material. Note that in these simulations the tangent modulus was not calculated but rather estimated because of lack of sufficient information from the stress-strain curve, presented in Figure 5-2, obtained from the tensile test of the steel wire.

Table C-1. Model parameters of the first attempted numerical modelling.

	Epoxy	Steel fibre
Poisson's ratio (v)	0.3	0.33
Tensile strength (σ_u) [MPa]	17	1200
Yield stress (σ_P) [MPa]	-	480
Young's modulus (E) [GPa]	3	196
Estimated Tangent modulus (E_T) [MPa]	-	2765

Appendix C.1.   Sensitivity studies of different parameters

The sensitivity studies have been conducted for the following parameters: the elastic modulus of the fibre (E_f), tangent modulus (E_T), yield stress (σ_Y) and the static frictional coefficient (μ). This was done in order to identify the parameters that would influence the magnitude of pull-out loads and the initial slope.

It should be noted that for computational cost reasons, simulations involving sensitivity studies have been purposely limited just after the peak load in order to compare with experimental results.

Appendix C.1.1. Impact of yield point

Increase of the yield stress σ_Y by 20 % from the baseline results in an increase of the peak pull-out load, as can be observed in Figure C-1. Therefore, the peak load of the model is yield point dependent. The material definitions for this analysis are given in the Table C-2.

Table C-2. Model parameters: varying yield point.

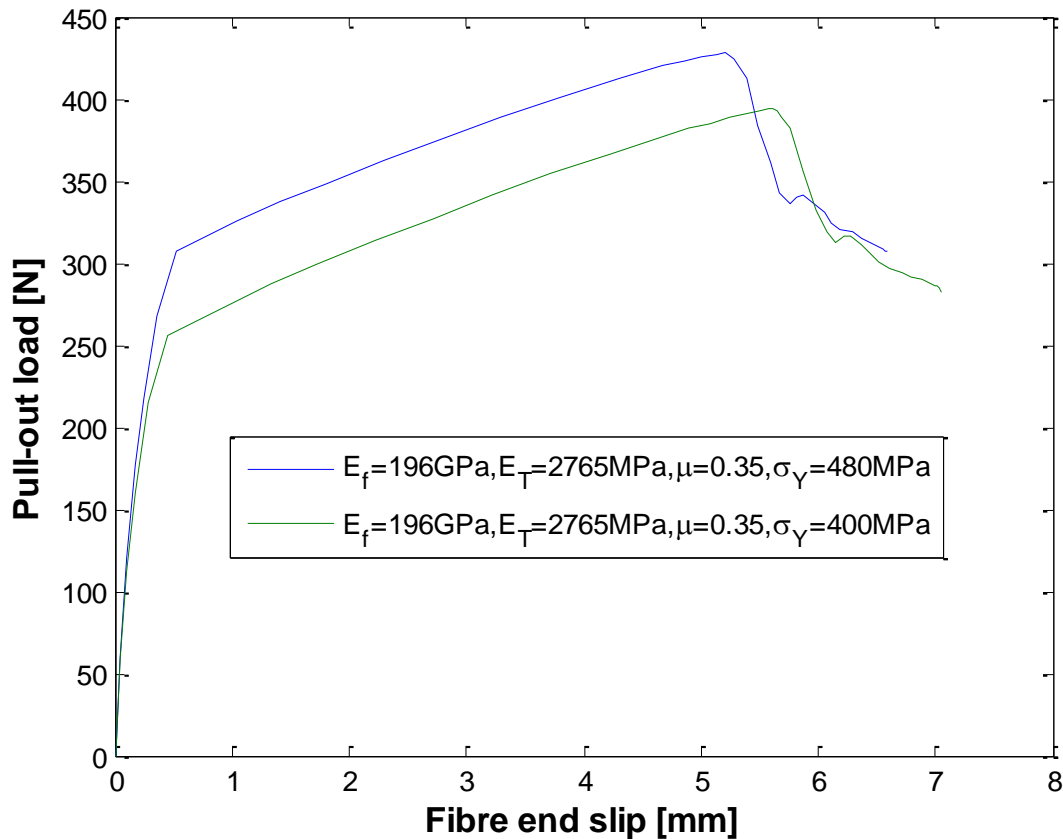| Simulation Number	Elastic modulus E_f [GPa]	Tangent modulus E_T [MPa]	Yield stress σ_Y [MPa]	Static coefficient of friction μ
1	196	2765	480	0.35
2			**400**	

Figure C-1. Sensitivity studies-Impact of the yield point on the model.

Appendix C.1.2. Impact of elastic modulus

These simulations were conducted with the elastic modulus E_f varying by 20% either side of the baseline, as shown in Table C-3. All other properties were held constant. Results presented in Figure C-2 show that variation of elastic modulus does not strongly affect either the slope of the curve or the peak pull-out load.

Table C-3. Model parameters: varying elastic modulus.

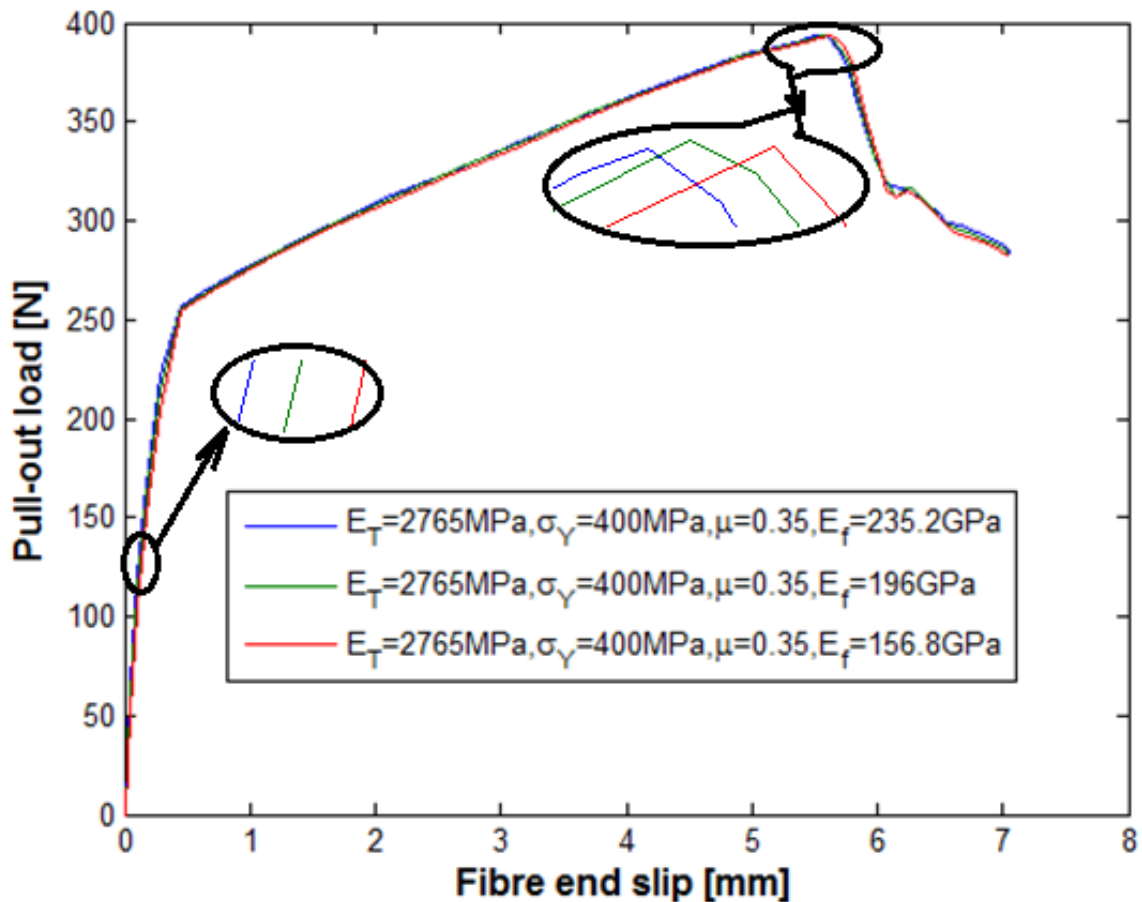| Simulation Number	Elastic modulus E_f [GPa]	Tangent modulus E_T [MPa]	Yield stress σ_Y [MPa]	Static coefficient of friction μ
1	157			
2	**196**	2765	400	0.35
3	235			

Figure C-2. Sensitivity studies-Impact of elastic modulus on the model.

Appendix C.1.3. Impact of tangent modulus

The tangent modulus E_T was increased by 20 % and 40 % from the baseline, while other properties were held constant. The material definitions are given in Table C-4. The pull-out responses of these material definitions are shown in Figure C-3. It is clear that the model is sensitive to the tangent modulus. The slope of the curve post-yield increases with increasing

tangent modulus, and the peak pull-out load also increases, while the fibre end displacement decreases slightly.

Table C-4. Model parameters: varying tangent modulus.

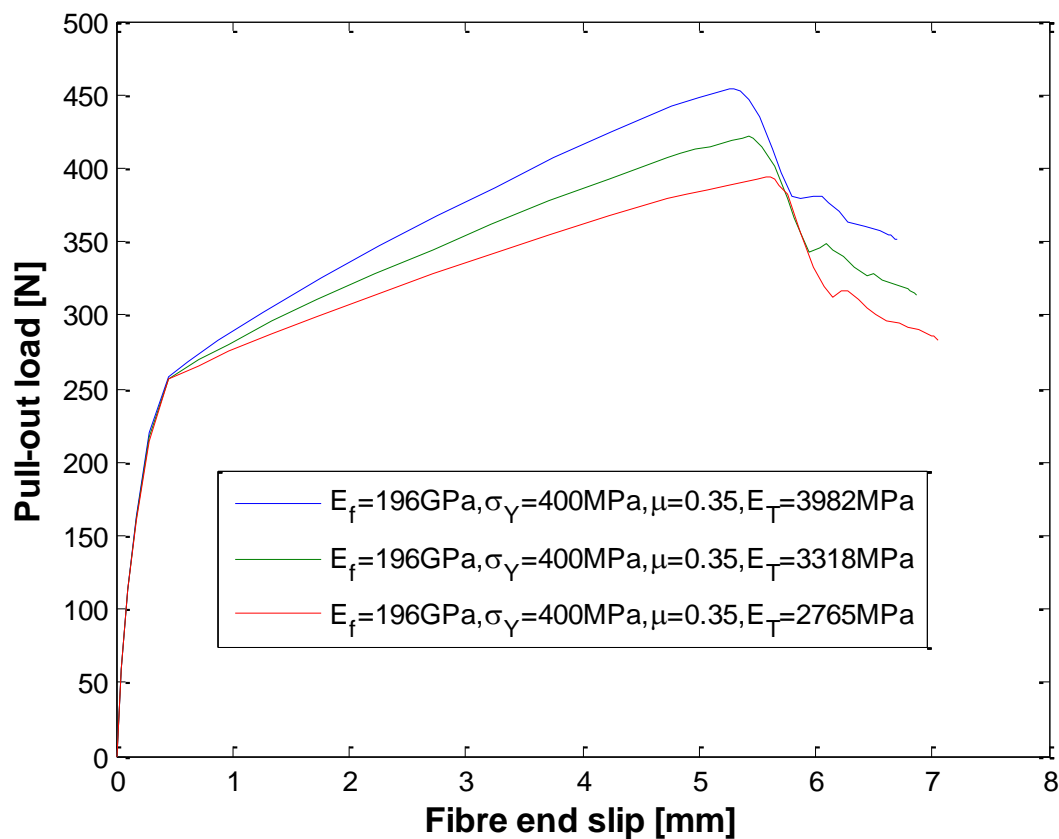| Simulation Number	Elastic modulus E_f [GPa]	Tangent modulus E_T [MPa]	Yield stress σ_Y [MPa]	Static coefficient of friction μ
1		3982		
2	196	3318	400	0.35
3		**2765**		

Figure C-3. Sensitivity studies-Impact of tangent modulus on the model.

Appendix C.1.4. Impact of static frictional coefficient

The last step of sensitivity studies was the verification of the effect of the static frictional coefficient on pull-out responses. It has been observed that the static coefficient of friction has a major impact on pull-out responses as seen in Figure C-4. The peak load and the corresponding displacement both decrease as the coefficient of friction decreases.

Table C-5. Model parameters: varying static frictional coefficient.

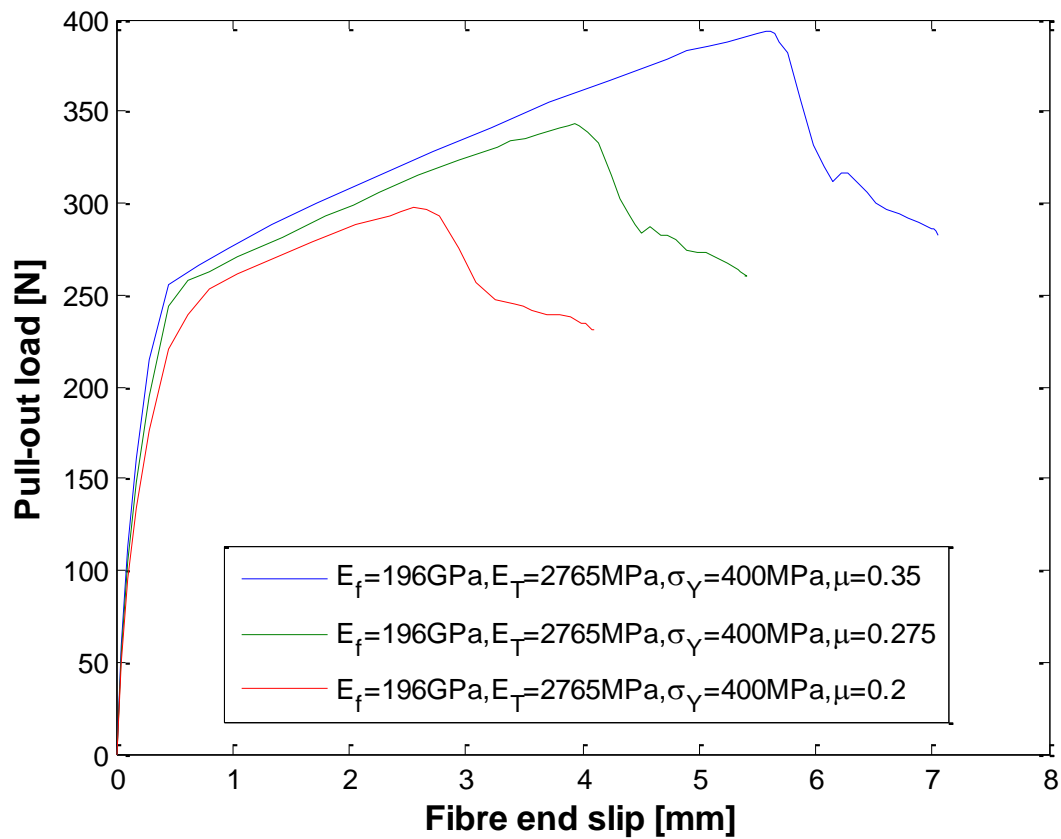| Simulation Number	Elastic modulus E_f [GPa]	Tangent modulus E_T [MPa]	Yield stress σ_Y [MPa]	Static coefficient of friction μ
1				**0.35**
2	196	2765	400	0.275
3				0.2

Figure C-4. Sensitivity studies-Impact of the static coefficient of friction on the model.

Appendix C.1.5. Comparison between the first attempted numerical model and experimental pull-out curves

Sensitivity studies have revealed that the numerical model is sensitive to three parameters: the tangent modulus and yield stress of the fibre, and the static frictional coefficient between the fibre and the epoxy matrix. Adjustment of these parameters with reference to experimental results, has led to the material definition presented in Table C-6.

Table C-6. Material definition used for the simulation.

Simulation Number	Elastic modulus E_f [GPa]	Tangent modulus E_T [GPa]	Yield stress σ_Y [MPa]	Static coefficient of friction μ
1	196	11	290	0.05

Figure C-5 shows both experimental and numerical pull-out curves. It appears that the numerical curve exhibits the same pull-out behaviour as the experimental ones. This is indicated by the general shape of both series of curves: an increase of the load up to the first peak which suddenly decays to a minimum then followed by another increase to the second peak which drops catastrophically.
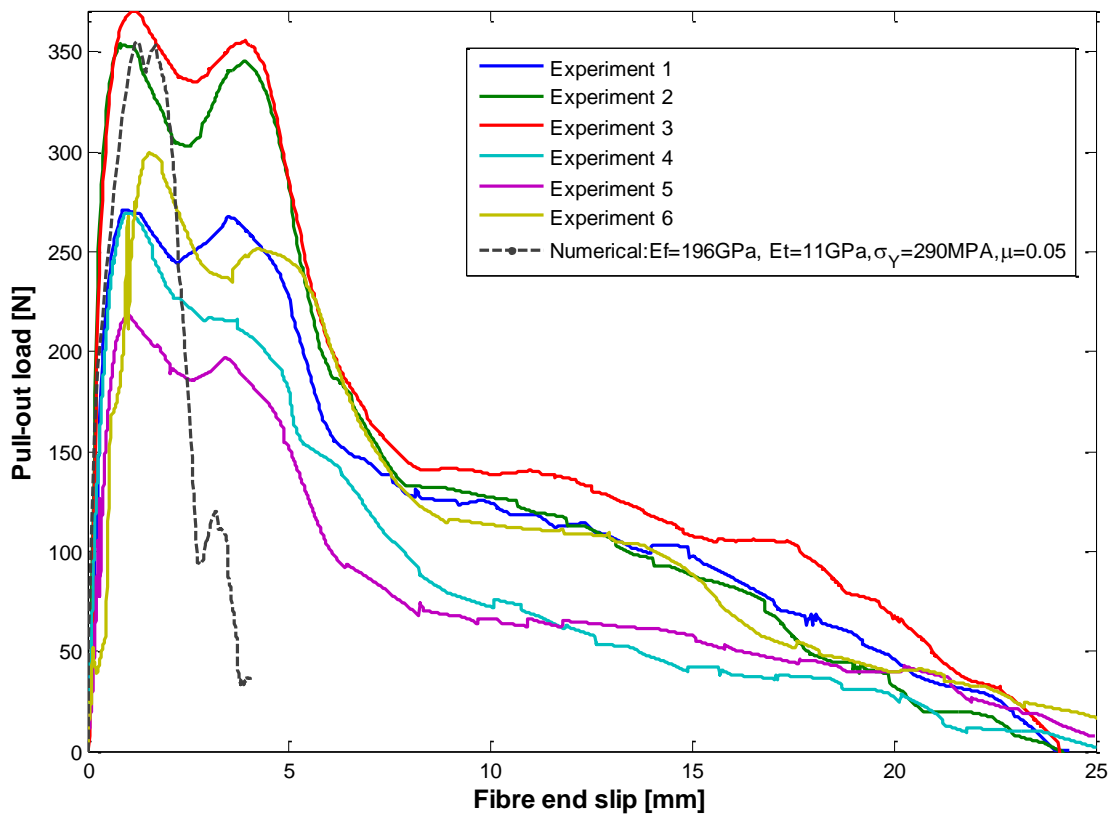
Figure C-5. Comparison of the proposed numerical curve to experimental curves.

Table C-7 shows the peak and minimum loads for the experimental pull-out and the corresponding fibre end displacements are also shown. These results indicate that the peak and minimum loads vary, significantly, from one test to another but the displacement of the fibre's end in the matrix channel are approximately the same. Therefore, a good match between the experimental and simulated loads is less likely, but we should insist on a good match between the experimental and simulated displacement.

The fibre end displacement in the numerical model is substantially smaller than the experiment results (as seen in Figure C-5).

Table C-7. Experimental pull-out: Loads and fibre's end displacements.

Experimental	Pull-out load [N]				Fibre's end displacement [mm]			
	P_{max1}	P_{min1}	P_{max2}	P_{min2}	Δ_{max1}	Δ_{min1}	Δ_{max2}	Δ_{min2}
1	370.6	334.9	355.8	140.7	1.166	2.637	3.922	8.363
2	354.6	302.5	345.7	132.6	0.8014	2.506	3.905	8
3	299.8	235.3	251.9	114.3	1.539	3.573	4.214	8.937
4	270.9	244.2	267.3	127.2	0.9273	2.247	3.538	8.114
5	268.9	216	216.5	72.11	0.9243	2.89	3.713	10.03
6	218.7	185.5	197	67.62	1.03	2.59	3.436	8.262

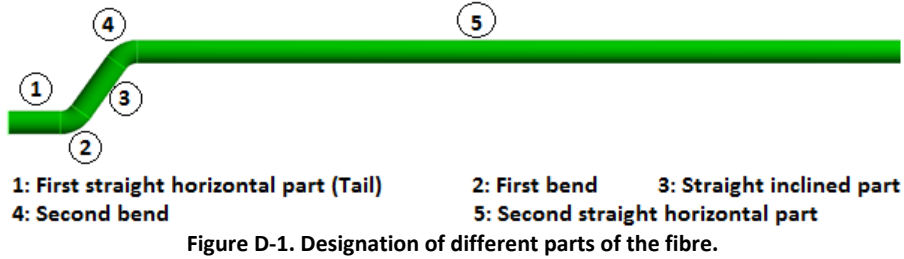| Average | 297.3 | 253.1 | 272.4 | 109.1 | 1.065 | 2.741 | 3.788 | 8.618 |

Table C-8 illustrates the discrepancies of the numerical displacements in comparison with the average displacements of six experimental curves. Based on these results it can be observed that variations between the experiment and numerical displacements are too big, therefore the results are not satisfactory from the fibre displacement standpoint.

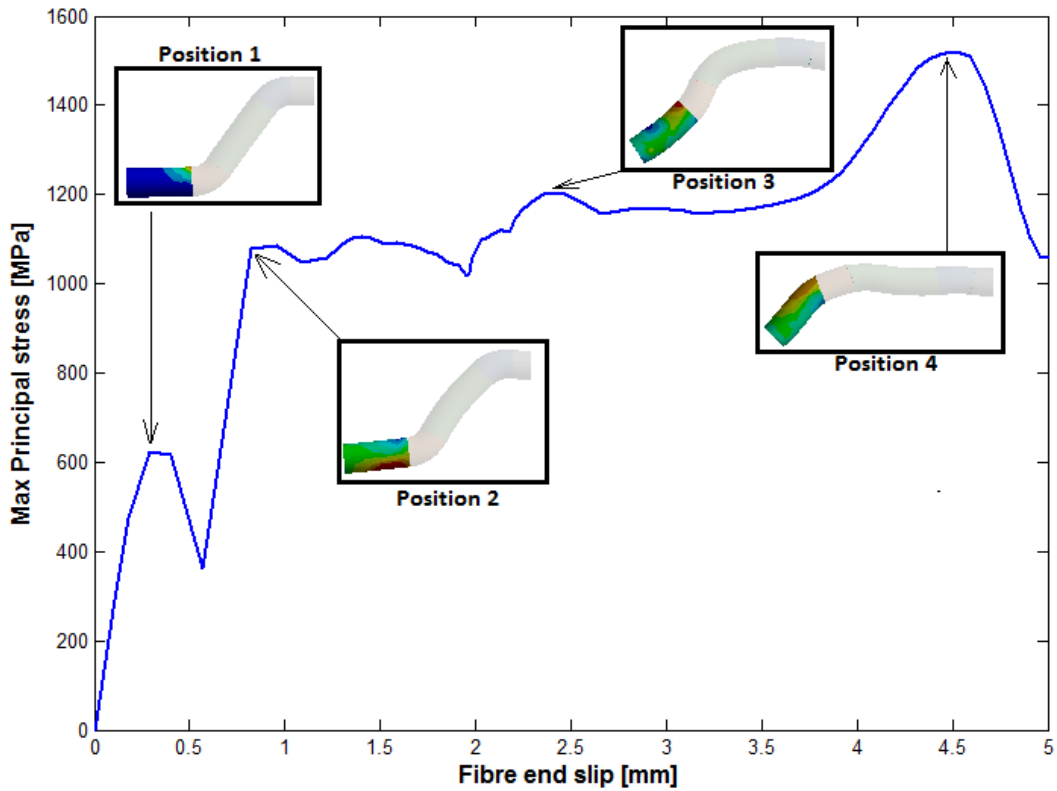**Table C-8. Comparison of numerical and experimental displacements.**

	Fibre's end displacement [mm]			
	Δ_{max1}	Δ_{min1}	Δ_{max2}	Δ_{min2}
Experimental [Average]	1.065	2.741	3.788	8.618
Numerical	1.243	1.433	1.682	2.812
Variation [%]	14	48	56	67

Appendix D   Additional details of the fibre's state of stress

Studies have been carried out for each individual part of the fibre as seen in Figure D-1.

1: First straight horizontal part (Tail)   2: First bend   3: Straight inclined part
4: Second bend   5: Second straight horizontal part

Figure D-1. Designation of different parts of the fibre.

Appendix D.1.   Fibre's maximum principal stress

Type: Maximum Principal Stress
Unit: MPa

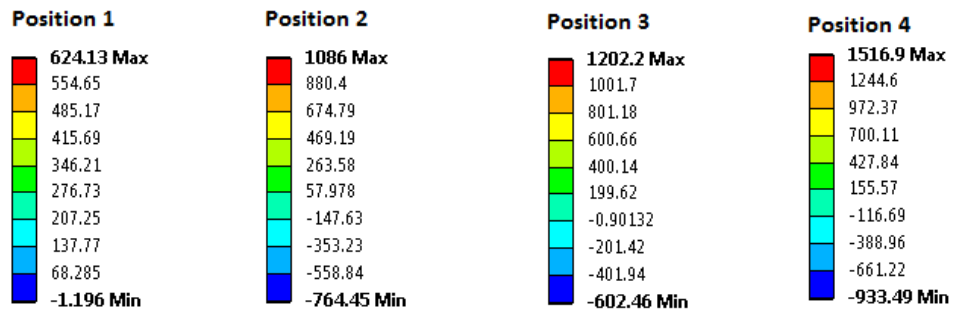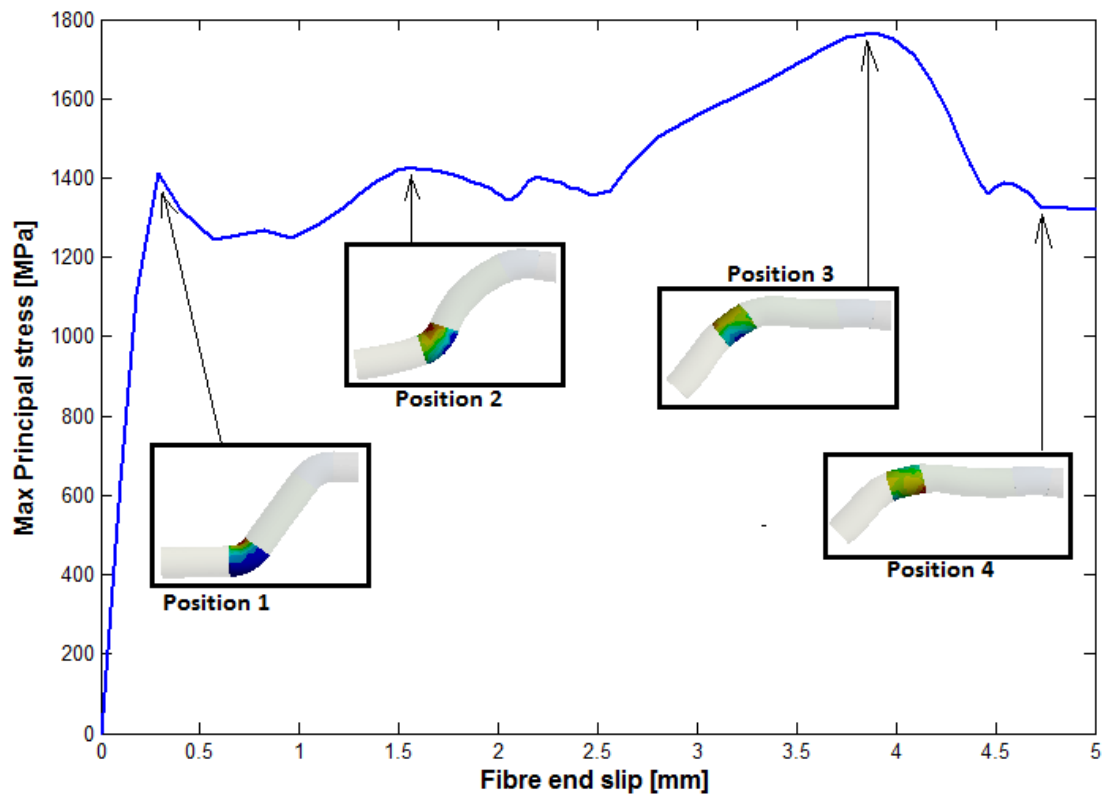| Position 1	Position 2	Position 3	Position 4
624.13 Max	1086 Max	1202.2 Max	1516.9 Max
554.65	880.4	1001.7	1244.6
485.17	674.79	801.18	972.37
415.69	469.19	600.66	700.11
346.21	263.58	400.14	427.84
276.73	57.978	199.62	155.57
207.25	-147.63	-0.90132	-116.69
137.77	-353.23	-201.42	-388.96
68.285	-558.84	-401.94	-661.22
-1.196 Min	-764.45 Min	-602.46 Min	-933.49 Min

Figure D-2. Maximum principal stress of the first straight horizontal part of the fibre (tail).

Figure D-3. Maximum principal stress of the first straight horizontal part of the fibre (tail).